MEASUREMENTS OF AERODYNAMIC DAMPING IN THE MIT TRANSONIC ROTOR

by

Edward F. Crawley

GTL Report No. 157 February 1981

GAS TURBINE & PLASMA DYNAMICS LABORATORY
MASSACHUSETTS INSTITUTE OF TECHNOLOGY
CAMBRIDGE, MASSACHUSETTS

MEASUREMENTS OF AERODYNAMIC DAMPING IN THE MIT TRANSONIC ROTOR

by

Edward F. Crawley

GTL Report No. 157 February 1981

This research was carried out in the Gas Turbine and Plasma Dynamics Laboratory, MIT, supported by NASA Lewis Research Center under grant NSG - 3079.

ABSTRACT

A method has been developed and demonstrated for the direct measurement of aerodynamic forcing and aerodynamic damping of a transonic compressor. The method is based on the inverse solution of the structural dynamic equations of motion of the blade disk system in order to determine the forces acting on the system. The disturbing and damping forces acting on a given blade are determined if the equations of motion are expressed in individual blade coordinates. If the structural dynamic equations are transformed to multiblade coordinates, the damping can be measured for blade-disk modes, and related to a reduced frequency and interblade phase angle. To measure the aerodynamic damping in this way, the free response to a known excitation is studied.

This method of force determination was demonstrated using a specially instrumented version of the MIT Transonic Compressor run in the MIT Blowdown Compressor Test Facility. Unique on-rotor instrumentation included piezoelectric displacement transducers to monitor the displacement of each blade, three accelerometers to measure in plane motion of the disk and a leading edge mounted total pressure transducer. Resonance tests performed prior to installation of the rotor in the tunnel indicate that the blade-disk structural interaction is dominated by the rigid body inertial coupling of the disk. An analytical model was developed for this inertial coupling. The model was verified by extensive testing of the tuned and severely mistuned rotor.

No regions of aeroelastic instability were found while testing the rotor in the Blowdown Facility, but three forms of forced vibration were

encountered. When operated in rotating stall, the blades were strongly excited at the fundamental frequency of stall cell excitation and those higher harmonics in proximity to blade resonances. At the fundamental frequency, the blade bending loading decreased as the blade entered the stall cell and increased as smooth flow was reestablished over the blade.

In runs near the operating point, the rotor was aerodynamically excited by a controlled two-per-revolution fixed upstream disturbance. The disturbance was sharply terminated midway through the test and the ring down of the rotor monitored. Analysis of the data in terms of multiblade modes led to a direct measurement of aerodynamic damping for several interblade phase angles.

During all runs, the third circumferential harmonic of the blade displacement was strongly excited by wakes shed from three evenly spaced upstream struts. The addition of a two per revolution fixed upstream disturbance caused a marked decrease in the third harmonic response, suggesting a nonlinear mechanism either in the upstream wake production or in the aerodynamic response of the rotor. It may therefore be possible to alleviate some forced vibrations by the deliberate introduction of upstream disturbances.

ACKNOWLEDGEMENTS

The author would like to acknowledge the efforts of all of those at M.I.T. who made this work possible, especially Professor Jack Kerrebrock, Dr. Alan Epstein and Mr. John Stanley. For financial support, I must thank the John and Fannie Hertz Foundation for their four years of generous fellowship support.

The research was supported under grant NSG-3079 from NASA Lewis Research Center, with Dr. John Adamczyk serving as monitor and advisor.

Contents

List of Symbols

a	amplitude of the sine multiblade mode
b	amplitude of the cosine multiblade mode
c	blade chord
f	force per unit area
f'	force per unit length
F	modal force
I	moment of inertia
j	$\sqrt{-1}$
k	stiffness
K	shaft stiffness
LE	leading edge
m	mass
M	modal mass
n	number of nodal diameter
N	number of blades
q	displacement
Q	quality of system
S	static imbalance
T	kinetic energy
TE	trailing edge
u	displacement in x direction
v	displacement in y direction
w	displacement in z direction
$\bar{w}$	blade displacement

α	angle of blade attachment to disk (Figure 4.1)
β	interblade phase angle
γ	mode shape
δ	log decrement
ν	wave speed
σ	see equation (4.19)
ψ_i	location of the ith blade
ω	natural frequency
Ω	frequency of rotation

Subscripts

A	assumed mode of the unweighted blade
B	assumed mode of the weighted blade
b	blade
d	disk
h	hub
i	ith blade
IP	in phase assumed mode
n	nth multiblade mode
OP	out of phase assumed mode
t	tip
T	sum of blade and disk
x	in the x direction
y	in the y direction
θ	in the circumferential direction

List of Tables

List of Figures

1. INTRODUCTION

It is of primary importance in the study of turbomachine aeroelasticity to develop techniques for the measurement of aerodynamic damping and eventually to gain an understanding of the physical processes which control that damping. Taken in its broadest sense, aerodynamic damping together with structural damping plays a role in both forced vibration and flutter, by limiting the amplitude of response and controlling the decay rates in the former and in the determination of the stability boundaries for the latter. It is the purpose of this investigation to develop techniques for the measurement of aerodynamic damping, and to make direct measurements of damping in a transonic rotor operating at a known point on its performance map.

The importance of aerodynamic damping can best be seen by examining a typical performance map with the aeroelastic stability boundaries superimposed (Figure 1-1). It can be seen that flutter boundaries can place limits on all sides of the performance map of the modern, lightweight transonic fan or compressor. Adamczyk [1] identifies five different stability boundaries, each of which is associated with a different unsteady fluid mechanical process [2,3]. Within the boundaries, the stage is aeroelastically stable, but is susceptible to forced vibration due to upstream and downstream disturbances, as well as unsteady effects such as rotating stall and surge. While the stability and forced vibration problems are usually formulated differently, Dugundji [4] has shown that given the aerodynamic damping coefficients in a proper form, the two problems can be analyzed in a unified systematic manner. Aerodynamic damping coefficients used in such an analysis might be based on either analytic or experimental results.

Since the early 1960's, a number of analytical models of damping in cascades have been developed. These analyses have in common that they model the 3-dimensional annular geometry of an axial flow turbomachine as a 2-dimensional infinite cascade, the blades of which undergo uniform sinusoidal motion with a fixed interblade phase angle. The force and moment coefficients for a given blade are then calculated. The earliest work focused primarily on the low-backpressure supersonic flutter of Region III (Figure 1-1), beginning with Whitehead's analysis of incompressible flutter of flat plate airfoils in bending [5] and in torsion [6]. This was extended to the compressible case by Smith [7] and to supersonic relative flow by Verdon [8]. Recent work by Whitehead [9] has extended the compressible flow case to cascades of finite thickness and high deflections using 2-dimensional computational fluid dynamics techniques [9]. Comparison of these 2-dimensional analytic models with experimental data by Snyder [10], shows that although these models greatly simplify the flow conditions, good agreement is found between experimental and predicted flutter boundaries for cascades.

The other four flutter regions have received less extensive analysis. A model which allows for finite shock strength has been developed by Goldstein [11] to examine the high-backpressure supersonic flutter of Region IV (Figure 1-1). Adamczyk has developed a low reduced frequency, small interblade phase angle model which treats the supersonic stall flutter Region V with an actuator disk model [1]. Finally, Ginzburg has proposed a low reduced frequency model [12] which can be used to treat the subsonic/transonic flutter of Region I, and the choke flutter of Region II. In general, these theories give qualitative agreement with observed

stability boundaries, but are not sufficiently refined to predict a priori the boundary location.

Experimental investigations of turbomachine aerodynamic damping fall into one of two distinctly different categories, cascade experiments and full scale rig tests. Cascade experiments are conducted in essentially 2-dimensional linear (finite) or annular (infinite) cascades. The blades are externally driven by mechanical or electromagnetic drivers with a uniform oscillatory motion and fixed interblade phase angle. Blades can be driven in rotational mode, representing torsional flutter [13] or in a translational mode, as in bending flutter [14]. Measurements of the overall aerodynamic damping as well as detailed measurements of the unsteady pressure distribution over the blade can be made over a wide range of Mach number and reduced frequency.

Full scale engine tests are performed by first heavily instrumenting a specially prepared stage or a fully operational engine and then running the device in the vicinity of one of its stability boundaries. Instrumentation usually consists of a number of low frequency response pressure taps to determine the overall operating point and flow conditions, and a large number of strain gauges mounted on the rotating assembly to monitor blade strain and displacement levels [15]. In the last few years, full scale rigs have also been run with miniature high frequency response pressure transducers mounted on the blade of a rotor, so that unsteady on-blade pressure measurements could be made in flutter. The principle value of these tests is to identify the location of the stability boundaries of real stages and the influence changes in operating parameters such as inlet temperature and pressure, as well as changes in blade design, have on these

locations. A further objective is to identify the modes of aeroelastic instability [16].

Each of the two experimental procedures, cascade and full rig tests, have their advantages and shortcomings. Cascade experiments, performed under controlled conditions, lend themselves to careful study of the influence that parameters such as reduced frequency and interblade phase angle have on aerodynamic damping. Detailed measurement of energy input and blade unsteady pressure distribution made in 2-dimensional cascades can be directly correlated with existing 2-dimensional theory. However, the principal shortcoming of cascades is that they fail to model the essential 3-dimensional nature of the flow in axial flow turbomachines, including such potentially important effects as strong radial variation in shock strength and boundary layer interaction, and distribution of total pressure rise and flow quantities due to work done on the fluid [17].

Full scale rig tests model this complex 3-dimensional nature of the flow, but do so under conditions which make the extraction of detailed quantitative information about aerodynamic damping extremely difficult. Since the blade-disk-shroud structural system is complex and highly coupled, it is often impossible to isolate the response of a single structural mode so as to gain parameteric information of damping in terms of reduced frequency and interblade phase angle. The results are confined to location of the boundary of neutral stability, rather than quantitative measurements of damping on either side of the boundary. Although there are empirical and semi-empirical procedures for the correlation of such 3-dimensional flutter data [18], there is really no truly 3-dimensional

theory to predict unsteady aerodynamic damping for a rotor operating at any point of its performance map.

The distinction between the two forms of experiments can be summarized in the following way. Cascades provide a controlled environment to gain detailed parameteric data but in simplified flow conditions. Rig tests operate under real flow conditions but an uncontrolled aeroelastic environment.

The purposes of this investigation are to help bridge this gap and to develop techniques by which quantitative parametric aeroelastic damping data can be extracted from a device operating in a real working turbomachine environment. The methods developed are general enough so that they can be applied to the investigation of any of the stability boundaries. They are also applicable to the interior of the performance map where the stage is stable, but encounters forced vibration. Included in the present work are both a description of a new technique for determining aerodynamic damping and the application of that technique to the MIT Rotor [19]. The result is one of the first direct measurements of damping in a transonic compressor.

The rotor chosen for the current experiments was the MIT Transonic Rotor, typical of current stages with a hub tip ratio of 0.5, tip Mach number of 1.2, pressure ratio of 1.6, and conventional, but somewhat stiff, blades. Since the rotor had never encountered flutter in testing, a scan of the performance map was made to locate any regions of aeroelastic instability. Although not all encompassing, 19 different runs were made, which probed the stall, high speed and choke boundaries of the map (Figure 1-2). For the current MIT Transonic Rotor design and within the limits of the MIT

Blowdown Test Facility, [20], no regions of instability were found.

The current investigation is therefore confined of necessity to those areas where the rotor is aeroelastically stable. Several cases of forced vibration and resulting measurements of damping will be shown in later chapters, but first the techniques and necessary background will be given, beginning with a description of the instrumented rotor, the experimental facility and the procedure in Chapter 2. In Chapter 3, the technique for the extraction of aerodynamic forcing and damping is developed. This technique requires a characterization of the structural dynamics of the blade disk system and a knowledge of the response while rotating in vacuum, which are reported in Chapter 4. An example of a direct measurement of damping obtained by subjecting the rotor to time varying upstream disturbances is given in Chapter 5. Other cases of forced vibration, including forced vibration due to rotating stall are discussed in Chapter 6, followed by a summary and conclusion in Chapter 7.

2. APPARATUS AND INSTRUMENTATION

2.1 The MIT Blowdown Facility and Compressor

2.1.1 The Blowdown Facility

The MIT Blowdown Compressor Facility, in operation for nearly ten years, has been used to gather extensive data on the aerodynamic performance of the MIT Transonic Compressor [19], as well as other state of the art compressor stages [21]. The facility itself consists of three main components, a supply tank, test section, and dump tank (Figure 2-1). Prior to the test, the supply tank is filled to an initial pressure of 464 mm with a Freon 12-Argon mixture having a speed of sound 74% that of air, and a ratio of specific heats of 1.4. Downstream of an aluminum diaphragm and still in the vacuum, the rotor is driven to speed by a small electric motor. The test is begun by cutting power to the motor and explosively cutting the diaphragm. After a start-up transient of approximately 60 msec, the flow becomes quasi-steady in the test section with the supply tank essentially behaving as a stagnation plenum. The mass flow is set by an orifice downstream of the stage which remains choked for about 150 msec. During the test, the rotor slows down, doing work on the flow. By proper matching of the rotor inertia and initial supply tank pressure, the tangential Mach number of the rotor can be kept constant. The torque can be determined by monitoring the rotor deceleration. During this period of constant Mach number flow, the steady aerodynamic performance of the stage can be determined from a number of wall static pressure transducers, and a five-way pressure probe which traverses the flow during the test [22]. For a complete discussion of the dynamics of the Blowdown Facility, see

Reference [20]. Reference [21] describes in detail the data reduction technique used to determine overall stage performance.

2.1.2 MIT Rotor

The Blowdown Facility has been adapted for use in aeroelastic studies by structural, but not aerodynamic, modification of the MIT Transonic Compressor Rotor, the geometry and performance of which are extensively documented in [19]. The 23 blade, 23.25 inch diameter rotor operates at a tip Mach number of 1.2, an average pressure ratio of 1.66. The mass flow corrected to air at standard temperature and pressure is 84.7 lbm/sec (38.4 kg/sec) at the design point. The rotor is cantilevered forward of a center body on which a fixed 48 blade stator is mounted, and which houses the drive motor and a 12 channel slip-ring assembly. In aeroelastic studies, these slip rings are supplemented by a 24 channel slip ring assembly housed in a centerbody supported by three struts ahead of the rotor (Figure 2-2). At design, the overall stage pressure ratio is 1.6.

2.1.3 Secondary Flow Injector

In certain runs, a time varying upstream disturbance was created in front of the rotor. This disturbance was created by the interaction of the primary flow with a series of small jets injected normal to the surface of streamlined struts five inches upstream of the rotor face. The injection takes place through a 5/8 inch tube which extends 3 inches into the tunnel from the outer wall and is faired by an NACA 0012 airfoil. Two such assemblies were located 180° apart, at the 0° and 180° instrument locations (right and left hand sides looking downstream). Figure 2-3 shows the

injector protruding into the tunnel downstream of the boundary layer bleed and upstream of the rotor. A close-up showing the fairing and proximity of the injector to the rotor is shown in Figure 2-4.

The injector operates in the following manner. At 50 msec after the diaphragm bursts, just as quasi-steady flow is established in the facility, the main injector solenoid valve is opened, venting Argon from a 110 in^3 (1.8×10^{-3} m^3) supply bottle at 150 psi into the inner diameter of the injector assembly. The assembly consists of two concentric tubes, an outer tube to which the fairing is attached and an inner tube which is free to rotate within the outer (Figure 2-5). The assembly of fairing, outer and inner tube has drilled through its walls two rows of twelve 1/16" diameter holes (1/8" center to center). The rows are on opposite sides of the injector tube, one facing in the clockwise, and the other in the counterclockwise circumferential direction (Figure 2-5). The high pressure argon passes through these holes and is injected normal to the mean flow. In this way, the symmetric disturbance creates a region of velocity defect behind the injector, but imparts no mean swirl in the flow. The radial extent of the defect is about 1 1/2 inches, and the circumferential extent is determined in part by the total pressure ratio of the mean flow to injected flow. With the given geometry and supply pressure, each injector adds only 0.27% to the mass flow of the tunnel.

The disturbance is shut off at 100 msec after the start of the test by pneumatically operating a rotary piston. This piston rotates the inner tube of the assembly, closing off the two rows of vent holes in less than 1 msec. In this way, a very well defined and sharp termination of the

upstream disturbance is achieved, which will be important in the later analysis.

The creation of upstream disturbances by injection of a secondary flow is not a new concept. In fact, several of the major laboratories have sophisticated devices for creation of arbitrary distortion patterns [23]. The emphasis in those facilities is on degradation of engine performance due to distortion. The patterns created are therefore steady, requiring time on the order of seconds to change. The unique features of the injector described are its fast shut off characteristics and the ability to tailor the circumferential extent of the disturbance simply by changing injector supply pressure.

2.2 Instrumentation and Data Acquisition

2.2.1 Rotor Instrumentation

In addition to the usual tunnel instrumentation used at the blowdown facility, a unique set of on-rotor instrumentation has been developed for aeroelastic experimentation. This includes piezoelectric crystals and strain gauges to monitor blade motion, accelerometers to monitor disk motion, and a blade-mounted total pressure probe.

Several years ago, a second article of the MIT Transonic Compressor Rotor was built, which incorporated a piezoelectric crystal into the root of each blade [24]. The details of the root attachment (Figure 2-6) show that the blade is attached well below the fairing line of the disk. The piezoelectric crystal assemblies (consisting of a soft rubber spring, G-10 glass/epoxy disk, brass electrical contact and PZT5H crystal) are held in place between the disk and blade. In this configuration, the crystals

can be used either to drive the blades with independent control of driving amplitude and phase, or as displacement transducers. As transducers, the crystals give a signal, linear to a very high amplitude, which can be calibrated against tip displacement for each of the natural modes of the blade. For the first flexural mode, the crystal yield a gain of 2400 V/in or 24 Volts across the rings for a nominal 0.01 inch tip deflection. Signals from the 23 crystals plus ground were carried across the forward set of 24 slip rings.

It should be emphasized that for frequencies above its RC rolloff point (about 30 Hz), the piezoelectric crystal (PZT) is functionally identical to a strain gauge. That is, it measures the blade displacement at one point, and for any blade mode this can be related to the displacement at all points on the blade. To confirm this functional similarity, four blades were also strain gauged with semiconductor gauges in a position to give primary sensitivity to the blade's first bending mode (Figure 2-7). When the PZT and strain gauge signals for the same blade were properly filtered and scaled in terms of tip displacement, they showed exactly the same time history of blade motion. The advantages of PZT's in this application are that they are rugged and produce a signal of 500 to 1000 times greater amplitude than that of a semiconductor strain gauge. Since they are active transducers, N blades instrumented with PZT's require N+1 slip rings, while strain gauges would require 2N+2 rings. Their principal and perhaps overwhelming disadvantage is that they must be incorporated into the blade disk system at its design, and cannot be retrofitted to a rotor as can strain gauges.

Of interest to the understanding of the response of the blade disk

system is the in-plane motion of the disk. To monitor this, the disk was instrumented with three Bolt Beranek and Newman Model 501 miniature accelerometers, with a nominal sensitivity of 10 mv/g. The accelerometers were mounted 120° apart with their axis of principal sensitivity aligned in the circumferential direction (Figure 2-7). From these three accelerometer signals, one can extract the rotational and two translational components of in plane disk acceleration.

While most piezoelectric accelerometers are charge coupled devices, the BBN accelerometers produce a voltage output by using an FET amplifier inside the device. The cost of this choice, made to reduce slip ring noise, was that a power supply line for the FET's had to be run to the rotor, and a power-signal conditioning circuit for each accelerometer had to be included on the rotor. These three circuits, as well as all other on-rotor connections were potted in an epoxy module and mounted inside the rim of the disk. The accelerometers worked perfectly when the rotor was run at full speed in vacuum. However, during the actual data test runs, one signal consistently failed and the other two were intermittent. After the test, the accelerometers were always found to be working perfectly again. This pattern of failure and recovery is probably due to thermal or acceleration spikes saturating the signal conditioning circuit. This behavior could be eliminated by either thermally insulating the accelerometers or by soft mounting them to the disk so that accelerations above several thousand Hertz would be attenuated. In the present investigation, neither of these remedies were attempted.

The final piece of on-rotor instrumentation was a total pressure probe, aligned with the relative flow and located on the leading edge of blade 8

at $r/r_T = 0.73$, just on the nominal sonic radius (Figure 2.7). The transducer used was a third generation Kulite high frequency response silicion diaphragm type CQ-080-25 with type B screen, and a diameter of 0.064". Mounted inside a supporting stainless steel tube, the probe was located as far out radially as the structure of the blade would allow. The active diaphragm was 0.2" in front of the blade leading edge. Signals from the pressure probe, as well as accelerometers and strain gauges were carried on the 12 rear slip rings.

The intent of placing a total pressure probe on the leading edge was to investigate circumferential nonuniformities in the flow. The transducer performed flawlessly, capturing low and high frequency content of the pressure field with no apparent thermal drift. The pressure field measured, even in the absence of any upstream distortion, was more complex than expected. It was rich in frequency content in the range of several hundred to 2000 Hz, and not easily identifiable with any blade resonance or acoustic mode of the Blowdown Facility. The complete analysis of this acoustic signal, and comparison with pressure measurements made by fixed transducers will be the subject of further investigation.

Before moving on to the fixed instrumentation, it should be noted that in 11 runs to full speed made in the most recent test, aside from the accelerometer problems there were no failures of instrumentation in the rotating system, despite vigorous vibration and centrifugal loading of up to 20,000 g's at the pressure probe location.

2.2.2 Tunnel Instrumentation

Fixed instrumentation, pressure sensors and tachometers, used to determine the overall operating conditions of the stage were essentially

identical to those used in previous experiments in the blowdown facility, and are thoroughly documented in [19] and [21]. Beginning at the extreme upstream end of the facility, the pressure in the supply tank is measured by two low frequency response transducers. These indicate the total pressure of the upstream flow, and from their decay rate, the mass flow through the facility can be determined [20]. One chord upstream of the rotor at 0° and 72° circumferential location are a pair of high frequency response (50 KHz) kulite semiconductor wall static pressure gauges.

Between the rotor and the stator is a low frequency static pressure gauge and the location of the five-way probe. Unlike in aerodynamic tests when the five-way probe is used to traverse downstream of the rotor from tip to hub during the quasi-steady flow period, in these aeroelastic tests, the probe was quickly translated to one radius, r/r_T equals 0.93, before the establishment of quasi-steady flow, and left there during the entire test. In this way, it was hoped the effect of unsteady blade motion on the downstream Mach number, pressure and flow angles at one radius, the aeroelastic radius, could be understood. However, like the data from the rotating total pressure probe, the five-way probe data is very complex, and lends itself to no simple analysis. Except for extraction of overall qualities such as downstream total pressure, this data will be left for further analysis together with the other unsteady pressure data. Finally, measurements were made of the dump tank pressure, and of a one per revolution and a 115 per revolution tachometer on the rotor shaft.

2.2.3 Data Acquisition

In summary, data was collected on 44 channels, including 23 PZT's, 2 strain gauges, 3 accelerometers, 2 tachometers, 12 pressure gauges, and 2

other channels. Data rates ranged from 5 KHz for vibration data to 100 KHz for high speed pressure data. The management, storage and analysis of this data was a formidable task. The amount of data taken and number of channels exceeded the existing analog to digital conversion capability of the Blowdown Facility [21]. As part of this investigation, a new A/D system based on the CAMAC convention and manufactured by LeCroy was acquired, installed, integrated into the lab's PDP 11/70 and checked out. Run in parallel with the existing MIT A/D system, this gave a capability of sampling 14 channels at up to 100 KHz, and 46 channels at up to 10 KHz, with an aggregate storage of 170,000 data samples.

High speed pressure transducers and strain gauges were amplified and digitized directly, while low speed pressure signals were amplified and low pass filtered at 1 KHz prior to digitization. Accelerometer signals were low pass filtered at 600 Hz, then digitized, but PZT's and tachometer data went directly into the A/D converter. Immediately after a test, data from the MIT A/D is moved from core to disk, while data from the CAMAC A/D is read slowly over a serial line to core and finally to disk. All data is eventually backed up to magnetic tape, where it is stored for further analysis.

2.3 Summary of a Typical Run

A concise summary of the instrumentation used is given in Table 2.1. Listed with each transducer are its location, the analogue to digital converter and channel type used to digitize the data. If the signal was low pass filtered before digitization, the -3 dB cutoff point of the four pole Bessel filter is also listed. Table 2.2 gives the chronology of major

events during the run. Note that times listed are after the rupture of the diaphragm which begins the flow of gas into the test section. In some runs, the diaphragm was broken at time t = 0, while in other runs, the diaphragm rupture was delayed 20 msec to observe the response of the blades in vacuum at speed for those 20 msec.

To put in perspective the overall pattern of a test and some of the data collected, Figure 2.8 shows the pressure and blade response time histories for a run in which the stage was operated in rotating stall, and the diaphragm was commanded to rupture at 20 msec. The top two traces show the wall static pressure one chord upstream and 0.1 chord downstream of the rotor, and the bottom trace shows the response of blade 12 as measured by the piezoelectric transducer. The test can be divided into three time periods. From 0 to 24 msec, the rotor is spinning in a vacuum and there is a low level of vibration of the blades. At 24 msec, the gas arrives and impulsively drives the blades backwards, the blade row acting as a turbine. The start-up time, reflected in the pressure and blade response, extends until about 70 msec, after which the flow becomes quite steady. In this last period, from 70 to 140 msec, three effects are reflected in the pressure signal: a steady decrease with a time constant of about 100 msec as the supply tank pressure drops; the stall cell passage with a period of 7 msec; and the blade passage with a period of 0.3 msec. The blade response to the stall cell passage is almost as large as that caused by the initial transient. All further discussion of the blade response will be confined to the time after 70 msec, or 50 msec after diaphragm opening, when quasi-steady flow has been achieved.

3. COMPUTATION OF AERODYNAMIC FORCES ACTING ON THE BLADES

The data commonly acquired in full scale engine aeroelastic tests is the deflection of the blades relative to the disk. This data can be extracted from simple strain gauge data, or, in the case of this investigation, piezoelectric displacement transducer data. The quantity of ultimate interest to the aeroelastician is the net aerodynamic force acting on the blade. These aerodynamic forces might be due to perturbations in the flow arising oustside the blade row, which can lead to forced vibration, or they might be due to the motion of the blades, in which case they can be classified as damping terms.

In this chapter, a technique will be outlined for direct computation of the aerodynamic forces acting on a blade from the blade deflection data. Some aeroelastic effects in rotors are best viewed in a local sense, such as the forced vibration of a blade due to passage of a stall cell. Other effects are better viewed on a more global level, such as the correlation of blade damping with interblade phase angle. In view of this, two complementary techniques will be developed for the computation of aerodynamic forces acting on blades; one which focuses on the response of a single blade and is based on the concept of dynamic substructuring, and a second which focuses on the response of the entire blade disk system and is based on the use of multiblade or modal coordinates. Since the single blade case is most direct and lays the foundation for the multiblade case, it will be discussed first.

3.1 Computation of Forces Acting on a Single Blade

3.1.1 Single degree of freedom blade

If a blade is modelled as a single degree of freedom cantilever mounted on a rigid massive disk, as in Figure 3-1(a), then the governing equation of motion is simply:

$$m_1 \ddot{q}_1 + k_1 q_1 = F(t) \tag{3.1}$$

The problem usually solved with this equation is to find the response q_1 of mass m_1 to an arbitrary forcing function F(t). However, the problem at hand is the inverse problem, that is to find the aerodynamic forces acting on a blade. The new problem statement is: given an arbitrary response q_1 (and $\ddot{q}_1$), find the force F(t) which would produce this response.

If the motion of the blade were represented by Equation 3.1, the problem would be solved at this point. But two major simplifications were made in arriving at this simple model, first that the blade has a single degree of freedom and second that the disk is massive and rigid, and takes no part in the motion. These simplificatlons will be removed first by allowing participation of the disk, then by including multiple degrees of freedom of the blade.

3.1.2 Single DOF blade with disk participation

The blade can be considered a substructure of a complex blade-disk-shaft structural system. Each blade is attached to a part of the disk with finite mass and elasticity. Through the root attachment, the motion of the

disk can influence the blade asa substructure in much the same way the motion of the ground excites a building in an earthquake.

Fabunmi proposed a very general model for this blade disk interaction [24], a segment of which is reproduced in Figure 3-1(b). In this model, each section of the disk has mass m_2, and is influenced by other sections of the disk through the springs k_2 and by the shaft through the spring k_3. The displacement q_2 is the absolute displacement of the disk, and q_1 is the displacement of the blade relative to the disk. The governing equations for this system become

$$m_1 \ddot{q}_1 + m_1 \ddot{q}_2 + k_1 q_1 = F(t) \tag{3.2}$$

$$m_1 \ddot{q}_1 + (m_1 + m_2) \ddot{q}_2 + (k_2 + k_3) q_2 = F(t) \tag{3.3}$$

The exciting force F(t) can be solved for in one of two ways. If both Equations 3.2 and 3.3 are given, F(t) and q_2 can be solved for, given only q_1. Given only Equation 3.2, F(t) can be found if both q_1 and q_2 are known. In this second approach, q_1, the relative displacement, can be inferred from strain gauge data, and q_2 can be measured directly with an accelerometer placed on the disk at the blade disk interface. Thus, with the proper strain gauge and accelerometer data, the disturbance force F(t) acting on the blade can be found directly. While this development used a simple lumped mass model of the blade and disk, a model allowing distributed mass and flexibility of the blade and disk results in equations of the same functional form as Equations 3.2 and 3.3, but with slightly different definitions of the mass and stiffness constants. The essential feature remains that given any characterization of the structural interac-

tion of the form of Equation 3.2 and the required data, the aerodynamic forces on the blade can be calculated.

3.1.3 Multi Degree of Freedom blade

The simplification that the blade has only one degree of freedom can be relaxed by expressing the displacement on the substructure of the blade in terms of its blade cantilevered normal modes. Then if the equations of motion are written in terms of the blade normal modes, the governing equations reduce to r single degree of freedom equations of the form

$$M_r \ddot{q}_r + M_r \omega_r^2 q_r = F_{r_{total}} \qquad r=1,2,... \tag{3.4}$$

where q, ω_r, M_r and F_r are the modal displacement, frequency, mass, and the net modal force exclusive of the elastic restoring force. The blade displacement is given by

$$\bar{w}\ (x,y,t) = \sum_r q_r\ (t)\ \gamma_r\ (x,y) \tag{3.5}$$

where γ_r is the r^{th} blade mode shape, and the modal force is defined by

$$F_r\ (t) = \int_{r_h}^{r_t} \int_{LE}^{TE} f(x,y,t)\ \gamma_r\ (x,y)\ dy\ dx \tag{3.6}$$

Using equation (3.4), the total modal force can be calculated if the modal mass, frequency and displacement are known. The modal mass and frequency can be found numerically using finite element models or experimentally. In this investigation, the modal mass was calculated from mode shapes measured holographically and the response of the blades spinning in vacuum was used to determine the natural frequencies. Some

care must be exercised in determining the modal displacement. If the natural frequencies are well separated and the blade response is primarily at or near the natural frequencies, then the modal displacements can be determined by band pass filtering the total response of a single displacement transducer and scaling the result appropriately. If the blade frequencies are closely spaced, or if the response of the system is not easily identifiable with a single particular mode, as would be the case in bending-torsion flutter, a more elaborate technique would be required. Several strain gauges could be used, each primarily sensitive to one blade mode. In general, to determine the displacement of N modes, at least N transducers would be required.

Substitution of the known amplitude, mass and frequency in equation (3.4) will give the modal component of the sum of all the forces acting on the blade. This sum contains at least three distinct components,

$$F_{r_{total}} = F_{r_{aero}} + F_{r_{disturbance}} + F_{r_{disk}} \tag{3.7}$$

the unsteady aerodynamic forces due to blade motion and interaction, the unsteady aerodynamic forces due to upstream or downstream disturbances, and the forcing of the blade due to interaction with the disk, and shrouds, if present. Unlike the energy approach, this generalizable formulation of the problem using the equations of motion with the aerodynamic damping and disturbance forces on the right hand side allows a consistent treatment of both forced vibration and flutter [4].

Looking at the origins of each of the force components, the disturbance force includes effects of blade passage through stationary circumferential nonuniformities in the flow such as inlet distortion, wakes from

struts and guide vanes, influences from upstream and downstream stators and nonuniformities in burner outflow in the case of a turbine. Also included would be unsteady aerodynamic loads not attributable to the motion of the blades themselves such as loads induced by surge and rotating stall.

The disk force is the term through which the presence of the disk and shrouds is accounted for. If handled rigorously, the influence of the disk and shroud would be included by a complete specification of the stress or displacement state of all the surfaces of contact of the blade with other parts of the blade-disk system. However, with a proper model of the structural dynamics of the blade disk system, the expression of this disk interaction force can be considerably simplified. In the single blade degree of freedom model of Equation 3.2, the disk force appears simply as the base acceleration term ($m_1\ddot{q}_2$). In the MIT Rotor, the three accelerometers described in Section 2.2.1 will be sufficient to characterize the disk force. In general, the number of pieces of data required to characterize the disk force will depend on the details of the rotor studied, and will increase as the number of blade modes and degree of participation of the disk in the model is increased.

After the disk and disturbance forces have been sorted out, the remaining aerodynamic force is the one of most interest in the understanding of aerodynamic damping. The aerodynamic modal force of equation (3.7) represents exactly the quantity one calculates for each blade in determining flutter boundaries, that is, the integrated effect along the blade span of the local damping forces. In the conventional calculation, Equation (3.6) is evaluated as

$$F_{r_{aero}}(t) = \int_{r_h}^{r_t} f'(x,y)\, \gamma(x)\, dx \qquad (3.8)$$

where f′ is the force per unit span usually found either from a two-dimensional theory or the results of cascade experiments.

There are two potential sources of error in the proposed method for force computation, the choice of natural frequency ω_r, and the twice differentiation of the blade displacement to obtain the acceleration. The accuracy of the differentiation depends on the data sampling rate and algorithm used in the differentiation, and will be discussed in Chapter 6. An error in the choice of natural frequency in equation (3.4) will introduce an error in the force which is in phase with displacement. The result will be a small error in the amplitude and phase of the force. From the simple case of a free decay, it can be shown that the error introduced in the phase is small, provided the fractional error in frequency is small compared to the critical damping ratio. Provided this criterion is met and the differentiation done accurately, the modal force acting on the system will be correctly calculated.

Since the blade damping force (F_{aero}) depends strongly on the motion of the other blades in the cascade, it is best analyzed by the more global method developed next. The single blade approach as formulated with equation (3.4) is best used to study forced vibrations localized to one or several blades. Finally, it should be noted that the equations (3.4) for the blade modal displacement which appear uncoupled can be recoupled through the force term in one of two ways. This could occur either through the disk force ($F_{r_{disk}}$) if the disk or shrouds strongly couple the blade modes, or through the aerodynamic damping force ($F_{r_{aero}}$) if the unsteady aerodynamic effects couple the modes. If these equations are solved in an uncoupled way, as will be done in this analysis, it must be recognized as a simplification of the actual system.

3.2 Analysis of Blade Motion using Multiblade Coordinates

Certain forces acting on the blades are best viewed in a global sense, that is looking at the response of all the blades simultaneously. Among these are the unsteady aerodynamic damping which can be expanded in its most general form as

$$F_{i_{aero}} = F_i\,(q_i, \dot{q}_i, \ddot{q}_i) + F_{i+1}\,(q_{i+1}, \dot{q}_{i+1}, \ddot{q}_{i+1}) + F_{i+2}\cdots + F_{i-1}\,(q_{i-1}, \dot{q}_{i-1}, \ddot{q}_{i-1}) + F_{i-2}\cdots \tag{3.9}$$

where the force acting on the i^{th} blade is dependent in some way on the blade's own position, velocity and acceleration, and the position, velocity and acceleration of all the remaining blades in the cascade, as well as the aerodynamic parameters. In current analytical models for compressible and transonic aeroelastic interaction [7,8], the assumption is made that every blade in the cascade moves with a constant amplitude, frequency and interblade phase angle. These assumptions reduce the complex functional dependence expressed by the infinite series of equation (3.9) to a dependence on just three parameters, the amplitude, reduced frequency ($\omega c/V$) and interblade phase angle, for any given aerodynamic operating point and cascade geometry. In this way, the displacement of the i^{th} blade of an N blade rotor located at ϕ_i is given as

$$q_i = A\, e^{j(\omega t - n\phi_i)} \qquad i = 1,2,3,\ldots,N \tag{3.10}$$

where

$$\phi_i = \frac{2\pi}{N} \; i$$

$$\beta = \frac{2\pi}{N} \; n$$

where ρ is the interblade phase angle and n is the number of nodal diameters.

While this traveling wave formulation is useful in aerodynamic calculations, an alternate multiblade coordinate formulation [25] is more useful in analyzing the structural response. In this formulation, the displacements of the blades are given as a sum of two standing waves of the disk, $\cos n\phi_i$ and $\sin n\phi_i$ corresponding to n nodal diameters such that

$$q_i = a_n \sin n\phi_i + b_n \cos n\phi_i \tag{3.11}$$

where: a_n , b_n - generalized coordinates

$\cos n\phi_i$, $\sin n\phi_i$ - disk modes

$\beta = \frac{2\pi}{N} n$ - interblade phase angle

The relation between the two formulations can be seen by expanding the real part of equation (3.10)

$$q_j = A \cos (\omega t - n\phi_i) \tag{3.12}$$

$$= A \cos \omega t \cos n\phi_i + A \sin \omega t \sin n\phi_i$$

By comparing this to equation (3.11), it can be seen that if a_n and

b_n are sinusoidal and temporarily out of phase by 90° they give rise to a travelling wave with interblade phase angle β.

The advantages of formulating the structural problem in generalized multiblade coordinates as opposed to individual blade coordinates of the type in equation (3.4) are several. First, each coordinate conveys information about the global, rather than the local behavior of the rotor. Second, the coordinates relate directly to the interblade phase angle used in unsteady aerodynamic calculations. Third, as will be seen in Chapter 4, the structural dynamic equations for the blade disk system expressed in multiblade coordinates are considerably simpler than those expressed in individual blade coordinates.

3.3 Application of Techniques for Computation of Blade Forces

Listed below is a brief step by step explanation of the application of the techniques discussed to a set of structural response data for the purposes of computing aerodynamic forces. This is given both as a summary of this section and as a guide to the remainder of this report which will follow this procedure:

1. Develop the equations of motion of the blade disk system which adequately characterize the blade modes expected to be present and the blade disk interaction. This will be done in Chapter 4.
2. Run a "model experiment", at full speed, but in vacuum to determine the excitation of the blades, if any, through the structural system. This will be discussed at the end of Chapter 4.

3. Run the aeroelastic experiment collecting data on every blade response and disk participation and analyze the data in the following manner:

a) Identify by Fourier transform in time, the dominant frequencies of response and the blade modes (first bend, etc.) with which they are associated.

b) Narrow band pass filter the raw data to isolate each frequency of response.

c) If the excitation is local, work directly with the data produced in (b). If the response is global, perform discrete Fourier transforms of the blade data in theta to transform to multiblade coordinates.

d) Use the amplitude data collected, together with the structural model, to calculate aerodynamic forces acting on the blades.

Examples of this last step will be given in Chapters 6 and 7.

4. Structural Dynamics of the MIT Rotor

4.1 Inertial and Elastic Coupling in Bladed Disks

In determining the response of the rotor to applied external forcing, and especially in determining the flutter boundaries of a stage, it is important to understand and characterize the coupled response of the blade-disk or blade-disk-shroud system. Previously, several authors have discussed the effects of blade-disk elastic coupling [26] and blade-disk-shroud elastic coupling [27] on the modal response of a tuned rotor. Other investigators have looked further into the effect that mistuning of blades has on the response of these systems [28].

These studies have focused primarily on the coupling of the flexural and torsional modes of the blades through out of plane elastic deflection of the disk. In these models, the hub or center of the disk is usually constrained from motion in or out of the plane. Therefore the resulting coupling of blade modes into blade-disk modes, characterized by a number of nodal circles and diameters, is attributable solely to the elastic deformation of the disk. Even the very general model of Fabumni [24] which allows for in plane and out of plane motion of the disk imposes the boundary condition that the hub center remain fixed.

The hub of any real rotor is not perfectly constrained, but is elastically constrained by the stiffness of the shaft on which it runs. In the case of an isolated rotor on a shaft, the transverse deflection of the shaft allows two in plane translation and two out of plane rotational modes of the disk. The single out of plane translational degree of freedom of the disk is resisted by the longitudinal stiffness of the shaft. The last

of the six rigid body modes of the disk, in plane rotation, is completely unconstrained by a shaft running on bearings.

Any of these rigid body degrees of freedom of the disk can couple the blades through the inertia of the rotor. In principle, all six should be considered in computing the coupled modes of the bladed disk. In the case of very flexible disks, these couplings could be dominated by the out of plane elastic deflection of the disk. However in the case of research rotors which tend to have thick, massive disks, the inertial effect of the relatively rigid disk can be the dominant source of blade disk coupling.

This chapter will deal with the question of in plane inertial coupling as observed in the MIT Rotor. In the next section, a model of the blade-disk-shaft system will be developed. In subsequent sections, the results of three sets of experiments are discussed in which the natural modes of the bladed rotor were found. In the first set of experiments, the blades were uniform and well tuned. In the latter two sets, different combinations of blades were weighted at the tips to produce a bladed disk system with extreme nonuniformity. The frequency results obtained from these experiments were found to correlate well with the proposed model.

4.2 Model of Blade-Disk Inertial Coupling

The proposed model of the blade-disk system is shown in Figure 4-1. A solid disk extends from the center to the hub radius ($r = r_h$), and possesses two translational and one rotational in plane degrees of freedom. Extending from the hub to the tip ($r = r_t$) are N blades located at angles ψ_i ($\psi_i = 2\pi i/N$). The blades deflect with a single mode shape γ which has an amplitude of $q_i r_t$. For every mode shape, the twisted blades deflect at

an effective angle to the normal, so their in plane component of deflection is $q_i r_t \cos\alpha$ With these assumptions, the deflections of a point on the blade are given as

$$\begin{aligned} u &= q_x - r q_\theta \sin\psi_i - \gamma r_t q_i \sin\psi_i \cos\alpha \\ v &= q_y + r q_\theta \cos\psi_i + \gamma\, r_t\, q_i \cos\psi_i \cos\alpha \\ w &= \gamma\, r_t\, q_i \sin\alpha \end{aligned} \tag{4.1}$$

Evaluating the kinetic energy of a single blade gives

$$T_i = \frac{1}{2} \int_{r_h}^{r_t} (\dot{u}^2 + \dot{v}^2 + \dot{w}^2)\, dm$$

$$= \frac{1}{2} \int_{r_h}^{r_t} \Big(\dot{q}_x^2 + \dot{q}_y^2 + r^2\dot{q}_r^2 + \gamma^2 r_t^2 \dot{q}_i^2 + 2\dot{q}_\theta r \Big[\dot{q}_y \cos\psi_i - \dot{q}_x \sin\psi_i\Big] + 2\dot{q}_i \gamma\, r_t \cos\alpha \Big[\dot{q}_y \cos\psi_i - \dot{q}_x \sin\psi_i\Big] + 2\dot{q}_\theta \dot{q}_i \gamma r_t\, r \cos\alpha\Big)\, dm \tag{4.2}$$

Evaluating the mass integrals gives

$$\begin{aligned} T_i = {} & \frac{1}{2} M_b (\dot{q}_x^2 + \dot{q}_y^2) + \frac{1}{2} I_b \dot{q}_\theta^2 + \frac{1}{2} m_o \dot{q}_i^2 \\ & + \dot{q}_\theta S_b \Big[\dot{q}_y \cos\psi_i - \dot{q}_x \sin\psi_i\Big] \\ & + \dot{q}_i m_2 \cos\alpha \Big[\dot{q}_y \cos\psi_i - \dot{q}_x \sin\psi_i\Big] + \dot{q}_\theta \dot{q}_i m_1 \cos\alpha \end{aligned} \tag{4.3}$$

where the integrals are defined as

$$\int dm = M_b \qquad \int r_t \gamma^2 \, dm = m_o$$

$$\int r dm = S_b \qquad \int r_t \gamma \, r \, dm = m_1 \tag{4.4}$$

$$\int r^2 dm = I_b \qquad \int r_t \gamma \, dm = m_2$$

where the limits of integration go from r_h to r_t. The integrals in Equation (4.4) are respectively the contribution of the blade to the system mass (M_b), static imbalance (S_b) and moment of inertia (I_b), the blade modal mass (m_o) and the consistent mass terms of the coupling of the blade with the rotation (m_1) and translation (m_2) of the disk.

The kinetic energy of a uniform disk reduces to

$$T_d = \frac{1}{2} (\dot{q}_x^2 + \dot{q}_y^2) M_d + \frac{1}{2} \dot{q}_\theta^2 I_d \tag{4.5}$$

If the center of the disk is restrained by translational and rotary springs, the potential energy is

$$U_d = \frac{1}{2} K_x q_x^2 + \frac{1}{2} K_y q_y^2 + \frac{1}{2} K_\theta q_\theta^2 \tag{4.6}$$

and each blade has a potential energy

$$U_i = \frac{1}{2} k_i q_i = \frac{1}{2} m_o \omega_o^2 q_i^2 \tag{4.7}$$

where ω_o is the cantilevered natural frequency.

Substitution of equations (4.3), (4.5), (4.6), and (4.7) into Lagrange's equation yields the equations of motion as expressed in individual blade coordinates.

$$M_T \ddot{q}_x + K_x q_x - \sum_{i=1}^{N} \left\{ \ddot{q}_\theta S_b \sin \psi_i + \ddot{q}_i m_2 \cos \alpha \sin \psi_i \right\} = 0$$

$$M_T \ddot{q}_y + K_y q_y + \sum_{i=1}^{N} \left\{ \ddot{q}_\theta S_b \cos \psi_i + \ddot{q}_i m_2 \cos \alpha \cos \psi_i \right\} = 0$$

$$I_T \ddot{q}_\theta + K_\theta q_\theta + \sum_{i=1}^{N} \left\{ S_b(\ddot{q}_y \cos \psi_i - \ddot{q}_x \sin \psi_i) + \ddot{q}_i m_1 \cos \alpha \right\} = 0$$

$$m_o \ddot{q}_i + m_2 \cos \alpha \left[\ddot{q}_y \cos \psi_i - \ddot{q}_x \sin \psi_i \right] + \ddot{q}_\theta m_1 \cos \alpha + k_i q_i = 0 \qquad i = 1,2,\ldots,N \tag{4.8}$$

where

$$M_T = M_d + \sum_i M_b$$

$$I_T = I_d + \sum_i I_b \tag{4.9}$$

Note that the translational and rotational equations are coupled through the combined imbalance of the blades and the motion of the blades. The blade motions do not couple to each other directly, but through the inertial coupling of the disk represented by the $m_1 \cos \alpha$ and $m_2 \cos \alpha$ terms.

The equations of motion as expressed in equation (4.8) are very general. They will be used in simplified form to examine the cases of extreme mistune of the disk. The equations are highly coupled through the disk rigid body modes, making them difficult to work with. For uniform blades, the equations can be simplified considerably by transforming to

generalized multiblade coordinates, which for an odd number of blades N are

$$q_i = \sum_{n=1}^{\frac{N-1}{2}} a_n \sin n\psi_i + \sum_{n=0}^{\frac{N-1}{2}} b_n \cos n\psi_i \tag{4.10}$$

Substitution of this expression for q_i into the first three equations of set (4.8), and carrying out the sums in i gives

$$M_T \ddot{q}_x + K_x q_x - \ddot{a}_1 \frac{N}{2} m_2 \cos\alpha = 0 \tag{4.11}$$

$$M_T \ddot{q}_y + K_y q_y + \ddot{b}_1 \frac{N}{2} m_2 \cos\alpha = 0$$

$$I_T \ddot{q}_\theta + K_\theta q_\theta + \ddot{b}_o N m_1 \cos\alpha = 0$$

Upon substitution of the expression for q_i in (4.10) into the last N equations of set (4.8), multiplication by successive values of $\cos n\psi_i$ and $\sin n\psi_i$ and summation over i gives the N new equations

$$N m_o \ddot{b}_o + N k_i b_o + \ddot{q}_\theta N m_1 \cos\alpha = 0$$

$$\frac{N}{2} m_o \ddot{a}_1 + \frac{N}{2} k_i a_i - \ddot{q}_x \frac{N}{2} m_2 \cos\alpha = 0$$

$$\frac{N}{2} m_o \ddot{b}_1 + \frac{N}{2} k_i b_1 + \ddot{q}_y \frac{N}{2} m_2 \cos\alpha = 0$$

$$\left.\begin{aligned} \frac{N}{2} m_o \ddot{a}_n + \frac{N}{2} k_i a_n = 0 \\ \frac{N}{2} m_o \ddot{b}_n + \frac{N}{2} k_i b_n = 0 \end{aligned}\right\} \quad n = 2, 3, 4, \ldots, (N-1)/2 \tag{4.12}$$

where the equations have been simplified by the trigonometric summations

valid for n, m $\neq$ N/2, N, 3N/2,..., namely

$$\begin{aligned} \sum_{i=1}^{N} \cos^2 n\psi_i &= \sum_{i=1}^{N} \sin^2 n\psi_i = \frac{N}{2} \\ \sum_{i=1}^{N} \sin n\psi_i \cos n\psi_i &= 0 \end{aligned} \tag{4.13}$$

A high degree of uncoupling has taken place by transformation to multiblade coordinates. To emphasize this uncoupling, the equations in sets (4.11) and (4.12) can be rewritten

$$\begin{bmatrix} M_{T_1} & -\frac{N}{2} m_2 \cos\alpha \\ \frac{N}{2} m_2 \cos\alpha & \frac{N}{2} m_o \end{bmatrix} \begin{Bmatrix} \ddot{q}_x \\ \ddot{a}_1 \end{Bmatrix} + \begin{bmatrix} K_x & 0 \\ 0 & \frac{N}{2} k_i \end{bmatrix} \begin{Bmatrix} q_x \\ a_1 \end{Bmatrix} = 0$$

$$\begin{bmatrix} M_T & \frac{N}{2} m_2 \cos\alpha \\ \frac{N}{2} m_2 \cos\alpha & \frac{N}{2} m_o \end{bmatrix} \begin{Bmatrix} \ddot{q}_y \\ \ddot{b}_1 \end{Bmatrix} + \begin{bmatrix} k_y & 0 \\ 0 & \frac{N}{2} k_i \end{bmatrix} \begin{Bmatrix} q_y \\ b_1 \end{Bmatrix} = 0$$

$$\begin{bmatrix} I_T & N m_1 \cos\alpha \\ N m_1 \cos\alpha & N m_o \end{bmatrix} \begin{Bmatrix} \ddot{q}_\theta \\ \ddot{b}_o \end{Bmatrix} + \begin{bmatrix} k_\theta & 0 \\ 0 & N k_i \end{bmatrix} \begin{Bmatrix} q_\theta \\ b_o \end{Bmatrix} = 0$$

$$\left.\begin{aligned} m_o \ddot{a}_n + k_i a_n &= 0 \\ m_o \ddot{b}_n + k_i b_n &= 0 \end{aligned}\right\} \qquad n = 2, 3, \ldots, \frac{N-1}{2} \tag{4.14}$$

Transformation to multiblade coordinates has reduced the completely coupled set of (4.8) to three sets of two coupled equations each and N-1 simple single degree of freedom equations. It can be seen that the sine and cosine modes (a_1 and b_1) couple to the translational rigid body modes of the disk. The collective or cos0Θ mode couples only to the rotational degree of freedom of the disk, and all higher modes are not coupled through the disk.

The implications of this simple rigid body coupling for the calculation of the aerodynamic forces acting on the blade are enormous. The second equation of each of the first three pairs in set (4.14) parallels equation (3.2). Thus, if the modal displacements (b_0,a_1,b_1) are known and the in plane translational and rotational acceleration of the disk are measured, the modal forces acting on the cos0Θ, sinΘ and cosΘ modes can be directly calculated. The last N-1 equations of set (4.14) resemble the even simpler equation (3.1), and with knowledge of the modal displacements, the modal forces can be calculated without any information about the disk motion.

It remains to be shown that this disk inertial coupling model is sufficient to characterize the dynamics of the MIT Rotor. The remainder of this chapter describes the method used to determine the constants in Equation (4.14) using a well-tuned rotor. Then, two experiments will be discussed in which severe mistune was introduced to check and verify the model.

4.3 Experiments with a Tuned Rotor

A series of tests was performed on the tuned MIT Aeroelastic Rotor to determine its mass and stiffness properties and compare its resonant modes

with those predicted by the proposed model. The rotor was mounted to a short steel shaft, machined with the same taper and keyway as the shaft on which the rotor was mounted in the Blowdown Facility. This short shaft was then mounted directly to the head of a Ling Model 420 electromagnetic shaker designed to produce a peak force of 100 pounds. Excitation of the rotor to determine resonances was sometimes achieved by the shaker through the mounting shaft. In other cases, a loud speaker was used to acoustically excite the blades directly. Amplitudes of response were monitored with the rotor strain gauges and PZT's and with blade and disk mounted accelerometers.

First the mass properties of the rotor as defined by equations (4.14) were determined. The dimensions of the aluminum rotor and blades were carefully measured using calipers. These dimensions were used to calculate the mass and rotary moment of inertia (M_T and I_T) of the rotor. As a check, the calculated mass agreed within 2% of the measured mass, which is well within the accuracy of the measurement. The blade mass properties (m_0, m_1, m_2) were based on the measured dimensions and holographic measurements of the first bending mode made while the rotor was not rotating. The dimension and mass properties for the blade first bending mode are summarized in the Appendix.

One more required constant can be estimated from the rotor geometery, the angle between the plane of the disk and the normal to the camber line (Figure 4-1). For the blades of the MIT Rotor, this angle varies from about 30° at the root to 60° at the tip. The effective angle around which the blade flexes must lie between these limiting values. Reference 1 (page 23) cites the normal to the chord at 20% span height outboard of the root

attachment as the effective flexural axis of such blades in first bending mode. A value of 36° was measured for this location and will be used in further calculations.

The remaining constants to be determined were the stiffness of the hub restraint (K_x, K_y, K_θ) and blade (k_i). Rather than measure these directly, it was decided to search for the resonances suggested by the model and calculate the values of the stiffness using the mass properties and observed frequencies.

Before any resonance tests were performed, the rotor was tuned in much the same way as a string instrument. In designing and installing the piezoelectric crystal assembly, it was observed that by selectively tightening the retaining bolt, a variation of about 6 Hz could be achieved in the frequency of the blade's first bending mode. It was impossible to simply tune any given blade due to the participation of all the other blades through the disk coupling. To isolate a given blade, all the other blades in the rotor were weighted at the tip by a two inch "C" clamp, which pulled the resonance of the weighted blades well below 200 Hz. The resonance of the single unweighted blade could then easily be identified and adjusted. In this way, the blades were tuned to 378 $\pm$ 2 Hz

With the rotor thus tuned, scans were made for overall blade-disk resonances and their modal patterns. Using the shaker excitation, a strong resonance was found at 374.5 Hz with no distinct modal pattern, and a second at 417-418 Hz. In this second resonance, all blades moved in phase. The disk moved in a rotational sense opposite in direction to the blade tips. This mode was referred to as the counterrotating mode. Under acoustic excitation, the modes at 374 Hz and 417 Hz were found, plus an

additional mode at 390-394 Hz. In this mode, the countertranslating mode, the tip displacement pattern was observed to go as $\sin\Theta$, and the disk translated in the sense opposite that of the blade tips.

The countertranslating mode is the one associated with the first two equations of set (4.14). If the base translation stiffness (K_x) is set to zero, and the proper blade cantilever frequency is used (to be discussed shortly), the calculated frequency of the $a_1\sin$ and $b_1\cos$ modes is 381 Hz. But the shaft mounted on the shaker provides a finite restraining spring. To move this resonance from 381 Hz to 390-394 Hz, K_x must have a value of 3×10^6 to 3.5×10^6 lb/ft. If this were the right value, the second mode associated with these equations, the translating mode in which the blades and disk move in phase rather than out of phase, would have a resonance in the range of 280 Hz to 302 Hz. A weak resonance with this modal structure was found in this range. The values of K_x and K_y will be taken as $3 - 3.5 \times 10^6$ lb/ft.

Similarly, the counterrotating mode is associated with the third equation of set (4.14). With K_θ set to zero, the predicted frequency is 417.2 Hz, within the observed range. However, a weak rotating resonance was observed at 40 Hz, suggesting a small, but nonzero, torsional stiffness of 1.5×10^4 lb ft/rad. This only moves the calculated counterrotating frequency to 417.7 Hz, and will be included in subsequent calculations.

The strong resonance at 374.5 Hz was found to be the true blade cantilever natural frequency, as given by the last N-1 equations of set (4.14). However, when the blades were tuned individually, they resonated at an average of 378 Hz. This difference of 3.5 Hz is associated with the participation of the disk. When the blades were tuned only one blade was

excited at a time and the disk participated in the motion. This observed natural frequency was not based on the modal mass of the blade, but on the reduced mass of the blade disk system. With all the blades free to vibrate, some combination of the higher modes (cos 2θ, cos 3θ,...) was excited; the disk did not participate and the real blade cantilever frequency was observed. In Section 4.5, the difference between the blade modal mass and blade-disk reduced mass will be shown to lead to a difference of 3.5 Hz in first bending frequency.

As a final test on the tuned rotor, the structural damping of single blades was measured by the half power bandwidth technique. Just as in the tuning process all the blades but one were weighted, and the response of the unweighted blade to constant amplitude excitation was measured. In this way, the structural damping in air of individual blades was found to have a Q ranging from 190 to 240 with an average value of 210. This corresponds to an average log decrement of 0.015 or a critical damping ratio of 0.0024. The combined material and structural damping only lightly damp the motion of the blade.

4.4 Severely Mistuned Rotor with Several Blades Participating

In the process of tuning each blade of the rotor weights were clamped to the tips of all the other blades. This process can be thought of as introducing a severe mistune into the rotor, in this case to isolate the resonance of a single blade. This method of creating a severe mistune was used in two additional ways. In one case, two blades were left unweighted and their natural frequencies were determined as a function of the angle that separated them. These results will be described in Section 4.4. In

the second case, between one and twenty-three adjacent blades were left unweighted. A study was made of how the observed frequency changed with an increasing number of participating blades.

The blades were weighted by a 2 inch steel "c-clamp" near the tip. Between the contact points of the clamp and the metal surface of the blade was a small piece of 1/8 inch thick hard rubber mat to prevent the clamp from slipping or chattering. With this weighting, the blades were observed to have a very well damped resonance in the range of 160 to 180 Hz, well below the unweighted resonance of 374 Hz.

When only one blade was unweighted, its single natural frequency was near that to which the blades were tuned, 378 Hz. When two or more blades were unweighted, two strong resonances were found. At the blade cantilever frequency of 374 Hz, the blades moved without any noticeable phase relation. At a higher frequency, the blades were observed to move in phase. This natural frequency was found at 381 Hz for two blades and monotonically increased with increasing number of blades unweighted. As the number of blades approached 23, the observed frequency approached the counterrotating mode of the tuned rotor at 418 Hz. The trend of the highest resonant frequency versus participating blades can be seen from the experimental data in Figure 4-2.

This highest mode resonance of the mistuned rotor can be modelled by assuming two modes for the blade displacements whose amplitudes are q_A and q_B. The J unweighted blades respond at equal amplitude and in phase and are symmetrically distributed about $\Theta = 0°$ such that for a blade at $\psi_i = 2\pi i/N$, the displacement is

$$q_i = q_A \qquad i = \frac{1-J}{2},\ \frac{1-J}{2}+1,\ \ldots,\ \frac{J-1}{2}-1\ \ \frac{J-1}{2} \tag{4.15}$$

The remaining K weighted blades respond at equal amplitude and in phase and are symmetrically distributed about $\Theta = 180°$ such that

$$q_i = q_B \qquad i = \frac{J-1}{2}+1,\ \frac{J-1}{2}+2,\ \ldots,\ N-\frac{J-1}{2}-2,\ N-\frac{J-1}{2}-1 \tag{4.16}$$

where

$$J + K = N$$

To derive the equations of motion for this untuned case, the two assumed modes q_A and q_B are substituted into equation set (4.8). The summations in the first three equations and over the last N equations are divided into sums over the K weighted and J unweighted blades. The resulting equations are

$$\begin{aligned}
&M_T \ddot{q}_x + K_x q_x = 0 \\
&M_T \ddot{q}_y + K_y q_y - \sigma S_w \ddot{q}_\theta - \sigma \ddot{q}_B m_2' \cos\alpha \\
&\qquad + \sigma \ddot{q}_A m_2 \cos\alpha = 0 \\
&I_T \ddot{q}_\theta + K_\theta q_\theta - \sigma S_w \ddot{q}_y + K' \ddot{q}_B m_1' \cos\alpha \\
&\qquad + J \ddot{q}_A m_1 \cos\alpha = 0 \\
&J m_o \ddot{q}_A + \sigma m_2 \ddot{q}_y \cos\alpha + J m_1 \ddot{q}_\theta \cos\alpha + J k_i q_A = 0 \\
&K m_o' \ddot{q}_B - \sigma m_2' \ddot{q}_y \cos\alpha + K m_1' \ddot{q}_\theta \cos\alpha + K k_i q_B = 0
\end{aligned} \tag{4.17}$$

where the blades have been assumed to be uniform except for the presence of

the weights at the tips. The mass properties of the weighted blades are given in a form similar to equation set (4.4) as

$$\int r_t^2 \gamma^2 \, dm = m_o' \qquad \int r_t \gamma \, dm = m_2' \qquad (4.18)$$

$$\int r_t \gamma r \, dm = m_1' \qquad M_w r_w = S_w$$

the last term representing the contribution to the static imbalance by a weight of M_w at radius r_w. The total rotor mass and inertia terms must also reflect the addition of weights at the tips. The term σ is defined as the partial sum

$$\sigma = \sum_J \cos \phi_i \qquad (4.19)$$

where the summation over the J blades represents the indices in equation (4.15). It can be shown that

$$-\sigma = \sum_K \cos \phi_i \qquad (4.20)$$

where the summation is over the K blades of the indices in equation (4.16). Note that since the displacements were assumed to be symmetric about the x axis, the x equation has uncoupled from the remaining four.

The solution to the last four equations of set (4.17) is shown in Figure 4.2 for the range of experimentally determined elastic constants. The agreement between the experimental results and those predicted by the model for this assumed mode are excellent. In particular, note that the model reproduces the dip in the resonance curve in the range of 15 to 20 blades unweighted. The lower end point for zero blades is the true can-

tilever frequency of the blade and the upper end point with all 23 blades unweighted is that of the in-phase mode found for the perfectly tuned rotor. In the range of 1 to 5 blades participating, the trend is nearly linear. When the first blade is unweighted, the reduced mass effect of the disk causes an increase in the observed resonance of about 3 Hz. As the next few adjacent blades are unweighted, the effective modal mass of the blades increases, growing closer to that of the disk. This increases the reduced mass effect and the increment in frequency. Once the participating blades subtend a large angle, the translational coupling begins to be reduced and the trend curves over.

A simplification can be made to equations (4.17) if the weighted blades are simply ignored, that is, they are assumed not to participate in the motion, and that the additional mass of the weights at the tips is not significant. With these assumptions, the last of the five equations of set (4.17) is removed, q_K and S_w are set to zero and the remaining three equations are less highly coupled. Solutions of this simplified set of equations for the in-plane resonance are shown in Figure 4-3. This agreement is also quite good. In this case, simply ignoring the mass of the weights and participation of the weighted blades still gives reasonable results.

4.5 Severely Mistuned Rotor with Two Blades Participating

In this second set of experiments with severe mistune, two blades were left unweighted. The angle subtended by the two blades was varied so that the blades were first adjacent, then separated by one weighted blade, then

two and so on until the unweighted blades were on opposite sides of the rotor.

For each location of the two blades, two distinct resonances were found, one in which the blades moved in phase, and one in which they moved out of phase. When the blades were adjacent, the out of phase mode was found at the true cantilever frequency of the blades (374 Hz). The out of phase motion of the blades cancelled the participation of the disk. The in phase mode was found at about 381 Hz, 7 Hz above the cantilever frequency. This difference is just twice the increase in observed natural frequency caused by the reduced mass effect of the disk acting on a single blade. As the spacing of the two active blades increases, the two observed frequencies tend to coalesce as shown in Figure 4-4. The error bars in the data represent several different pairs of blades tested for each angular separation.

Once again, this mistune can be modelled by assuming two modes for the displacement of the two blades. As in the simplified analysis at the end of section 4.4, the weighted blades will be assumed to have no displacement and the mass of the clamps will be ignored. Then the displacement of the two blades participating in the motion at plus ϕ_i and minus ϕ_i can be given as the sum and difference of an in phase and out of phase mode

$$q_i = \frac{q_{IP} + q_{OP}}{2} \qquad \text{at} \quad + \phi_i$$

$$q_i = \frac{q_{IP} - q_{OP}}{2} \qquad \text{at} \quad - \phi_i \tag{4.21}$$

where ϕ is one half the angle subtended by the two blades.

Substitution of the displacements expressed above into equations (4.8) gives

$$
\begin{aligned}
&M_T \ddot{q}_x + K_x q_x - \ddot{q}_{OP} m_2 \cos\alpha \sin\phi = 0 \\
&M_T \ddot{q}_y + K_y q_y + \ddot{q}_{IP} m_2 \cos\alpha \cos\phi = 0 \\
&I_T \ddot{q}_\theta + K_\theta q_\theta + \ddot{q}_{IP} m_1 \cos\alpha = 0 \\
&m_o \ddot{q}_{IP} + k_i q_{IP} + 2\ddot{q}_y m_2 \cos\alpha \cos\phi \\
&\qquad + 2q_\theta m_1 \cos\alpha = 0 \\
&m_o \ddot{q}_{OP} + k_i q_{OP} - 2\ddot{q}_x m_2 \cos\alpha \sin\phi = 0
\end{aligned}
\tag{4.22}
$$

The symmetry of the in and out of phase modes about the x axis has caused an uncoupling of the equations of motion. It can be seen that the first and last of set (4.22) completely determine the out of phase resonance and lead to the lower curve of Figure 4-4. The middle three equations are coupled and determine the in phase resonance responsible for the upper curve of Figure 4-4.

Within the uncertainty concerning the disk restraint stiffness, the agreement with experimental results is again excellent. Both branches of the response and their coalescense are predicted correctly. Examination of equations (4.22) shows the origin of this coalescence. The first and last equations are coupled through a term expressing the translational coupling which depends on sin ϕ. For adjacent blades, ϕ is near zero and the true cantilever frequency is observed. As ϕ moves towards 90°, the equations are increasingly coupled with a resulting upward shift in resonance. The

middle three equations are coupled through translational terms which depend on cos ψ and rotational terms which have no ψ dependence. At small values of ψ both are present. As ψ approaches 90° the translational terms go to zero, reducing the coupling, but the rotational coupling still keeps the observed resonance above the cantilever frequency. If the magnitude of the translational and rotational coupling are the same, as they are in the MIT Rotor, the two frequencies tend to coalesce as ψ approaches 90.

4.6 Summary

A structural model has been developed and demonstrated in which the coupling of the blade motion is caused by the inertia of the disk. The model correctly predicts the behavior of the real rotor even in the case of severe mistune. Although present in all rotors, this inertial coupling appears to dominate in the case of the MIT Rotor.

The model simplifies the interpretation of the aeroelastic data that follows in two ways. First the higher multiblade modes (cos 2θ, sin 2θ, cos 3θ, etc.) are unaffected by the motion of the disk. Therefore the response of these modes can be calculated in the absence of any information about the disk. The three lowest modes are coupled by the translational and rotational motion of the disk. These are quantities which can be measured using disk mounted accelerometers as are included in the MIT Rotor.

Transformation of the equations of motion developed can be achieved by letting the location of the blade depend on time such that

$$\psi_i = \frac{2\pi}{N} i + \Omega t \qquad (4.23)$$

where Ω is the rotation rate. This transformation has two effects on the equations derived for a tuned rotor expressed by Equations (4.8). A centrifural stiffening term is added in the blade bending stiffness k_i, which raises the cantilever frequency to 410 Hz at full speed. A gyroscopic coupling term appears which couples the two translational degrees of freedom of the disk. This gyroscopic coupling leads to whirling of the disk and blades [29]. When run at full speed in a vacuum, a forced vibration of the blade was observed due to one modal diameter which occurred at one, two, and three times the rotor rotation speed. This effect must be included in the analysis of the aeroelastic response at these frequencies and in these modes.

5. FORCED VIBRATION DUE TO UPSTREAM DISTURBANCES

5.1 Stage Performance and Aerodynamic Response

Since no aeroelastic stability boundaries were encountered within the performance map of the MIT Transonic Compressor Rotor, it was decided to study the response to forced vibration at the design point. There, the steady aerodynamic performance of the rotor is understood and well documented [19]. The secondary flow injector system described in Section 2.1.3 is used to create a disturbance upstream of the rotor. The disturbance extends part way through the period of quasi-steady flow during which time the forced vibration response of the rotor can be determined. Then the disturbance is sharply ended and the subsequent ring down of the rotor is a measure of the aerodynamic plus structural damping.

Several attempts were made before the flow injector successfully created a steady disturbance. At first, the downstream throttle orifice was chosen so that the rotor would operate at its design point when run at 100% speed. The disturbance was scheduled to turn on at the start of the test and off at 80 msec or 30 msec into the quasi-steady flow. The total pressure of the injected flow was 200 psia. This strong disturbance drove the stage into a two cell rotating stall from which it did not recover during the test. To correct this, the throttle was opened to move the operating line away from the stall boundary, the beginning of gas injection was delayed until the start of the quasi-steady flow at 50 msec, and the injector pressure was reduced to 60 psia. This combination created no clear excitation of the blades. In the third attempt, the throttle and start time were left unchanged, but the supply pressure was increased to

150 psia. This combination succeeded in creating a disturbance with a clearly observable aeroelastic response which will be discussed below.

The steady operating point of the rotor was on the 100% speed line just below the design point, with a flow corrected to air at standard conditions of 77 lb/sec (35 Kg/sec), and a tip Mach number of 1.23. A total pressure ratio of 1.57 was measured by the 5 way probe at the 94% tip radius. This is less than the pressure ratio of 1.70 measured by Durali [19] at this radius at the design point. This would be expected since the throttle orifice was larger than that for design. However, the corrected mass flow of 77 lb/sec calculated from the rate of pressure decrease in the supply tank is also less than Durali's measured value of 84.7 lb/sec. This discrepancy can be accounted for by an inaccuracy in the supply tank volume and calculation procedures used by Durali.

The aerodynamic response of the rotor to the upstream disturbance can be seen in a change in bow shock strength. Figure 5-1a shows the trace of the high frequency response wall static pressure transducer 0.1 chord upstream of the rotor at the 0° instrument location directly behind one of the injectors. An increase in the bow shock strength can be seen starting at about 55 msec and ending at 100-102 msec. During this period, when the injector is on, a region of velocity defect is created behind the injector. As a blade passes through this region, the incidence increases, and with it the local shock strength. Comparison with Figure 5-1b taken from a wall static transducer 1.0 chords upstream at the 72° instrument location (i.e. far from the injectors at 0° and 180°) shows no corresponding change in shock strength.

5.2 Aeroelastic Response of the Individual Blades

The individual response of all 23 blades is shown in Figure 5-2. The blades are shown in their proper relative positions around the rotor. The signal from blade 23 is shown twice for reference, once at position zero and again at position 23. The reference time is that time when the diaphragm is commanded to burst. From this presentation of the data, some overall trends can be seen. The rotor spins in vacuum until 3 msec when the wavefront of the gas expanding into the test section subjects the rotor to an almost impulsive loading. A complex and large amplitude response continues until about 50 msec, when the first bending frequency becomes dominant in a response which locally has some phase coherence. From 70 to 100 msec the first bending mode appears to damp and a higher frequency grows, that of the second bending mode. After 100 msec, the second bending response decays and the first bending re-emerges.

Other than these general observations, it is difficult to gain any qualitative understanding of the response as it is shown in Figure 5-2. The first step in reducing the data is to determine the frequency content of the response by performing Fast Fourier Transform (FFT) in time of individual blade signals. Fourier transforms of blade 3 response are shown in Figure 5-3 for the period when the injector is on, and in Figure 5-4 for the period after the injector is turned off. Both figures indicate that the amplitude of response is concentrated in distinct frequencies: at low frequency less than 50 Hz, at about 150 Hz, at 300 Hz, in a band from 400 to 500 Hz, and at 1140 Hz. These spikes correspond to the low frequency response due to the blowdown transient, the first, second and third engine orders, and the second blade bending frequency at the eighth engine order.

The next step in the data reduction is to narrow bandpass filter the

total response of each blade to isolate each of the frequencies indicated. This is done digitally using a Nearly Equal Ripple digital filter [30]. The filter parameters typically used included a transition width at the edge of the pass band of 70 Hz and a loss outside of the pass band of 50 dB. Figure 5-5 shows the original data for blade 1 as well as its components derived from low pass filtering the raw data below 100 Hz, and in the ranges 100 - 220 Hz to isolate the first engine order, 220 - 350 Hz to isolate the second engine order, 350 - 750 Hz which contains the bulk of the first bending response, and 750 - 1500 Hz which contains the second bending response. Little response of interest is contained in the two lowest frequency ranges in the period of quasi-steady flow.

The bandpass filtered responses for the last three frequency ranges are shown for all the blades in Figures 5-6, 5-7 and 5-8. The components of the blade displacement data at the second engine order (Figure 5-6) should show some sign of response to the flow injector since a two per revolution disturbance fixed in tunnel coordinates would be seen by the rotor at this frequency. While the amplitude of response is on average greater prior to 100 msec than after 100 msec, no clear pattern or phase relation emerges. The situation is only slightly more clear in the response at the first bending frequency (Figure 5-7). Here certain "patches" of response have uniform amplitude and phase relation, such as the group of blades 1-8 from 50 to 70 msec and 16-22 from 60 to 80 msec. Again, no clear demarcation of the response before and after termination of the disturbance is evident. The response at second bending frequency (Figure 5-8) does show a rise in amplitude prior to 100 msec and a decay thereafter for most blades, but no global pattern is evident.

At this point, the analysis can proceed in two ways. Either a detailed study can be made of the individual blade data, or a transformation can be made to disk modal or multiblade coordinates. Since the aerodynamic damping is expected to depend on the global property of interblade phase angle, the transformation to multiblade coordinates will be made.

5.3 Aeroelastic Response of the Multiblade Modes

The values of the multiblade coordinates as described in Section 3.2 can be calculated from the individual blade coordinates by performing at each instant in time a Discrete Fourier Transform in theta such that

$$
\begin{aligned}
b_o &= \frac{1}{N} \sum_{i=1}^{N} q_i \\
a_n &= \frac{2}{N} \sum_{i=1}^{N} q_i \sin n\phi_i \\
b_n &= \frac{2}{N} \sum_{i-1}^{N} q_i \cos n \phi_i
\end{aligned}
\tag{5.1}
$$

where a_n and b_n are the generalized multiblade coordinates defined by Equation (3.11). In this way, the information contained in the displacements of 23 individual blades has been transformed to the generalized displacements of 12 cosine modes (cos0θ, cos1θ, ..., cos11θ) and 11 sine modes (sin1θ, sin2θ, ..., sin11θ). The transformed data for the frequency ranges of interest corresponding to Figures 5-6, 5-7 and 5-8 is shown in Figures 5-9, 5-10 and 5-11. The global nature of the response is much more apparent from examination of the amplitudes of the multiblade modes. Figure 5-9 reveals that for the frequency range around second engine order

(220-350 Hz), the motion of the blades is primarily a superposition of the lowest seven modes, the in-phase mode ($\cos 0\theta$) and the $\sin 3\theta$ and $\cos 3\theta$ modes appear in bursts which are unrelated to the upstream excitation. However the one and two modal diameter modes clearly respond to the excitation. The $\sin\theta$ and $\cos\theta$ modes decay in the time period up to 100 msec. After that time, the two modes grow with the same amplitude envelope and with a temporal phase relation such that the cosine mode lags the sine mode by 90 degrees. The two modal diameter modes are the pair which should respond most strongly to the two per rev disturbance, and this is seen to happen. Through the entire test time from 50 to 150 msec, the $\sin 2\theta$ and $\cos 2\theta$ have similar amplitude and are temporarily 90 degrees out of phase.

As was discussed in Section 3.2, the condition that the sine and cosine modes have the same amplitude and are 90 degrees out of phase is synonymous with a travelling wave with a fixed amplitude and interblade phase angle. In both the cases of the $\sin\theta$ and $\cos\theta$ modes, and the $\sin 2\theta$ and $\cos 2\theta$, the cosine mode lags the sine mode 90 degrees. This translates to a rearward travelling wave in rotor coordinates.

With an interblade phase angle

$$\beta = -\frac{2\pi n}{N} \tag{5.2}$$

the blade displacements are

$$q_i = A \sin \omega t \sin n\phi_i - A \cos \omega t \cos n \phi_i \tag{5.3}$$

where n is the number of modal diameters. The wave speed of this travelling wave is

$$\nu = \pm \frac{\omega}{n} \tag{5.4}$$

where has a forward sense for a positive interblade phase angle and a rearward sense for a negative interblade phase angle.

The travelling blade displacement pattern given by the sin2Θ and cos2Θ modes has an interblade phase angle of -31.3 degrees. Since the observed frequency is exactly twice the engine speed, the wave speed in rotating coordinates given by Equation (5.4) is just - Ω. In rotor coordinates, the displacement pattern travels backward at Ω . By a stationary observer, this would be viewed as a standing wave and is therefore the forced response to the fixed upstream disturbance. The observed response fluctuates in amplitude in the interval from 60 to 100 msec, but from 100 to 120 msec, there is a smooth decay from a higher to a lower amplitude of response.

There is not a resonance of the blade disk system at this frequency, so the continued response indicates some lower level two per revolution excitation must be present after 100 msec when the injector system shuts off. Since it was shown in Chapter 4 that structural and shaft vibrations cannot excite this two modal diameter mode, the source of this disturbance must be an innate 2Θ nonuniformity in the flow in the facility. However, the smooth decay between two levels of excitation can be used to determine the total damping. With a knowledge of the structural damping, the aerodynamic damping for this interblade phase angle and reduced frequency can be calculated. The numerical values of these parameters are listed in the summary at the end of this chapter.

The response of the one nodal diameter mode (cosΘ, sinΘ) is also a

backwards travelling wave disturbance with an interblade phase angle of -15.6 degrees and a wave speed of $-2\ \Omega$ in rotor coordinates or $-\ \Omega$ as viewed by a fixed observer. This is therefore not the response to any fixed disturbance. The response builds up from a lower level at 100 msec to a higher level at 120 msec. It then remains about at this level as if responding to a fixed amplitude excitation. The source of this excitation is probably the second engine order excitation of the backward whirling mode of the blades and disk, as is observed in a vacuum (Section 4.6). Again, an estimate of damping can be made from the time constant of the transition from a lower to a higher amplitude of response.

The amplitudes of the multiblade coordinates for the component of the response which includes blade first bending frequency is shown in Figure 5-10. The lowest nine modes ($\cos 0\Theta$, $\sin\Theta$, ...$\cos 4\Theta$) meet the criteria of significant amplitude of response, similar envelopes of response of the sine and cosine modes, and 90 degree phase lag of the cosine mode. While all nine show some response to the turn on or off of the injector, only the $\sin 3\Theta$ and $\cos 3\Theta$ modes have a response from which a damping estimate can be made. This mode has an interblade phase angle of -50.0 degrees, and again a wave speed of $-\ \Omega$ giving a fixed pattern of blade deflection as viewed by a stationary observer. This is a forced response to a steady 3Θ aerodynamic disturbance which has its origins in the interaction of the boundary layer bleed and three struts which support the forward centerbody (Figure 2.3). This response is present in every run, with or without the gas injector system present.

The interaction between the fixed 3Θ disturbance and the controllable 2Ω disturbance can be seen at two times in the test. Prior to about 60

msec, the response is large. When the 2Θ disturbance is turned on at about 55 msec, the three nodal diameter response diminishes sharply. When the injectors are turned off at 100 msec, the response grows. From this growth after 100 msec, the damping listed in the summary is calculated. The explanation of this response pattern is as follows. Prior to injector turn on, the three struts create wakes at 60, 180 and 300 degree locations. The third circumferential Fourier component of this distortion pattern is dominant, and the rotor sees an excitation at 3 Ω (435 Hz). Since this is close to blade first bending frequency (410 Hz), there is a strong response. At 55 msec, the gas is injected and wakes created at 0 and 180 degrees (Figure 2.3). If the wake production and aerodynamic response mechanisms were both linear, the structural response of the cos3Θ and sin3Θ modes would not change in response to the 2Θ excitation. Obviously, the responses do interact such that the third circumferential Fourier component is reduced and the response at 3Θ decreases. When the injector shuts off at 100 msec, the reverse process takes place and the 3Θ component again dominates.

Since there clearly is an interaction of the two per revolution excitation and three per revolution response, there could be a nonlinear mechanism present. Since one gas injector is located directly downstream of one of the struts (at 180 degrees, Figure 2.3), one possible explanation is that the disturbance created by the strut does not combine in a simple linear manner with the disturbance created by the injector. Another explanation is that the unsteady aerodynamic response of the blades is not linear. The actual disturbance that the blade encounters is not a smooth sinusoidal variation in the inlet velocity, but a sharp edge gust whose

width is about one blade chord. If the aerodynamic response were nonlinear the response to such a gust or wake would be different than that predicted by linear superposition of the response to circumferential Fourier components of the gust. Such a nonlinearity would allow the two per revolution excitation and three per revolution response to interact.

At this time, it is not possible to determine if the source of the interaction is in the wake generation mechanism or aerodynamic response. The source of this effect could be isolated by changing the location and number of upstream wake generators. A possible conclusion to be drawn from this is that if an engine has a forced vibration problem due to proximity of an engine order to a blade resonance, it is possible by selectively adding upstream disturbances to change the frequency content of the excitation and reduce the overall response of the blades.

The response of the rotor at second blade bending frequency shows a completely different pattern in the response of the multiblade modes than the two frequency ranges already discussed. Figure 5-11 shows that only the eight nodal diameter modes ($\sin 8\Theta$, $\cos 8\Theta$) respond to the disturbance created by the injector. It has an interblade phase angle of -125 degrees and a wave speed of $-\Omega$. Two injectors located 180 degrees apart in the tunnel will create disturbances at all the even harmonics of the tunnel. The rotor will see the eighth harmonic at eight times rotor rotation speed or about 1160 Hz. Since this is very close to second blade bending, a large response in the eighth multiblade mode results. The response after 100 msec is a decaying free vibration which gives another measurement of aerodynamic damping.

5.4 Summary of Measured Aerodynamic Damping

The techniques developed have been used to estimate four values of the damping for the operating point tested. They are summarized in Table 5-1. These are, in fact, measurements of the total modal damping; aerodynamic plus structural. The value of the modal structural damping can be determined for a rotor spinning in a vacuum and subtracted out to leave only the aerodynamic damping. These modal dampings were not determined in the present investigation. Individual blade structural damping was found to have a log decrement of 0.015 in the first bending mode. Since this is a factor of 10 to 50 less than the total damping, it can be assumed that the principal source of the measured damping is aerodynamic.

6. FORCED VIBRATION DUE TO ROTATING STALL

6.1 Stage Performance

With the stage operating just above its design point, a two cell rotating stall was encountered. The wall static pressure signature from this run is shown in Figure 2-8 and was discussed in Section 2.3. The stall cells were found to rotate at a constant 54% of the rotor speed even though the rotor decelerated during the test time. At the tip, each of the two cells occupied about one-sixth of the rotor circumference. The rotor was operated on the nominal 100% speed line with a measured tip Mach number of 1.22. The mass flow passed by the stage was 66 lb/sec (30 kg/sec), 14% less than the 77 lb/sec measured in the test at 100% speed just below the design point. The total pressure ratio measured at 94% tip radius in the smooth flow between stall cells was 1.70, the same as the pressure ratio measured by Durali for this radius at the design point.

6.2 Response of the Blades

The procedure used for analyzing the structural data was much the same as that described in Chapter 5. Fast Fourier Transforms in time of individual blade signals revealed that the dominant frequencies in the response were a low frequency component below 50 Hz, a component at about the rotor rotation speed, and bands at the blade first bending resonance and second bending resonance. The raw data was then digitally filtered to isolate the response at each of these frequencies. Since this run was made in an earlier series of tests, not all the blade displacement transducers were functioning and recorded. In view of this missing data and the fact that

the forcing due to passage of a stall cell is more a local than a global went, the data was analyzed in terms of the individual blade displacements rather than the amplitudes of the multiblade modes.

Figure 6-1 shows the blade response low pass filtered in the range up to 250 Hz. Again, each trace is in a position corresponding to the circumferential location of the blade. The propagating nature of the disturbance caused by the rotating stall cells can be clearly seen to lock the amplitude signals. The frequency of this response is just the apparent frequency of cell passage which occurs at twice the rotating speed of the cells in rotor coordinates [2 x (1 - 0.54) x Ω = 136 Hz]. Recall that since the rotor decelerates, the stall cell rotation speed slows as a constant fraction of the rotor speed, so the blade forcing frequency drops through the test.

The band pass filtered response at first blade bending frequency in the range from 250 to 750 Hz is shown in the same format in Figure 6-2. Not only is the response of large amplitude, but it is also very closely phase-locked with an interblade phase angle of about -90 degrees. For a 23 blade rotor, this phase angle corresponds to a backward travelling displacement pattern with 6 nodal diameters. If the source of this excitation were linked to the rotating stall cells, the disturbance would be seen in rotor coordinates at 6 x (1 - 0.54) x Ω or about 408 Hz, the measured frequency of response. Since this excitation is just below the first bending frequency it accounts for the strong excitation and phase lock.

A clearer picture of the forcing can be gained by focussing on one blade. Figure 6-3 shows the low frequency, first bending and second bending responses of blade 12, as well as the frequency of the first

bending response. The frequency shown in this last curve is derived by making a least squares fit of a decaying sinusoid to segments of the data about 1.5 periods in length. The center time of the segment over which the fit is made is progressively incremented in time and the process repeated. The derived parameters of the curve which was fit to a segment of data, namely its frequency, amplitude, phase, and time constant of decay or growth, are assigned to the center time of the segment.

Returning to Figure 6-3, the small arrows at the bottom mark the approximate arrival of the leading edge of the stall cell. From each of the responses something can be learned about the nature of the forcing during the passage of the cell, and of the damping while the blade is operating in smoother flow between cells. The second bending response is excited by the leading edge of the stall, and less strongly so at the trailing edge, indicating that the higher frequency content of the disturbance is at its leading edge. This implies the blades stall sharply and recover more gradually. As was pointed out by Bartlett [31] and Day and Cumpsty [32], this difference between the sharp stall cell leading edge and more gradual recovery can also be seen in the wall static pressure (Figure 2-8), if one recalls that in fixed coordinates one sees the trailing edge of the cell go by before the leading edge. In undisturbed flow, the second bending mode appears to be lightly damped.

The low frequency signal shows that the blade springs back from its steady forward loaded position towards its neutral rest position as the cell passes, indicating that the bending load on the blade drops off sharply in the stall cell. Close examination of this top trace in figure 6-3 as well as the traces of the same low frequency range in Figure 6-1

reveals that the signal is periodic with the stall cell passage period but not sinusoidal. For about 60% of the period, the blades are deflected forward by the gas bending loads of unstalled flow. Then for the remaining 40% of the period, the blades begin to relax back to their neutral rest position, then suddenly regain their steady gas bending load. This temporal division in the behavior of the blade corresponds directly to the circumferential distribution of the stall cell which was found to occupy about one third of the annulus at the tip. The conclusion drawn from the phasing of this response to the arrival of the stall cell (Figure 6-3) and its time history is that the "steady" gas bending load drops off sharply during the passage of a stall cell.

6.3 Discussion of the Forcing Due to Stall Cell Passage

Day and Cumpsty [32] have studied the kinematics of the flow within rotating stall cells in axial compressors. While the details of the flow were found to depend on the number of stages, flow coefficient and degree of reaction of the design, there were two traits they found fundamental to the behavior of flow within the stall cell. First, that the net axial flow in the stall cell is much less than that of the mean flow, and second that the tangential velocity of the fluid in the cell is equal to the rotor's, such that "the stalled blades behave like paddle wheels, sweeping the flow in their direction of motion, and not at all in the manner of unstalled airfoils". In rotor coordinates, the average flow within the cell would have little net axial or tangential velocity although in any part of the cell, the velocity is non-zero.

The influence that the flow field within the stall cell would have on

the blade bending load is uncertain. Attention must be paid to the interruption of the primary flow and the creation of secondary flows in the cell. If one considers the net or specially averaged flow velocities, the flow is nearly at rest in rotor coordinates. This reduction in the net relative dynamic pressure would suggest an unloading of the blade as the blade stalls and a reloading as the blade recovers. However, the presence of secondary flow within the stall cells, and in particular the drift of flow into and out of the rotor at the front of the passages, may cause a redistribution of loading on the blading.

This redistribution of load can be measured in two ways, as a change in torque on the rotor, and as a change in bending load on the blades. Note that these two measurements are not synonymous. Torque is the product of load times radius from the axis of rotation and can only be measured as an average over the rotor. Bending moment is the product of load and distance from the hub radius and can be measured for each blade. For moderate and low aspect ratio (high hub to tip ratio) stages, this is an important distinction. In particular, if the loading in a stall cell decreased on the tip and increased in the root area, the torque could be unaffected, but the bending load would decrease. Direct measurements of the torque were not made on the MIT Rotor, but the bending load was found to decrease in the stall cell as the blades relaxed back to their unloaded position. As the blade emerged from the stall cell, it recovered its steady load.

That this redistribution of load is a quasi-steady aerodynamic process can be inferred by comparing the duration of the stall cell passage to the through flow time of the undisturbed flow and the lowest blade natural frequency. The length of time any one blade remains stalled corresponds to

the duration of the stall cell passage as seen in rotor coordinates. For the MIT Rotor, this is $1/[6 \times (1 - 0.54) \times \Omega]$ or 2.4 msec. The flow time through the passage of undisturbed flow ($c/V\omega$) is 0.26 msec. Thus for about ten through-flow times, the blades sit in the cell.

Returning to the first bending response in Figure 6-3 and focussing on the four cell passage events "from 80 to 110 msec" it is clear that once every three cycles the blade is forced by the stall cell, and in the remaining time it rings down. The frequency is seen to drop just as the cell arrives and peak just as the blade unstalls, oscillating approximately between the forcing frequency at the sixth harmonic of the rotating disturbance and the blade natural frequency.

Figure 6-4 shows the modal velocity and force for the same blade, both of which were calculated from the band pass filtered blade displacement data. The velocity was calculated with a simple second order finite difference operator. The force was calculated for the first bending mode using the model of Equation 3.4, with the interaction of the disk set to zero, with the modal mass and stiffness derived in Chapter 4. Great care had to be exercised in calculation of the inertial force since it required twice differentiating numerical data. Second and fourth order finite difference operators were tried, but when the inertial and elastic terms were added, the resulting apparent force was very noisy. Finally, a routine was developed which for any given point fit a fourth order polynomial to seven adjacent points (about one third of a period) by a least squares method. The second derivative was then calculated for the center point from the fit. The force calculated with the curve fitting technique contained less noise at the sampling frequency than that calculated using finite dif-

ference approximations.

The passage of the cell stands out clearly when the force signal is compared to the velocity (Figure 6-4). As the blade stalls then recovers, the forcing is nearly in phase with the velocity. Away from the disturbance the blade damping is just 180 degrees out of phase with the velocity. In a sense, each stall cell passage can be viewed as an experiment to measure the aerodynamic damping. The passage of the cell provides an excitation and locks the phase of the blades to almost exactly -90 degrees. In the clear flow, the blade motion usually decays, and by plotting the modal force versus the velocity, as shown in Figure 6-5, it is clear that the damping force is 180 degrees out of phase with the velocttty. The log decrement measured this way and averaged over the three events from 90 to 110 msec is 0.2.

In this chapter, the technique to calculate the aerodynamic forces acting on a rotor by analysis of individual blade displacements has been demonstrated. Unlike the multiblade method of Chapter 5, this method is best used when the events are of a local nature, or when the data from all the blades is not available for transformation to multiblade coordinates.

7. SUMMARY AND RECOMMENDATIONS

7.1 Summary

1. A method has been demonstrated for the measurement of aerodynamic forcing and damping of a transonic rotor by an inverse solution of the structural dynamic equation of motion. The method is quite general and can be used in the analysis of forced vibration and damping of a rotor in that region of its performance map where the rotor is aeroelastically stable, as well as the behavior in regions of instability. It uses data which is available from conventional strain gauges. In damping studies, the final result is a direct measurement of the aerodynamic damplng for a known point on the performance map as a function of the interblade phase angle and reduced frequency.

2. The experimental and analytical tools needed to implement the proposed method have been developed. Specifically, they are:

a) The rotor must be subjected to a controlled excitation which causes measurable amplitude response of the blades. The excitation must be of a type which can be terminated within one period of the blade vibratory response. In the present investigation a controllable upstream gas injector was used, but in general any combination of structural or aerodynamic excitation can be employed.

b) During and after the excitation, the displacements of each blade must be measured. The blade modal displacements must then be identified by proper transformations and filtering. Either piezoelectric crystals or strain gauges will provide the data.

c) An adequate characterization of the structural dynamics of the blade-disk-shroud-shaft system must be developed and sufficient data must be collected during the test to determine the participation of the disk in the response. In this investigation, a structural model was developed which focuses on the inertial coupling of the blades through the rigid body mode of the disk, and three accelerometers were mounted on the disk to measure these in-plane displacements.

d) A capability must exist to process and reduce the data gathered in order to solve the equations of motion for the force acting on the blades. If the equations are expressed in terms of individual blade displacements the result is a calculation of the force acting on an individual blade. If a Discrete Fourier transform around the rotor is performed on the blade displacement data to extract the amplitude of the multiblade modes, the computed forces are the generalized forces acting on these global modes. Pairs of these multiblade modes have specific interblade phase angles.

3. In addition to the elastic deformation of the disk, the rigid body modes of the disk must be included in any model of the structural dynamics of the blade disk system. For research rotors with thick massive disks, these in-plane inertial effects dominate the blade disk coupling.

4. The aerodynamic damping of a transonic rotor operating at a known point has been measured for several values of the interblade phase angle. In all cases, the rotor was aeroelastically stable.

5. When operating in rotating stalls the passage of stall cells by a

blade excite the blade at the fundamental frequency of cell passage and its higher harmonics. For the rotor tested, the blade bending load decreases as it enters the stall cell and it relaxes back toward its rest position. As the cell passes the blade regains its steady load and maintains it until the arrival of the next cell.

6. In the forced vibration response to three upstream struts, it was observed that the addition of a two per revolution upstream disturbance diminished the three per revolution response. This could be due to a nonlinear mechanism either in the disturbance generation or the blade response. It suggests that it may be possible to reduce the forced vibration response of a rotor by "mistuning" the upstream disturbance.

7.2 Recommendations for Future Study

1. A useful demonstration of the techniques developed would be to perform a series of experiments on a rotor known to have an aeroelastic stability boundary close to or within its normal operating map. A series of runs could then be made where the rotor was successively run first near, then at, then over, its stability boundary. The aerodynamic damping of the mode known to become unstable could be followed from positive damping, through zero at the boundary, to a negative value in the unstable region. In this way, a great deal of insight could be gained into the nature of aerodynamic damping in general, and its role in aeroelastic instabilities in particular.

2. During the course of this investigation, a great deal of data was taken on the unsteady pressure field upstream and downstream of the rotor, both by fixed and rotating transducers. The signal from the rotating total

pressure probe showed a great deal of response in the range of several hundred to a thousand Hertz not readily associated with the blade natural frequencies or any multiple of the shaft frequency. Surprisingly, the fixed transducers also showed a great deal of response in this range, well below blade passage frequency, at about 3400 Hz. The frequencies and amplitudes as measured by the fixed transducers were similar but not identical to those measured by the rotating probe. It is thought that this "combination tone" noise, responsible for some of the acoustic emission of modern jet engines, could be related to the unsteady vibratory motion of the blades. The interaction of the aeroelastic and acoustic phenomena is important and of great interest, and should be further explored.

3. The techniques developed here for obtaining aerodynamic forcing data from blade motions should be applied to turbomachine experiments other than those conducted in the MIT Blowdown Compressor, so as to assess its general applicability.

REFERENCES

1. Adamczyk, J.J., "Analysis of Supersonic Stall Bending Flutter in Axial-Flow Compressors by Actuator Disk Theory", NASA Technical Paper 1345, 1978.

2. Dowell, E.H., Sisto, F., et al., A Modern Course in Aeroelasticity, Sijthoff and Noordhoff, Alphen aan den Rijn, The Netherlands, 1978.

3. Fleeter, S., "Aeroelastic Research for Turbomachine Applications", AIAA Paper 77-437, AIAA Dynamics Specialist Conference, San Diego, California (March 24-25, 1977).

4. Dugundji, J., "Flutter Analysis of a Tuned Rotor with Rigid and Flexible Disks", MIT GT&PDL Report No. 146, July 1979.

5. Whitehead, D.S., "Bending Flutter of Unstalled Cascade Blades at Finite Deflection", ARC Reports and Memoranda No. 3386, October 1962.

6. Whitehead, D.S., "Torsional Flutter of Unstalled Cascade Blades at Zero Deflection", ARC RePorts and Memoranda No. 3429, March 1964.

7. Smith, S.N., "Discrete Frequency Sound Generation in Axial Flow Turbomachines", ARC Reports and Memoranda No. 3709, March, 1972.

8. Verdon, J.M., and McCune, J.E., "Unsteady Supersonic Cascade in Subsonic Axial Flow", AIAA Journal, Vol. 13, No. 2, February 1975.

9. Whitehead, D.S., Grant, R.J., "Force and Moment Coefficients for High Deflection Cascades", University of Cambridge, CUED/A-Turbo/TR 98, May, 1980.

10. Snyder, L.E., and Commerford, G.L., "Supersonic Unstalled Flutter in Fan Rotors; Analytic and Experimental Results", J. Engineering for Power, Vol. 96, No. 4, October 1974, pp. 379-386.

11. Goldstein, M.E., Braun, W., and Adamczyk, J.J., "Unsteady Flow in supersonic Cascades with Strong In-Passage Shocks", J. Fluid Mechanics, Vol. 83, Pt. 3, 1977, pp. 569-604.

12. Ginzburg, S.I., "Calculation of the Boundary of Excitation of Flexural Flutter of a Homogeneous Array in a Quasistationary Approximation", translated from Problemy Prochnosti No. 8, 46-51, Pleum Press, August 1974.

13. Fleeter, S., et al., "An Experimental Determination of Unsteady Aerodynamics in a Controlled Oscllllatlng Cascade", J. Engineering for Power, Vol. 99, No. 1, January 1977 p.. 88-96.

14. Fleeter, S., et al., "The Unsteady Aerodynamics of a Cascade in Translation", AGARD Symposium on Stress, Vibrations, Structural Integration and Engine Integrity (Including Aeroelasticity and Flutter), AGARD CP 248, April 1979.

15. Jones, W., H., et al., "Experimental Apparatus for investigation of Fan Aeroelastic Instabilities in Turbomachinery", NASA TM-X-3508, June 1977.

16. Lubomski, J.F., "Characteristics of Aeroelastic Instability in Turbomachinery - NASA Full Scale Engine Test Results", NASA TM-X-79085, April 1979.

17. Kerrebrock, J.L., "Flow in Transonic Compressors", 1980 Dryden Lecture, Paper AIAA-80-0124, January 1980.

18. Mikolajczak, A.A., Arnoldi, R.A., Snyder, L.E., and Stargardter, H., "Advances in Fan and Compressor Blade Flutter Analysis and Predictions", J. Aircraft, Vol. 12, No. 4, pp. 325-332, April 1975.

19. Durali, M., "Rotor Wake Behavior in a Transonic Compressor Stage and its effect on the Loading and Performance of the Stator", MIT GT&PDL Report No. 149, April 1980.

20. Kerrebrock, J.L., et al., "The MIT Blowdown Compressor Facility", J. Engineering for Power, Vol. 96, No. 4, pp. 394-405, October 1974.

21. Ng, W.F., "Detailed Time Resolved Measurements and Analysis of Unsteady Flow in a Transonic Compressor", M.S. Thesis, Department of Mechanical Engineering, MIT, August 1980.

22. Kerrebrock, J.L., Epstein, A.H., and Thompkins, W.T., "A Mixture Miniature High Frequency Sphere Probe", Measurement Methods in Rotating Components in Turbomachinery, 79-57425, ASME 1980.

23. Overall, B.W., "Evaluation of an Airet Distortion Generator Used to Produce Steady State Total Pressure Distortion at the Inlet of Turbine Engines", Arnold Engineering Development Center Report AEDCTR-97-141, December 1976.

24. Fabunmi, J.A., "Forced Vibration of a Single Stage Axial Compressor Rotor", J. Engineering for Power, Vol. 102, No. 2, April 1980, pp. 322-328.

25. Hohenenser, K.K., and Yin, S-K., "Some Applications of the Method of Multiblade Coordinates", J. of American Helicopter Society, Vol. 17, July 1972, pp. 3-12.

26. Ewins, O.J., "Vibration Characteristics of Bladed Disk Assemblies" J. of Mechanical Engineering Science, Vol. 15, No. 3, 1973, pp. 165-186.

27. Carta, F.O., "Coupled Blade-Disk-Shroud Flutter Instabilities in Turbojet Engine Rotors", J. Engineering for Power' Vol. 89, July 1967, pp. 419-426.

28. Ewins, D.J., "Vibration Modes of Mistuned Bladed Disks", ASME Paper No. 75-GT-14, April 1975.

29. Crandall, S.H. and Dugundji, J., "Forced Backward Whirling of Aircraft Propeller-Engine Systems", Proceedings of the Second International Conference on Vibrations in Rotating Machinery, The Institution of Mechanical Engineering, Churchill College, Cambridge, England, September 1980.

30. Kaiser, J.F. and Reed, .A., "Data Smoothing Using Low-Pass Digital Filters", Rev. Sci. Instrumentation, Vol. 48, No. 11, November 1977.

31. Bartlett, F.G., Greitzer, E.M., "Stalled Flow Performance of a Single Stage Transonic Compressor", MIT Gas Turbine and Plasma Dynamics Laboratory Report 144, December 1978.

32. Day, I.G. and Cumpsty, N.A., "Measurements and Interpretation of Flow Within Rotating Stall Cells in Axial Compressors", J. of Mechanical Engineering Science' Vol. 20, No. 2, 1978.

Appendix - Mass Properties of the M.I.T. Rotor

Overall and blade mass properties for all blades unweighted and for J blades unweighted. (See equation 4.4 for definition)

	all blades unweighted	J blades unweighted
M_d (slug)	.793	---
M_b (slug)	.0058	---
M_w (slug)	---	.00776
M_T (slug)	.926	.926 + (N-J) .00776
I_T (slug ft^2)	.211	.211 + (N-J) .00601
m_0 (slug ft^2)	.00105	.00472
m_1 (slug ft^2)	.00169	.00639
m_2 (slug ft)	.00216	.00750

Blade dimensions and first bending mode shape:

	r_h	r_t-5	r_t-4	r_t-3	r_t-2	r_t-1	r_t
r (in)	5.43	6.56	7.56	8.56	9.56	10.56	11.56
Chord (in)	2.63	2.73	2.70	2.89	3.05	3.14	3.17
thickness(in)	.321	.321	.260	.213	.117	.110	.0827
area (in^2)	.844	.745	.491	.431	.378	.242	.184
γ (mode shape)	0.00	.0693	.168	.311	.489	.714	1.00

Table 2.1 - Instrumentation used in Aeroelastic Testing in the Blowdown Facility

Transducer	Location	4-Pole Filter 03db Freq. (KHZ)	Analogue to Digital Converter Channel
On Rotor Instrumentation:			
Rotor Total Pressure	Blade 8 r/r_T = .73	50	MIT[1] HS 5
PZT Displacement	Blade 18	--	MIT LS 9
PZT Displacement	Blade 1	--	CAMAC[2] LS 1
⋮	⋮		⋮
PZT Displacement	Blade 23 (360° on disk)	--	CAMAC LS 23
Strain Gauge	Blade 4	--	CAMAC LS 24
Strain Gauge	Blade 5	--	CAMAC LS 25
Disk Accelerometer	120° on disk	0.6	CAMAC LS 26
Disk Accelerometer	240° on disk r/r_T = .26	0.6	CAMAC LS 27
Disk Accelerometer	360° on disk	0.6	CAMAC LS 28
115 per Rev Tach	Rotor Shaft	--	MIT HS 6
1 per Rev Tach	Motor Shaft	--	CAMAC HS B1
Tunnel Instrumentation:			
5 way Probe P1		--	MIT HS 1
5 way Probe P2	Rotor TE	--	MIT HS 2
5 way Probe P3	@ r/r_T = .93	--	MIT HS 3
5 way Probe P4		--	MIT HS 4
Total Pressure (Kulite)	Supply Tank	1.4	MIT LS 2
Total Pressure (Statham)	Supply Tank	1.4	MIT LS 3
Total Pressure (Statham)	Dump Tank	1.4	MIT LS 5
Wall Static Press. (low f)	Rotor TE	1.4	MIT LS 6
Probe Linear Position	Probe Traverser	--	MIT LS 7
Probe Temp. Signal	Rotor TE	1.4	MIT LS 8
Wall Static Pressure (high f)	1 chord upstream of 2E	--	CAMAC HS A1
Wall Static Pressure (high f)	1 (.1) chord upstream of LE[3]	--	CAMAC HS A2

Notes: 1. MIT A/D samples at 100 KHZ. (HS) and 10 KHZ.(LS) during "test time"
2. CAMAC A/D samples at 100 KHZ. (HS) and 5 KHZ.(LS) during "test time"
3. When injector was used,transducer was moved to 0.1 chord upstream.

TABLE 2.2

TIME LINE OF EVENTS IN BLOWDOWN
DURING AEROELASTIC TESTING

Time after Rupture of Diaphram (msec.)	Event
0	Diaphram Bursts, Expanding Gas Hits Rotor
5	Probe Traverse Begins
10	
15	
20	
25	
30	
35	
40	Probe Reaches r/r_T = .93
45	
50	Beginning of Quasi-Steady "Test Time"
55	Injector Flow Begins (if used)
60	
65	
70	
75	
80	
85	
90	
95	
100	Injector Shuts Off (if used)
105	
110	
115	
120	Boundary Layer Bleed Unchokes
125	
130	
135	
140	
145	Downstream Throttle Unchokes, End Of "Test Time"
150	Calibration Continues For 30 Seconds

Table 5.1 Measured Values of Damping

Blade Node	Nodal Diameters (n)	Interblade Phase Angle (β)	Frequency (Hz)	Tip Reduced Frequency ($\omega c/2V$)	Time Constant (msec.)	Log Decrement (δ)
1 Bend	1	- 15.6	290	.25	4.8	.72
1 Bend	2	- 31.3	290	.25	5.1	.68
2 Bend	3	- 47.0	435	.38	3.0	.77
2 Bend	8	-125.0	1160	1.01	6.1	.14

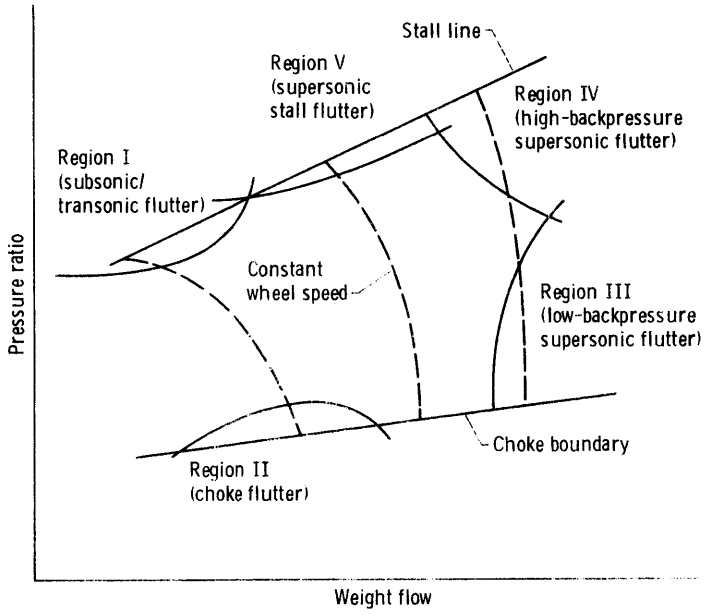

Figure 1-1 Compressor performance and stability map.

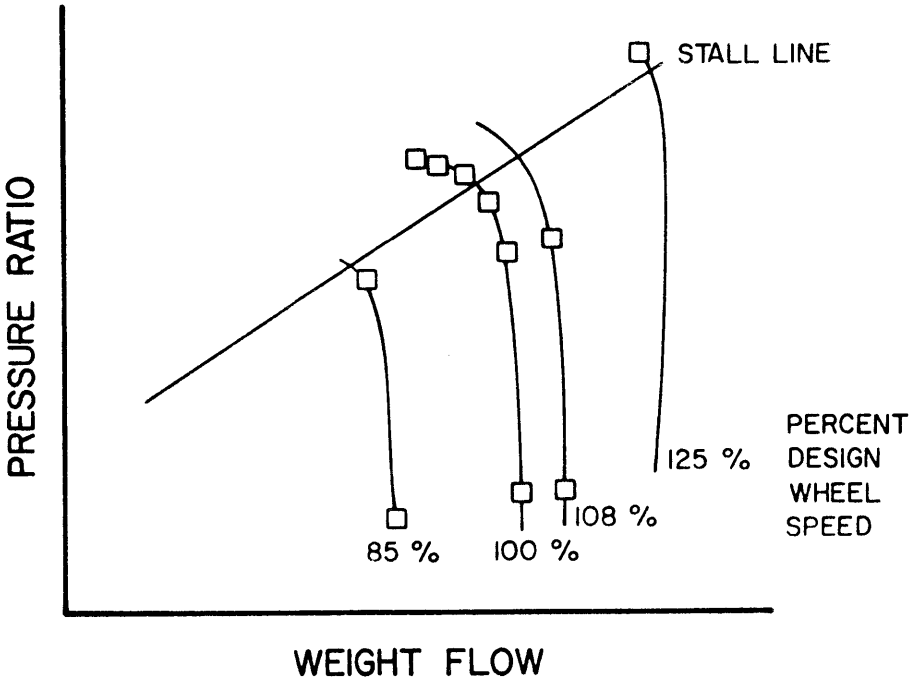

Figure 1-2 Relative location on performance map of tests performed in search of flutter boundaries.

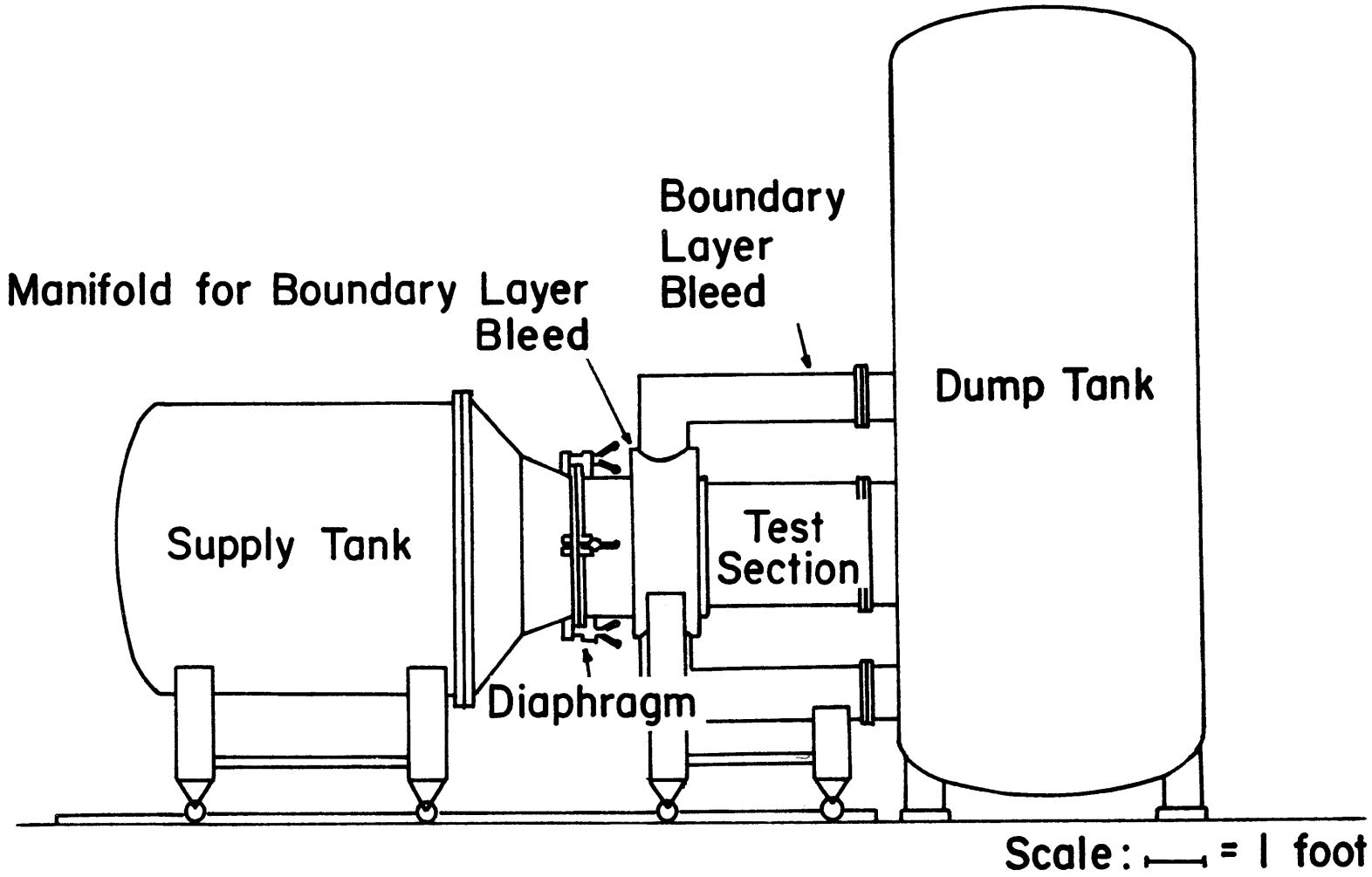

Figure 2-1 Scale drawing of Blowdown Compressor Facility

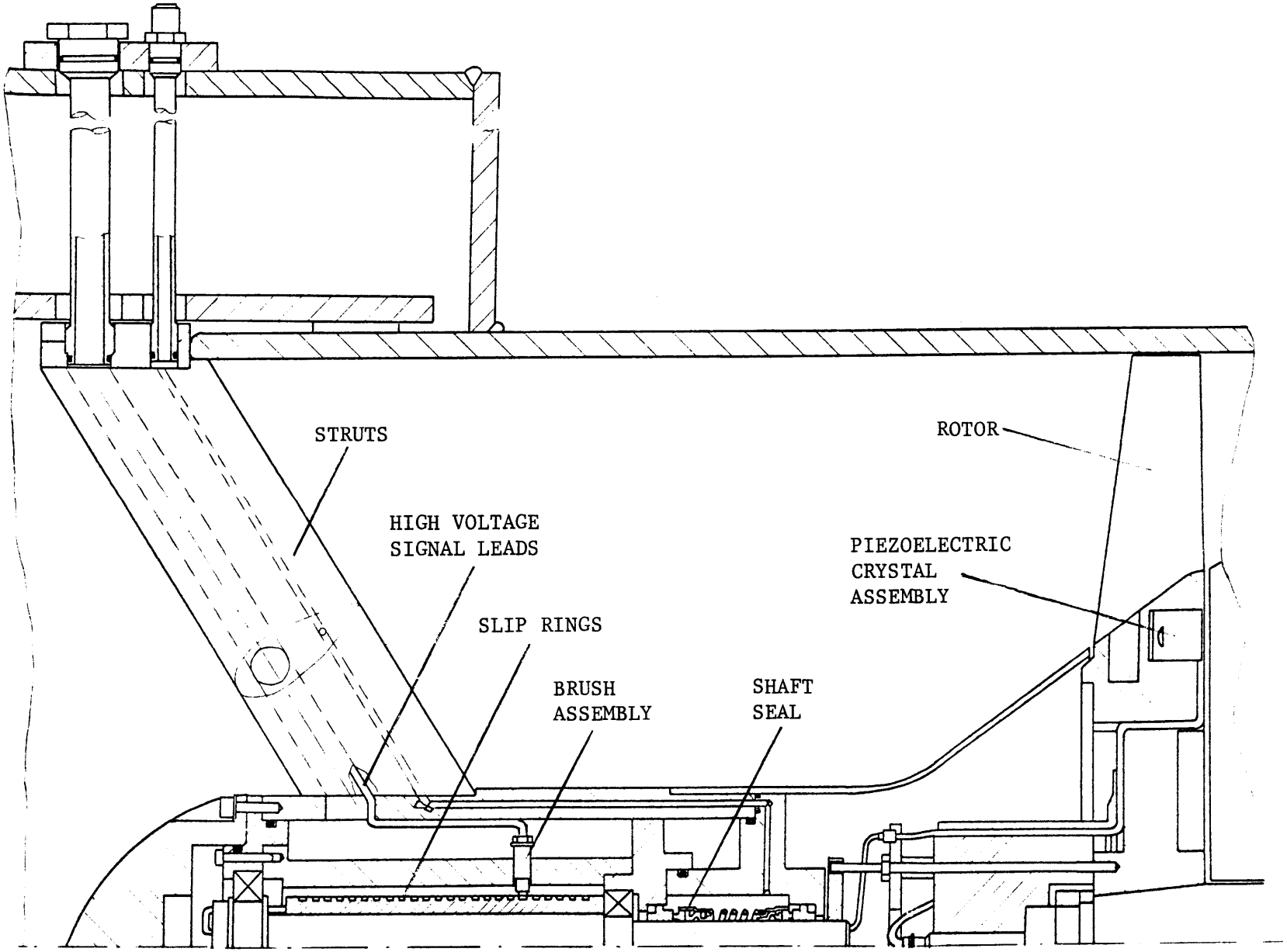

Figure 2-2 Cut away view of the rotor, shaft and forward centerbody

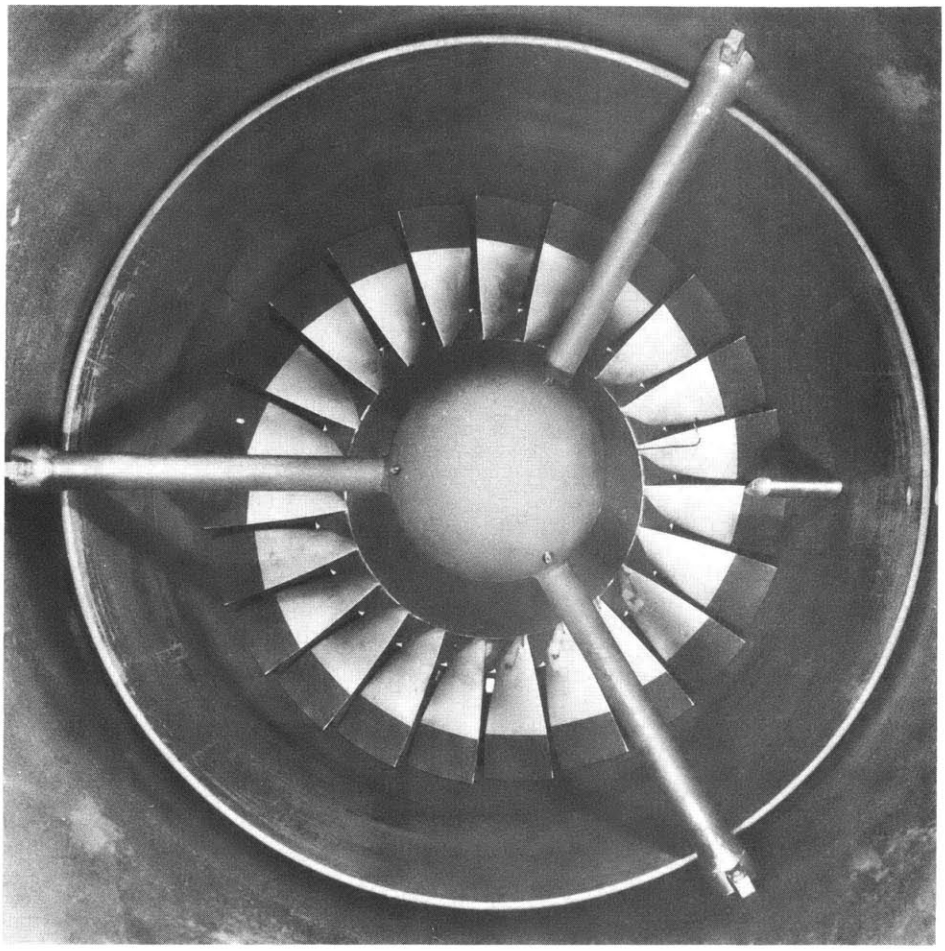

Figure 2-3 View looking downstream into the Blowdown Facility showing the forward centerbody, boundary layer bleed, gas injector (only visible on right), and instrumented rotor.

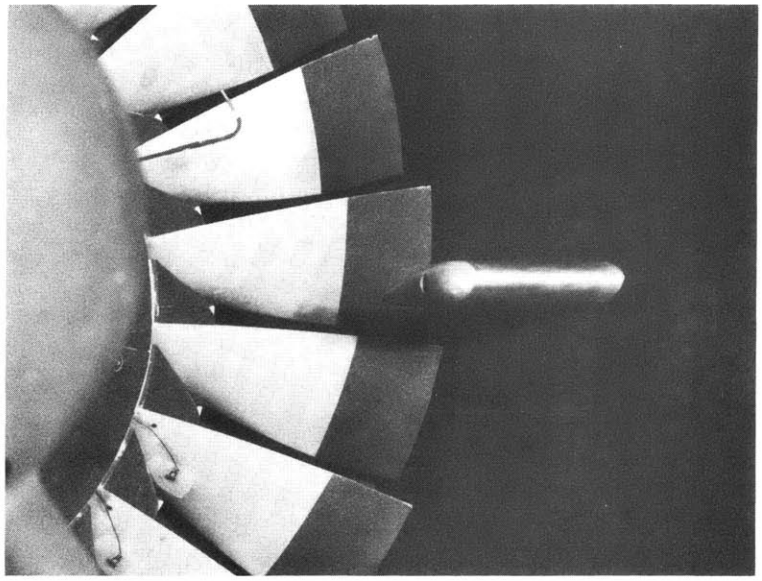

Figure 2-4 Closeup view of the faired gas injector. Also visible are the blades on which the total pressure probe and strain guages are mounted.

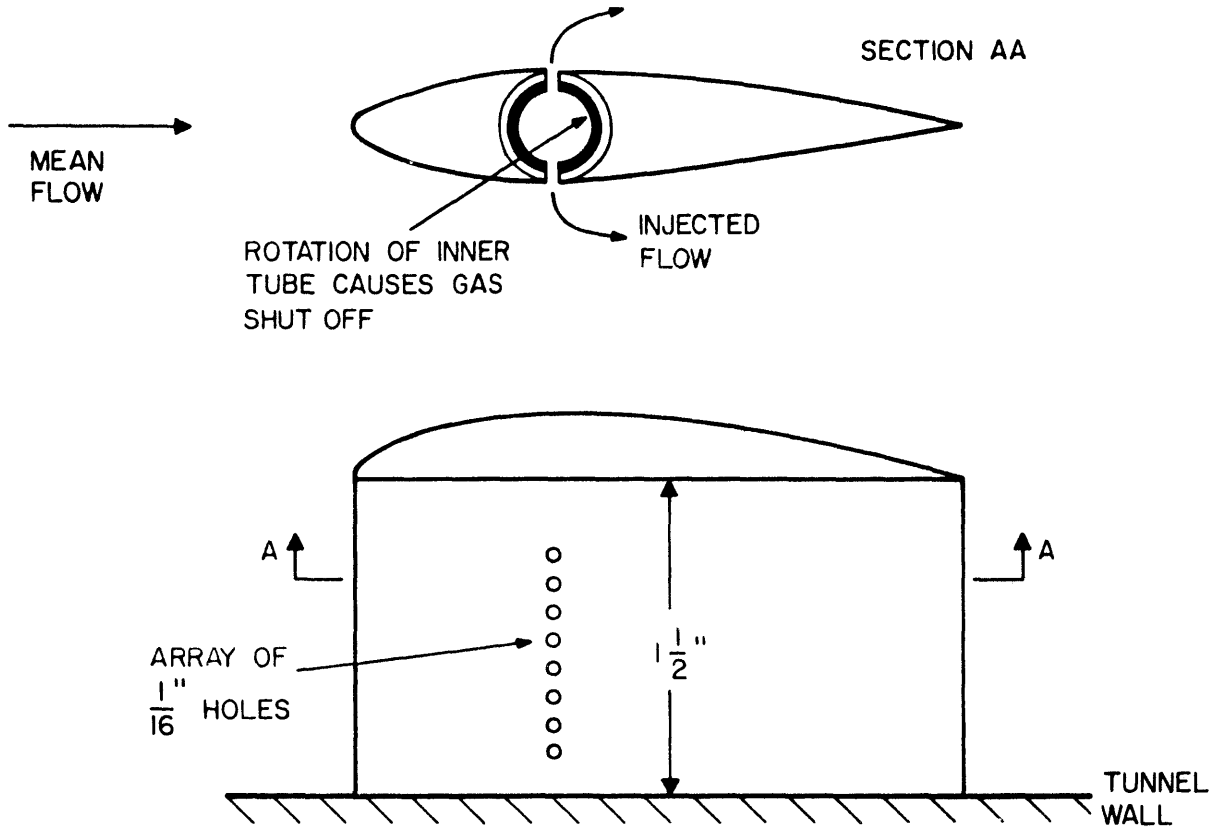

Figure 2-5 Diagram of gas injector showing hole pattern and gas flow path.

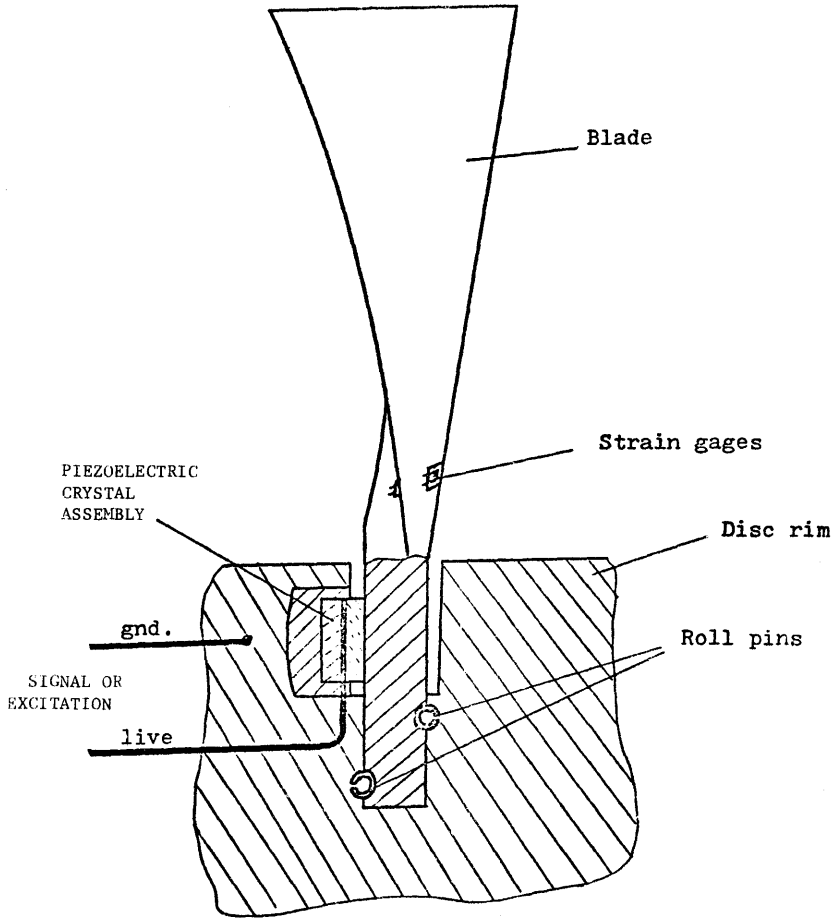

Figure 2-6 Details of root attachment showing the location of the piezoelectric displacement transducer.

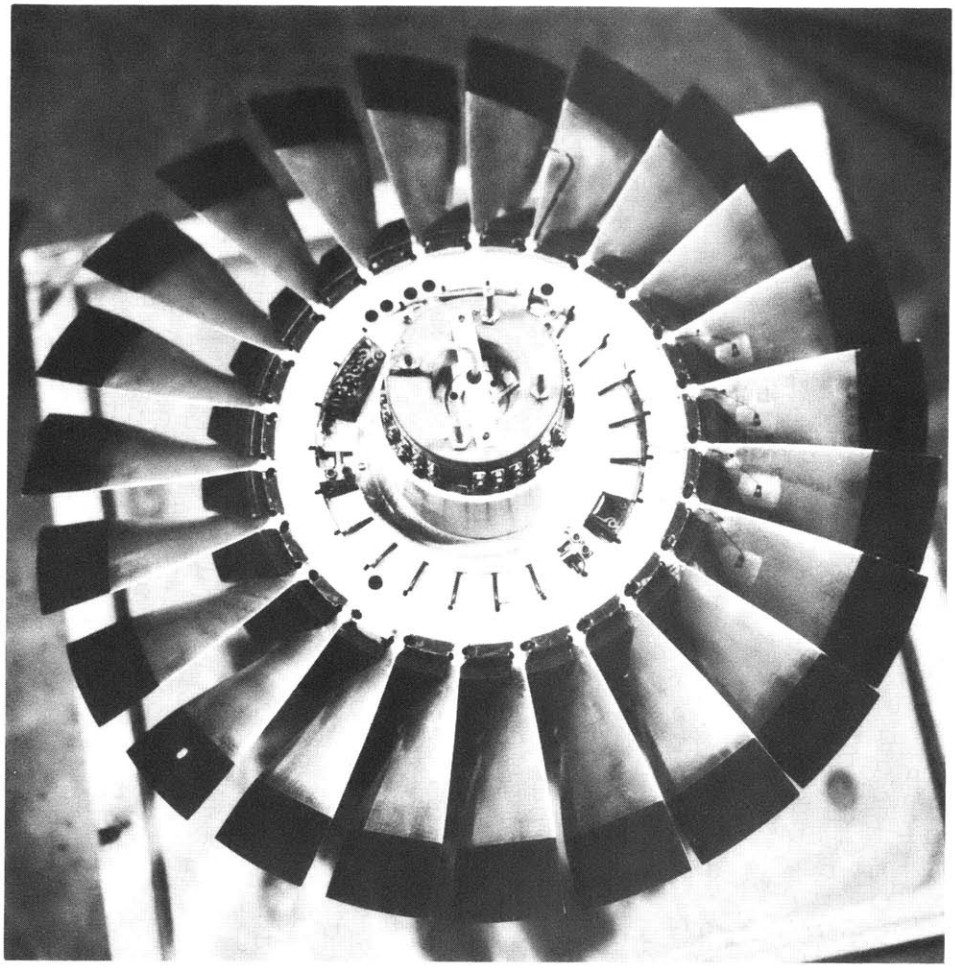

Figure 2-7a Instrumented M.I.T. Rotor with disk exposed showing instrumentation and wiring.

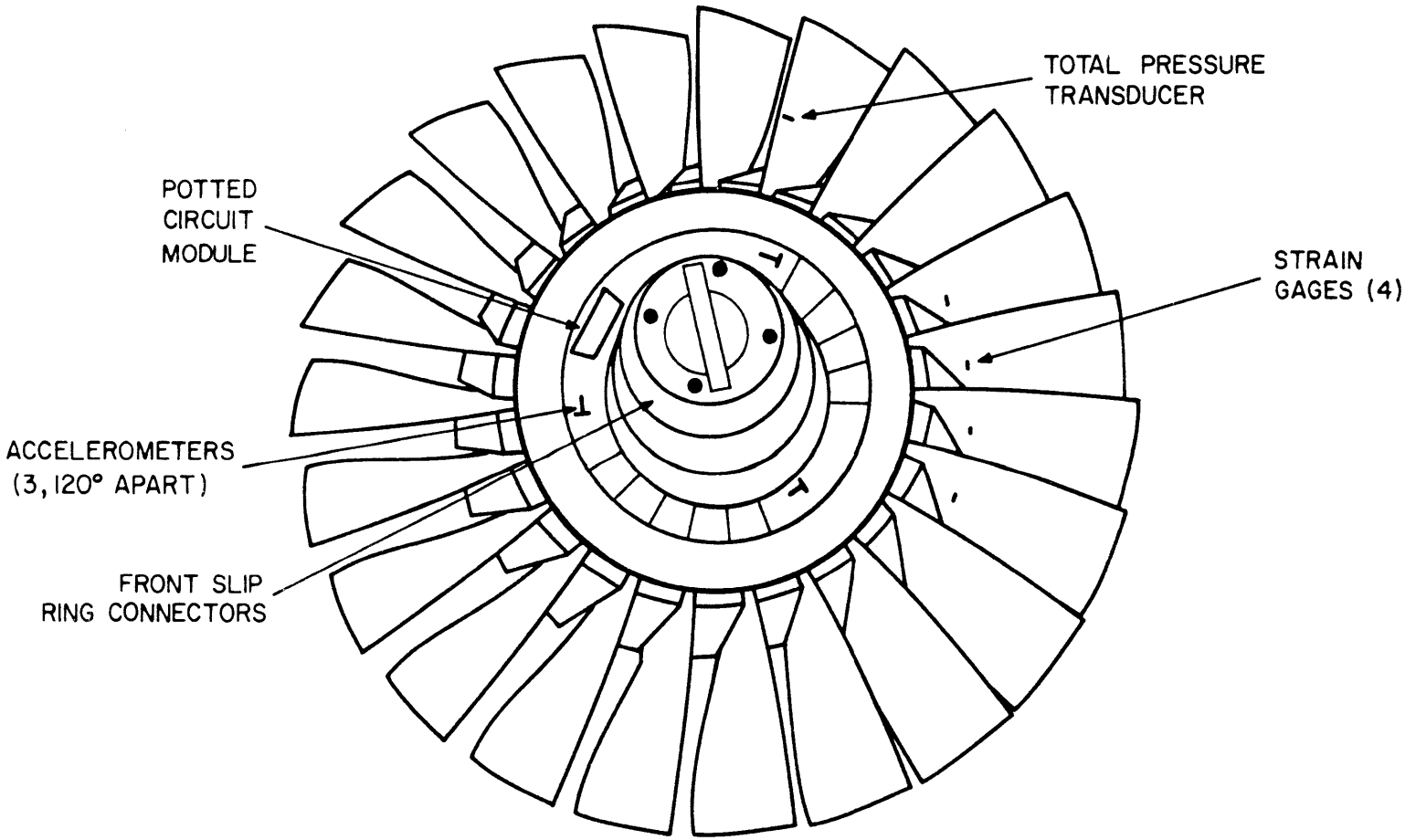

Figure 2-7b Location of instrumentation on disk and blades.

(Compare with Figure 2-7a)

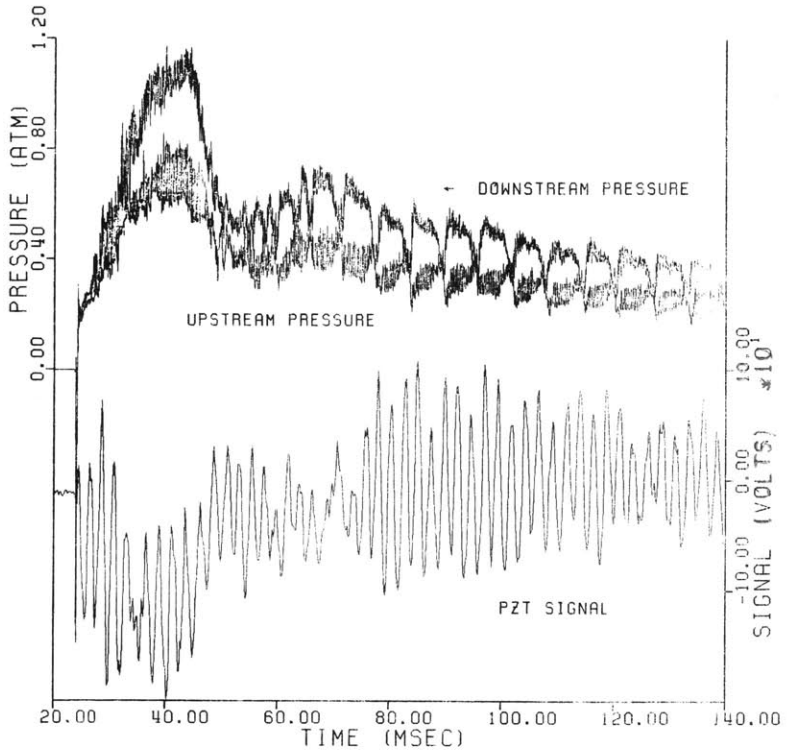

Figure 2-8 Time history of the wall static pressure measured upstream and downstream of the rotor, and the response of one blade piezoelectric crystal (PZT). In this test the diaphram burst at about 23 msec.

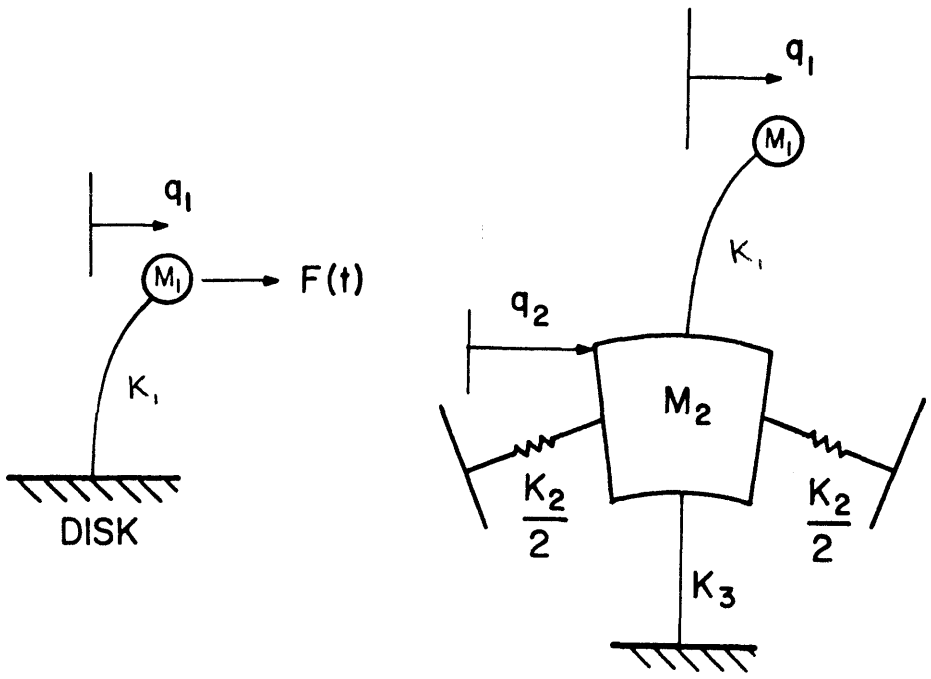

Figure 3-1 Left: Model of an isolated blade mounted on a rigid disk.
Right: Model of a blade mounted on a segment of a disk with finite mass and stiffness.

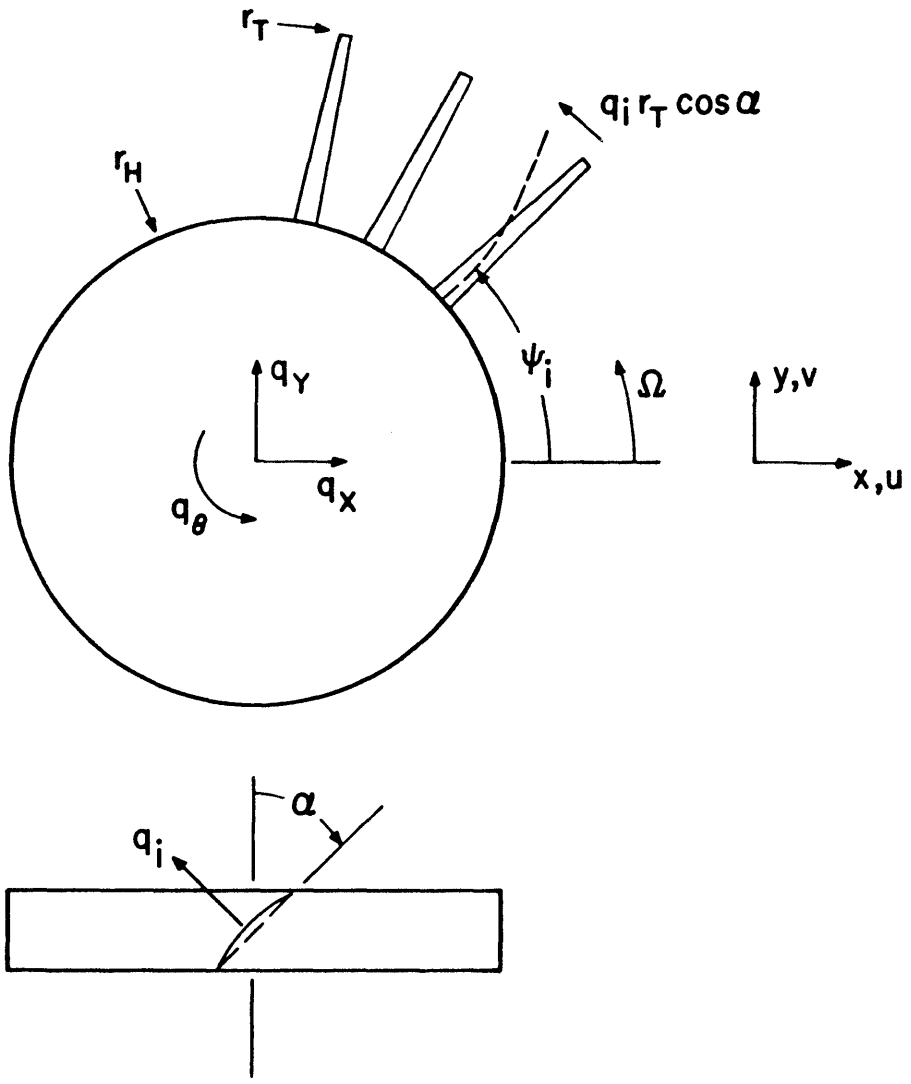

Figure 3-2 Structural model of the M.I.T. Rotor with flexible blades attached to a rigid disk, which possesses 3 in plane degrees of freedom.

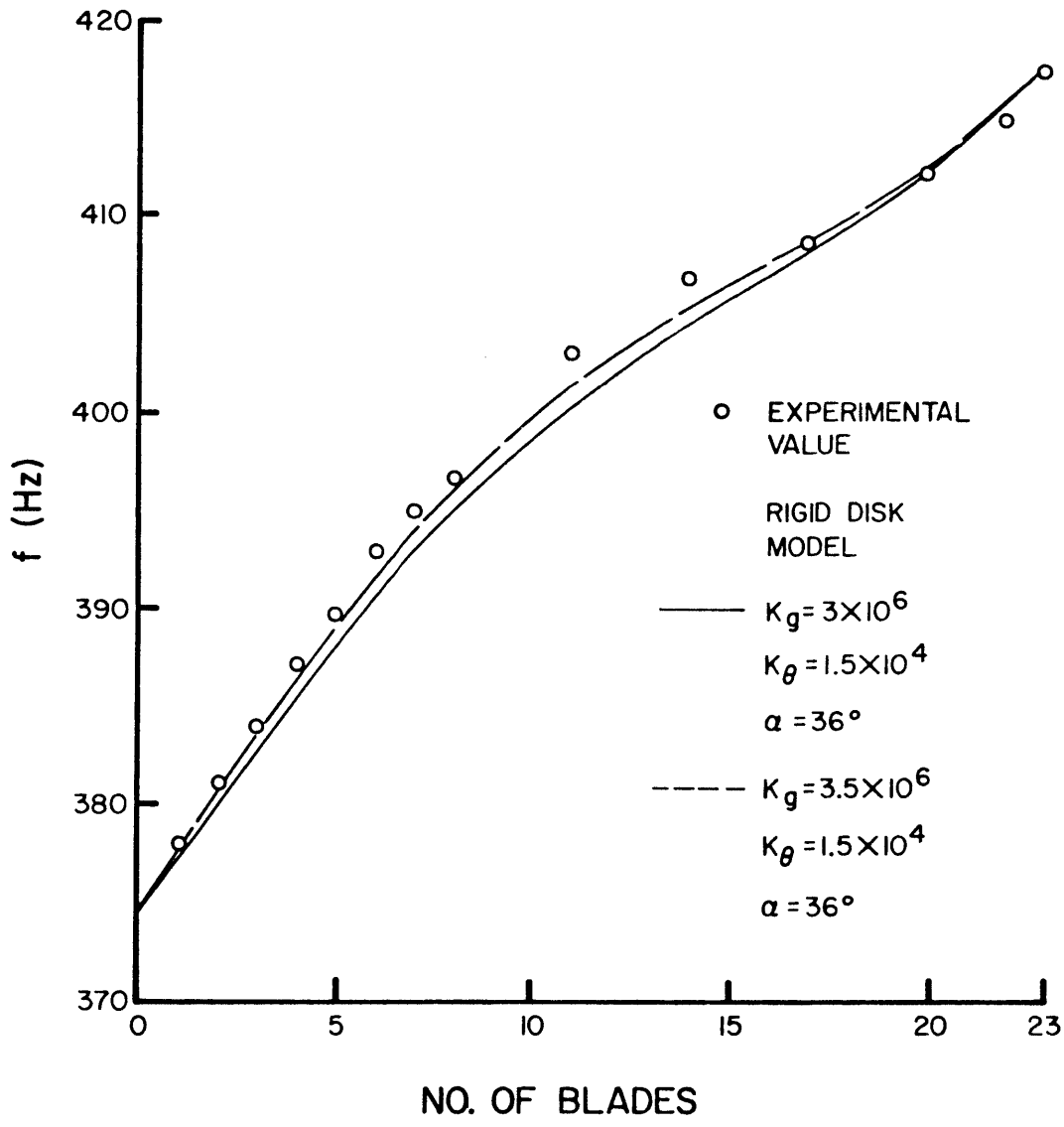

Figure 3-3 Frequency of the highest observed (in phase) mode vs. the number of blades participating.

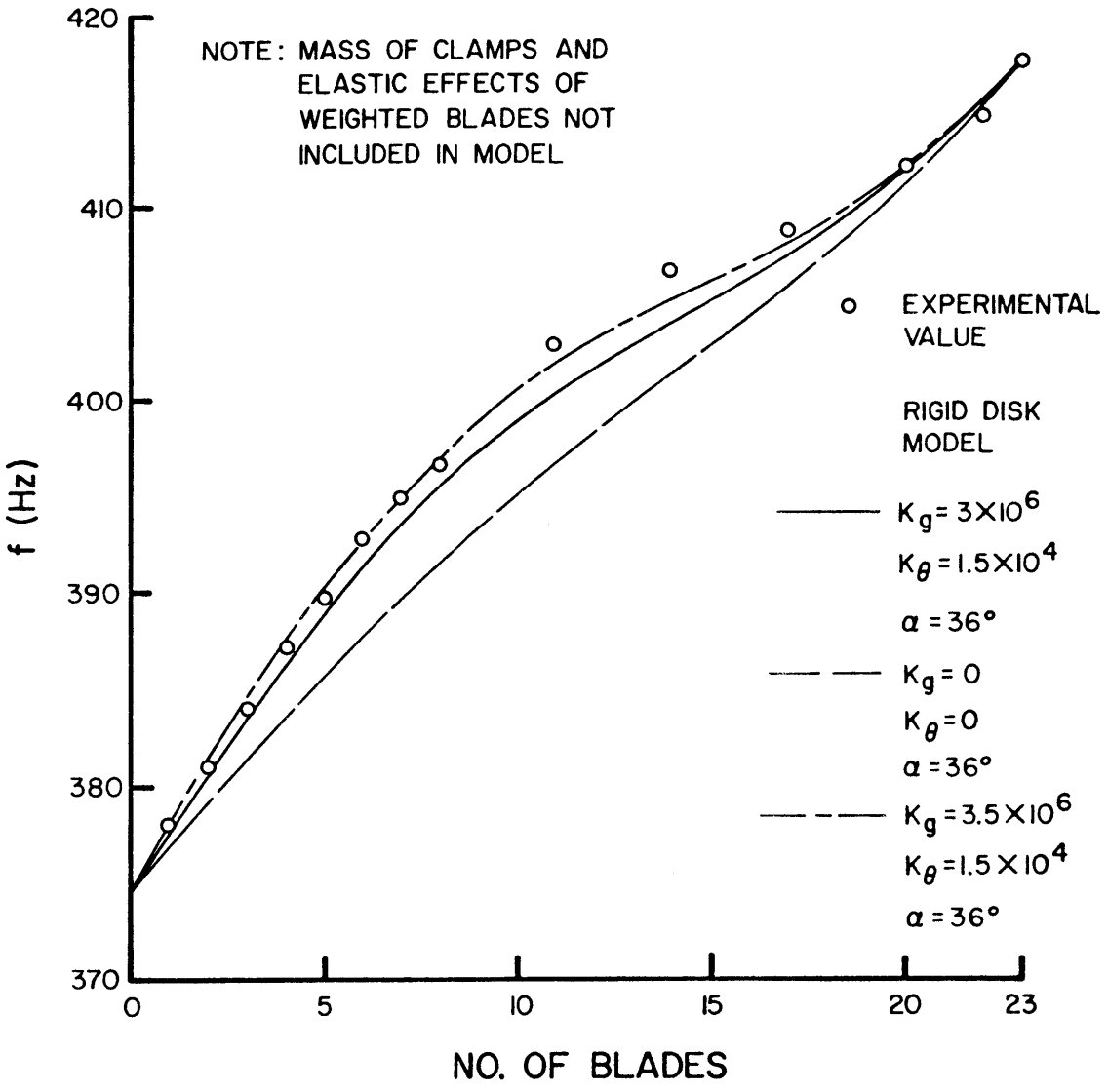

Figure 3-4 Frequency of the highest observed (in phase) mode vs. the number of blades participating.

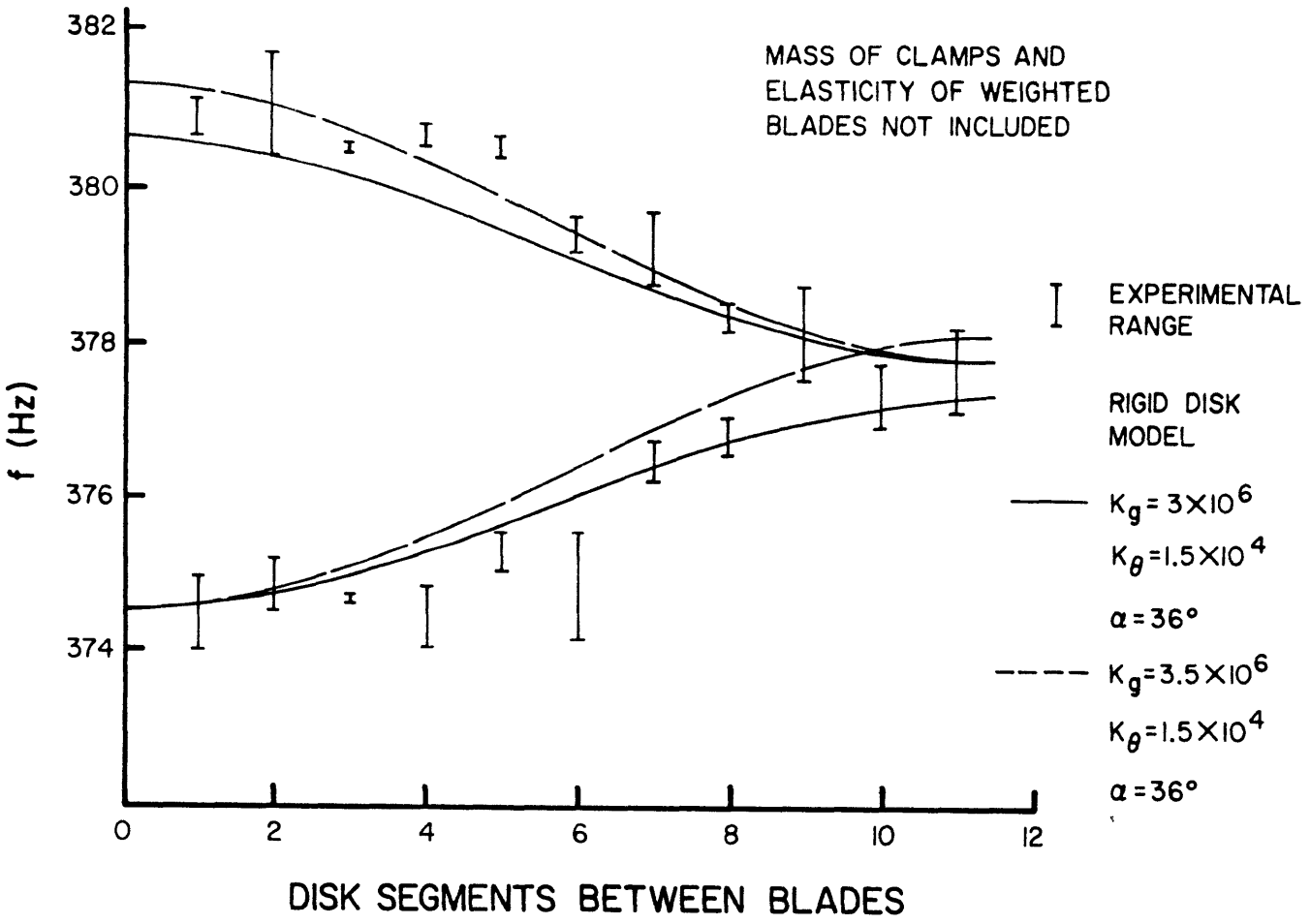

Figure 3-5 The two observed frequencies of a system with 2 blades free to participate vs. the angular separation between blades. (For a 23 bladed rotor, 11.5 corresponds to 180 degrees).

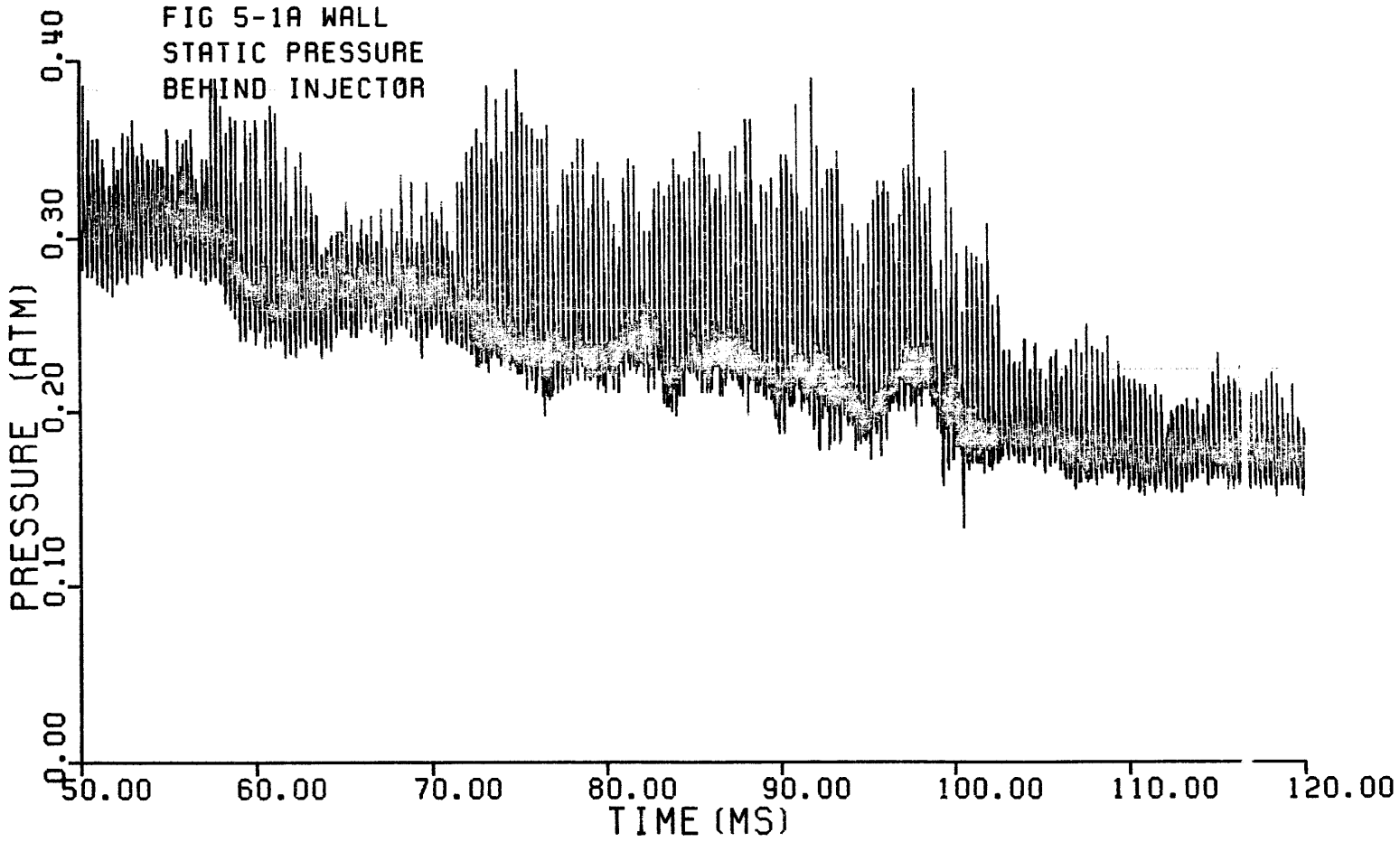

Figure 5-1a Upstream wall static pressure measured one inch behind the injector.

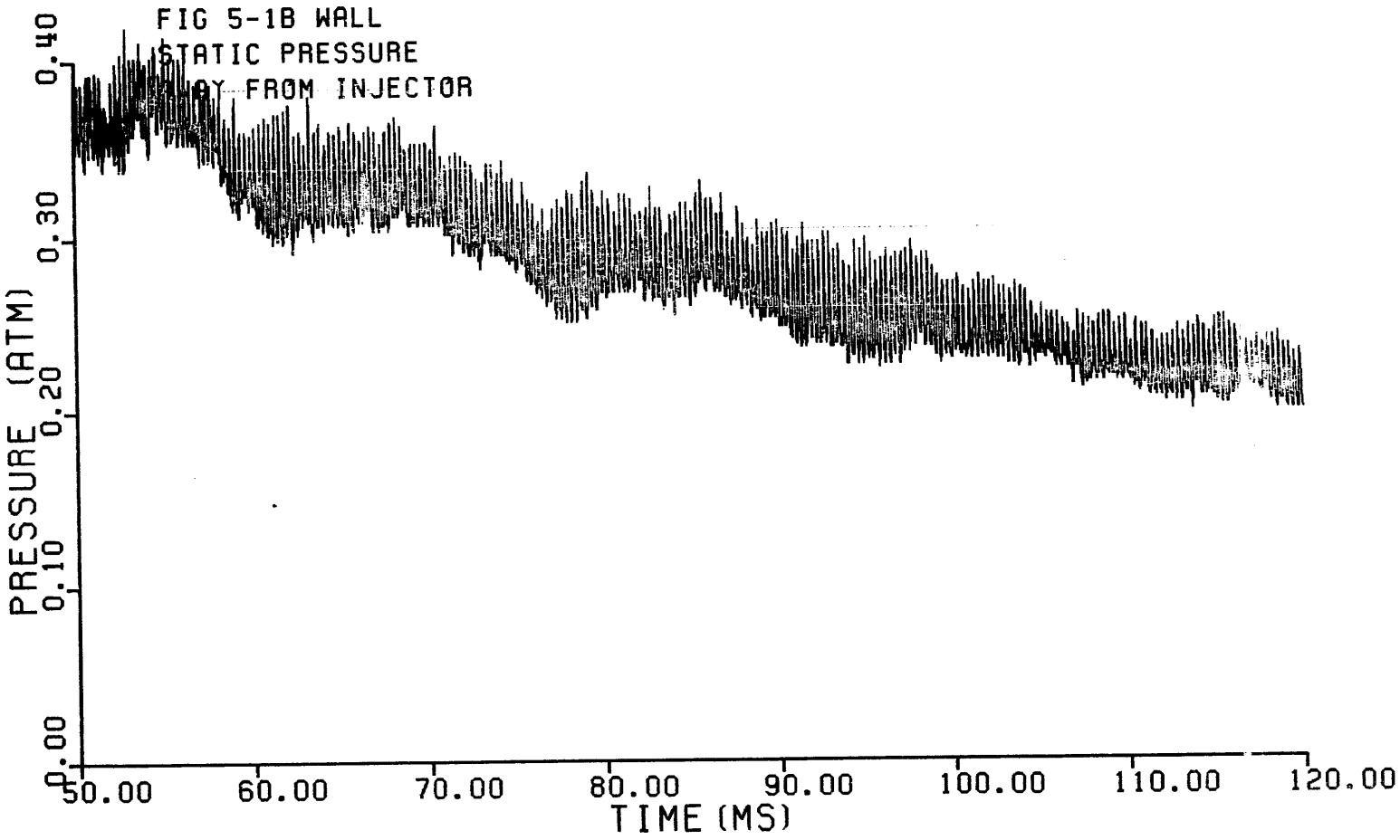

Figure 5-1b Upstream wall static pressure measured 72 degrees away from an injector.

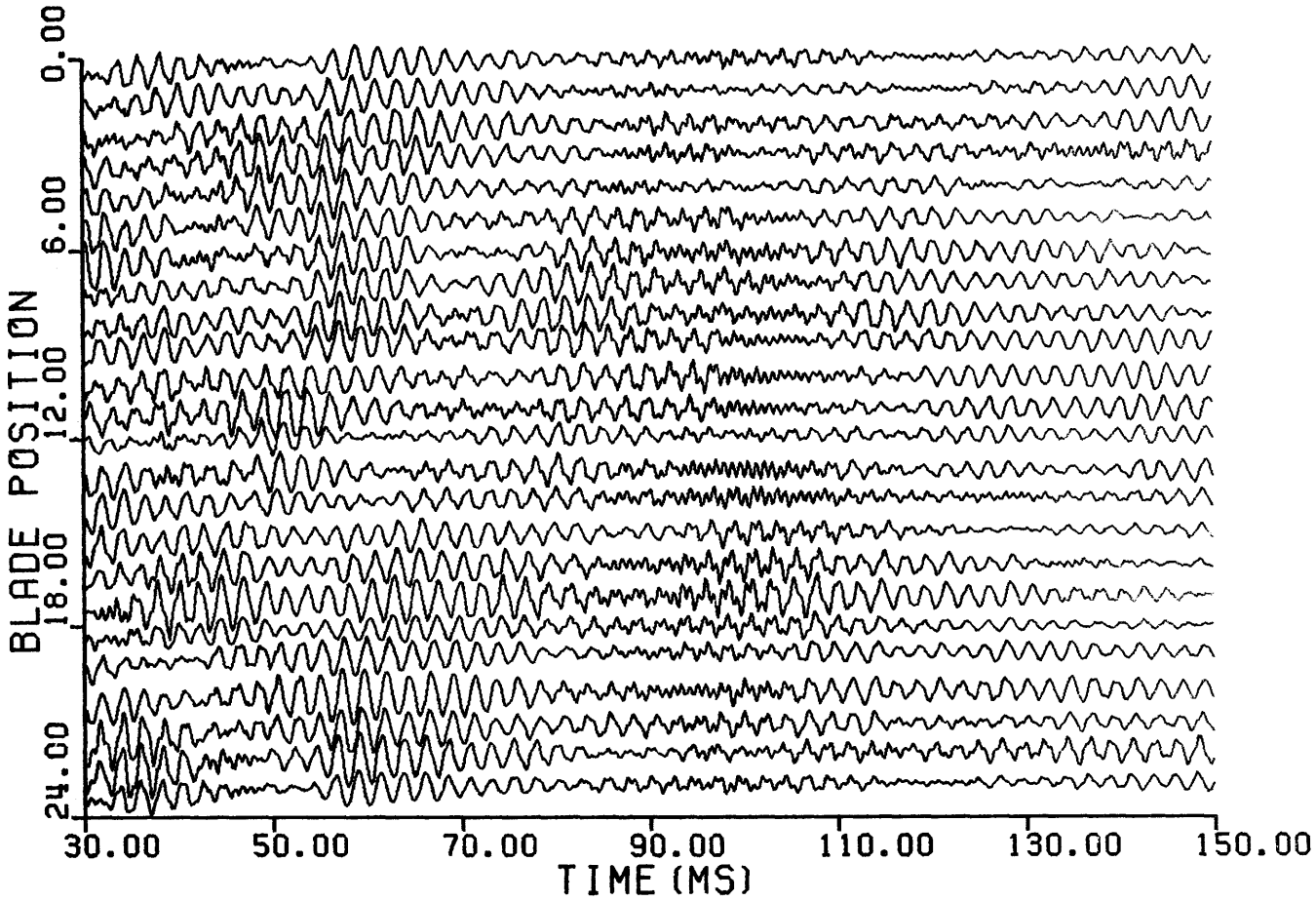

Figure 5-2 Total response of the piezoelectric crystal for all blades. Each is shown in its proper relative location. Blade 23 is shown again as zero for reference.

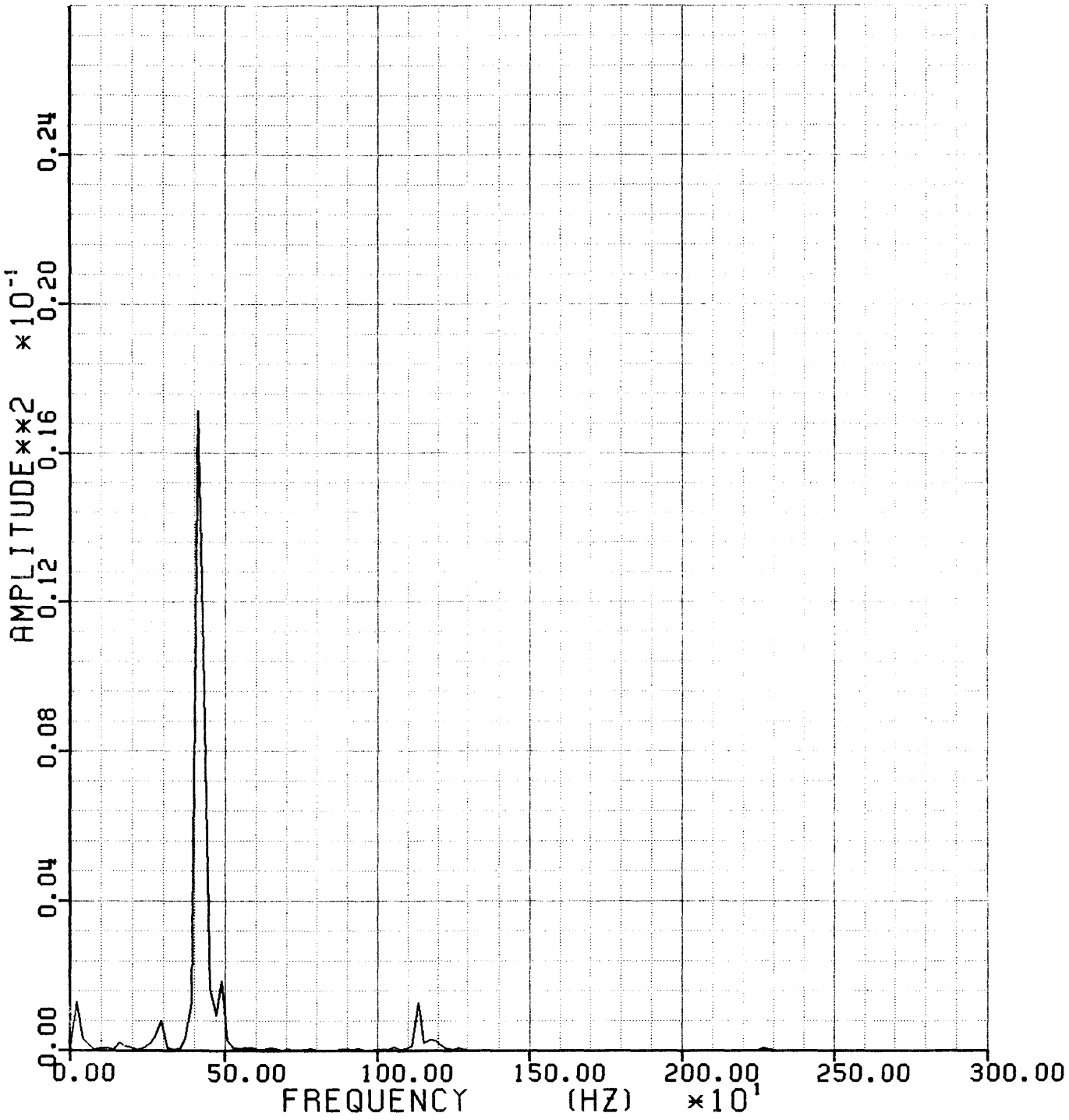

Figure 5-3 Power spectrum density of Blade 3 response for the period from 50 to 100 msec.

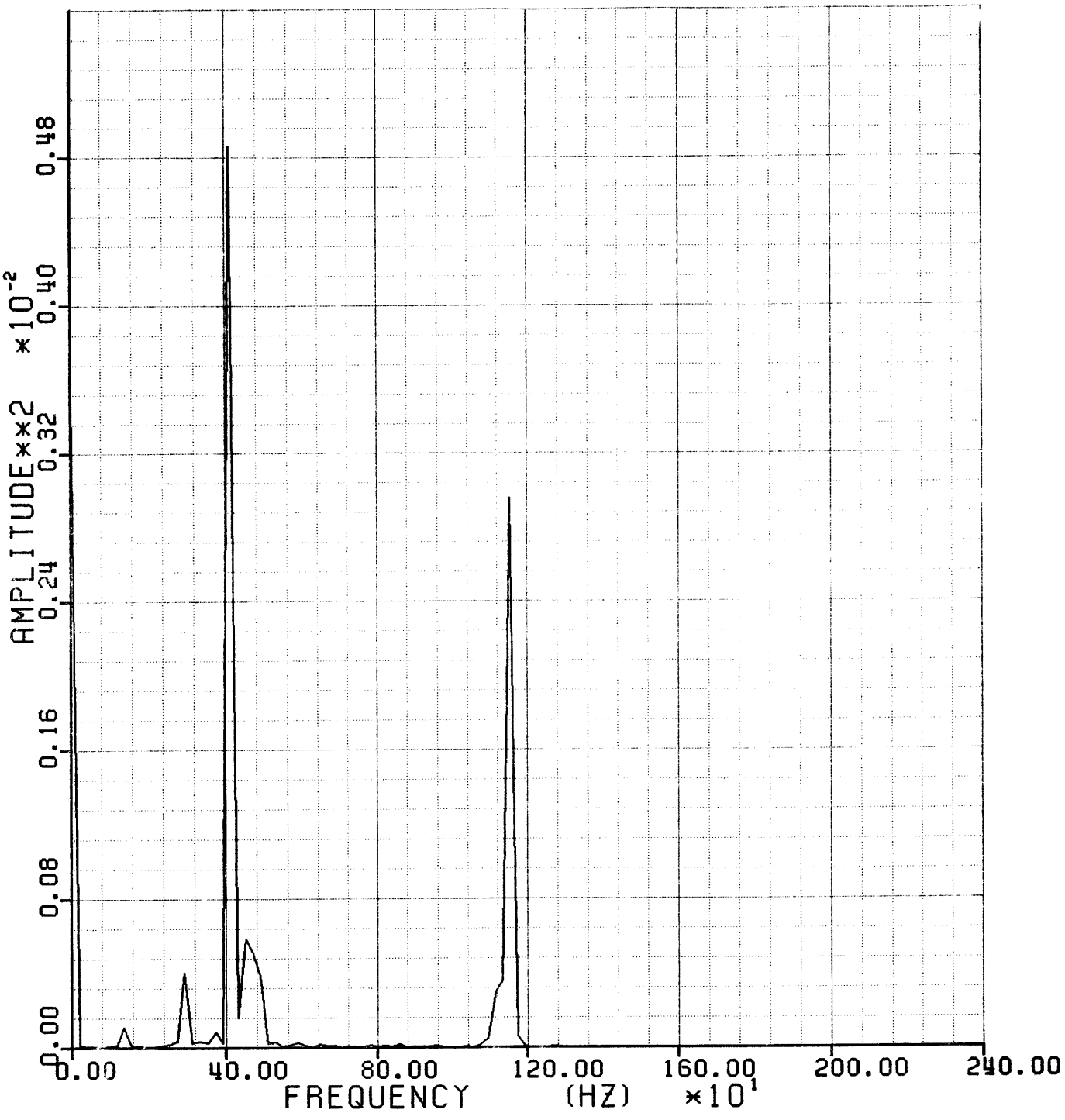

Figure 5-4 Power spectrum density of Blade 3 response for the period from 100 to 150 msec.

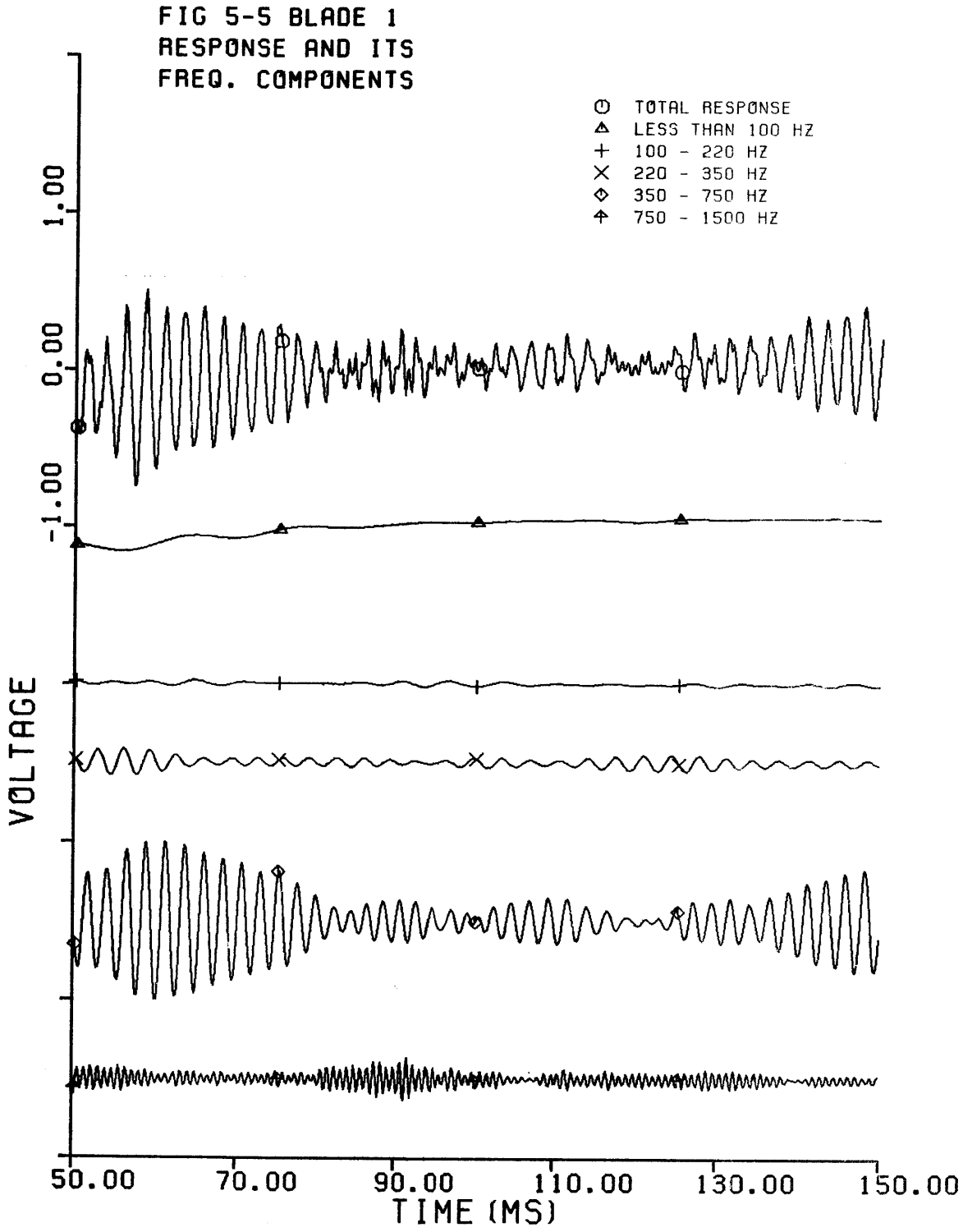
FIG 5-5 BLADE 1
RESPONSE AND ITS
FREQ. COMPONENTS
TOTAL RESPONSE
LESS THAN 100 HZ
100 - 220 HZ
220 - 350 HZ
350 - 750 HZ
750 - 1500 HZ
1.00
0.00
-1.00
VOLTAGE
50.00
70.00
90.00
110.00
130.00
150.00
TIME (MS)

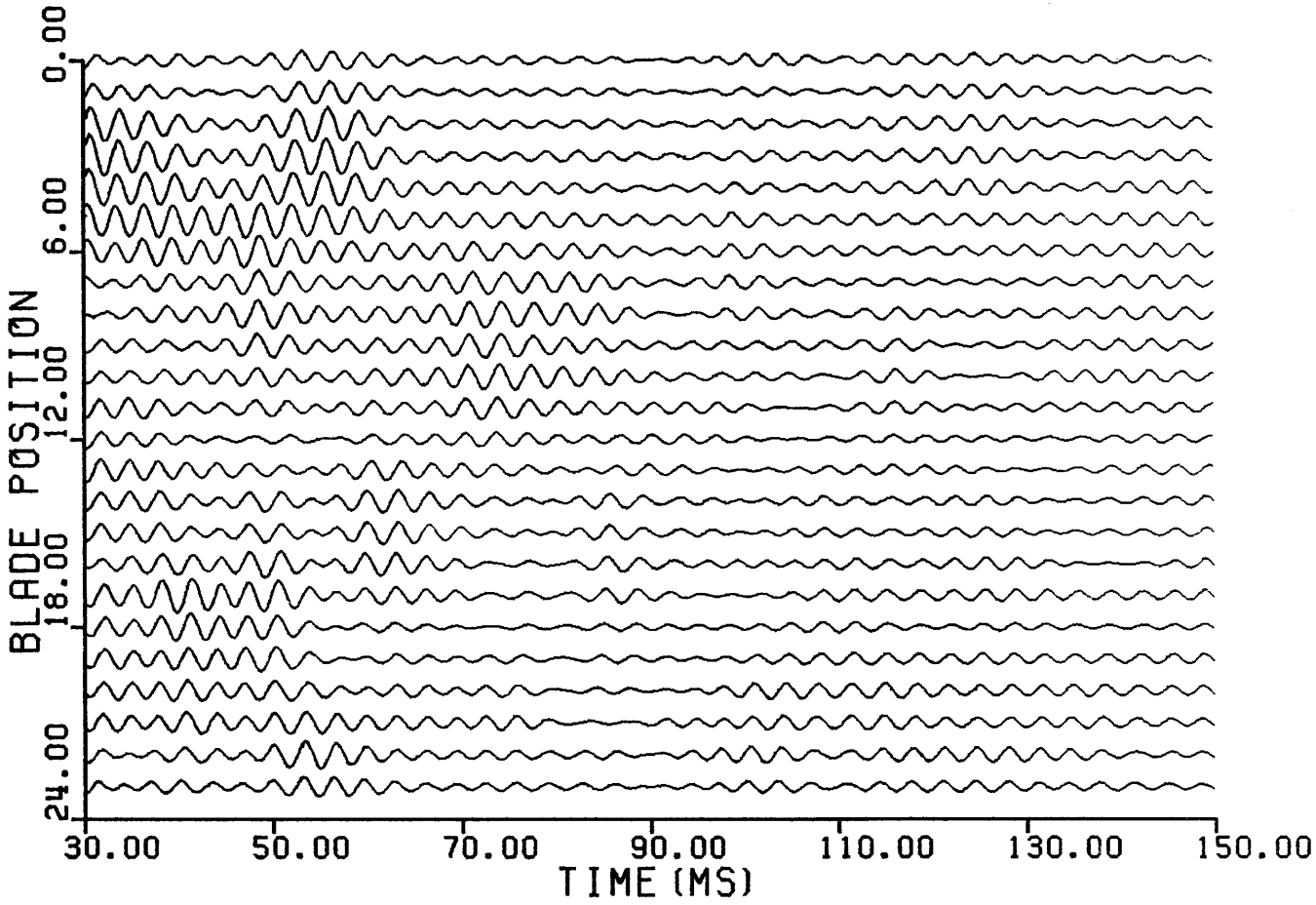

Figure 5-6 Blade response in the range of 220-350 Hz.
(shown at 4 times the scale of Figure 5-2)

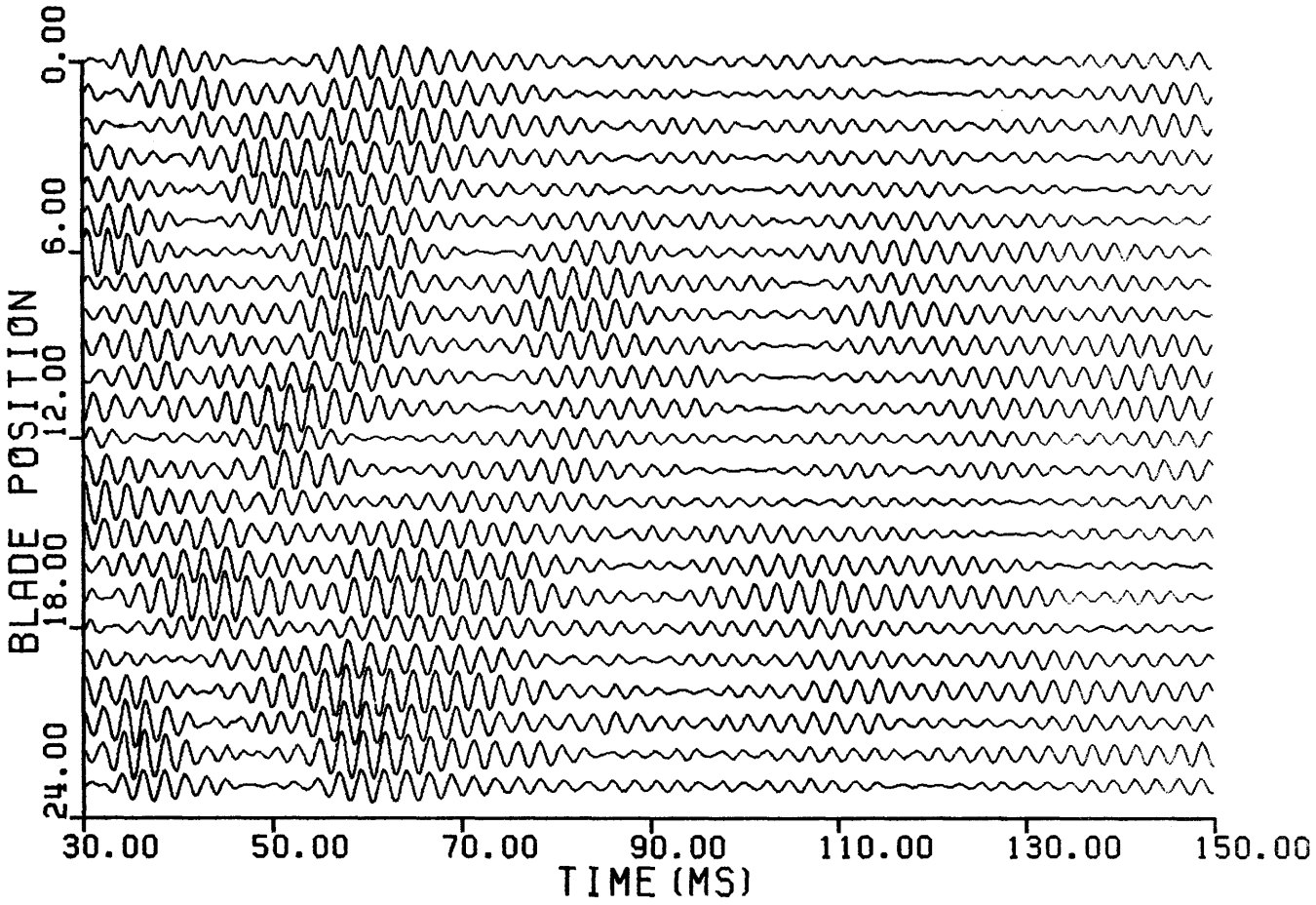

Figure 5-7 Blade response in the range 350-750 Hz.
(shown at the same scale as Figure 5-2)

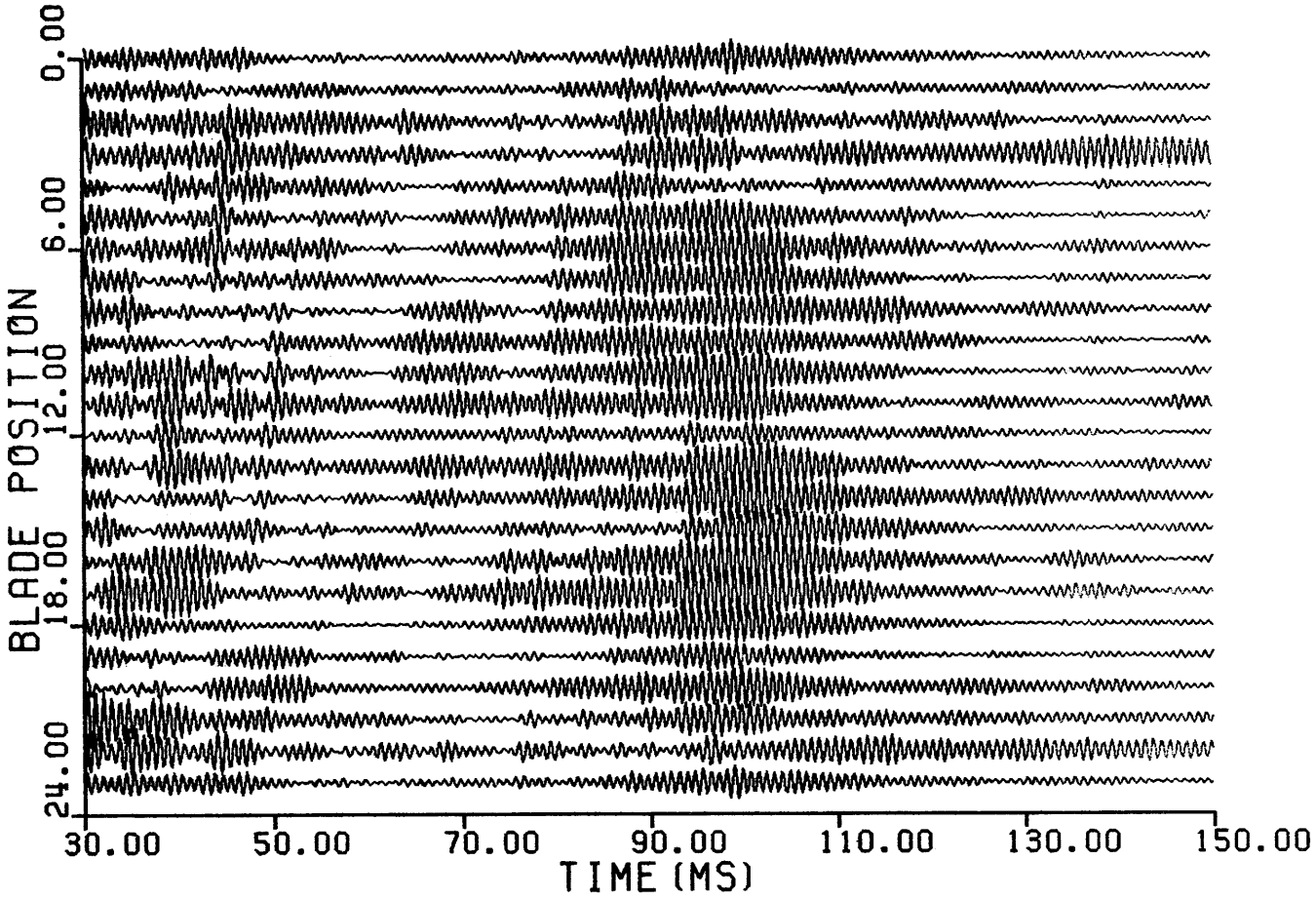

Figure 5-8 Blade response in the range 750-1500 Hz.
(shown at 3 times the scale of Figure 5-2)

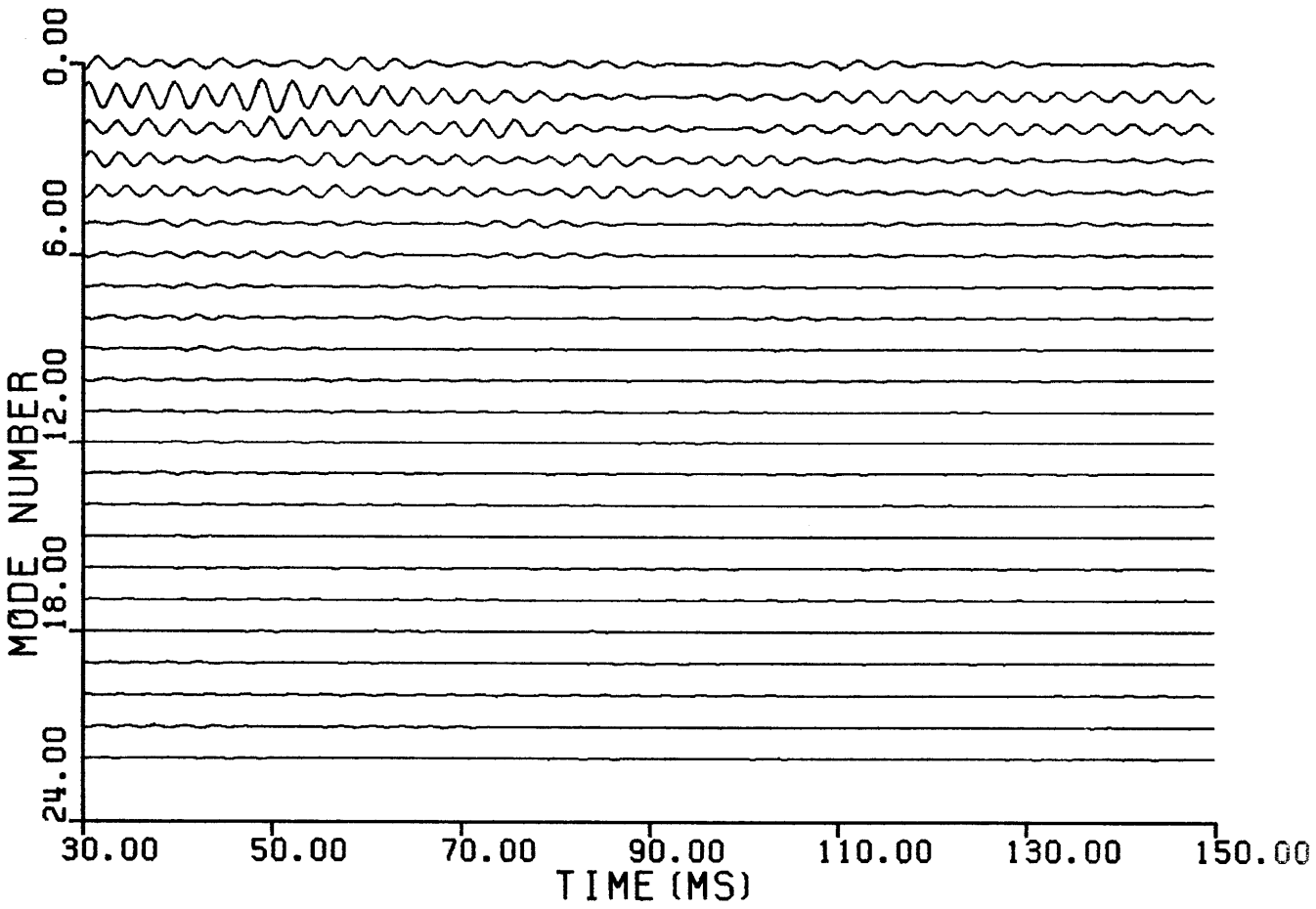

Figure 5-9a Amplitudes of the multiblade modes of the response in the range 220-350 Hz.

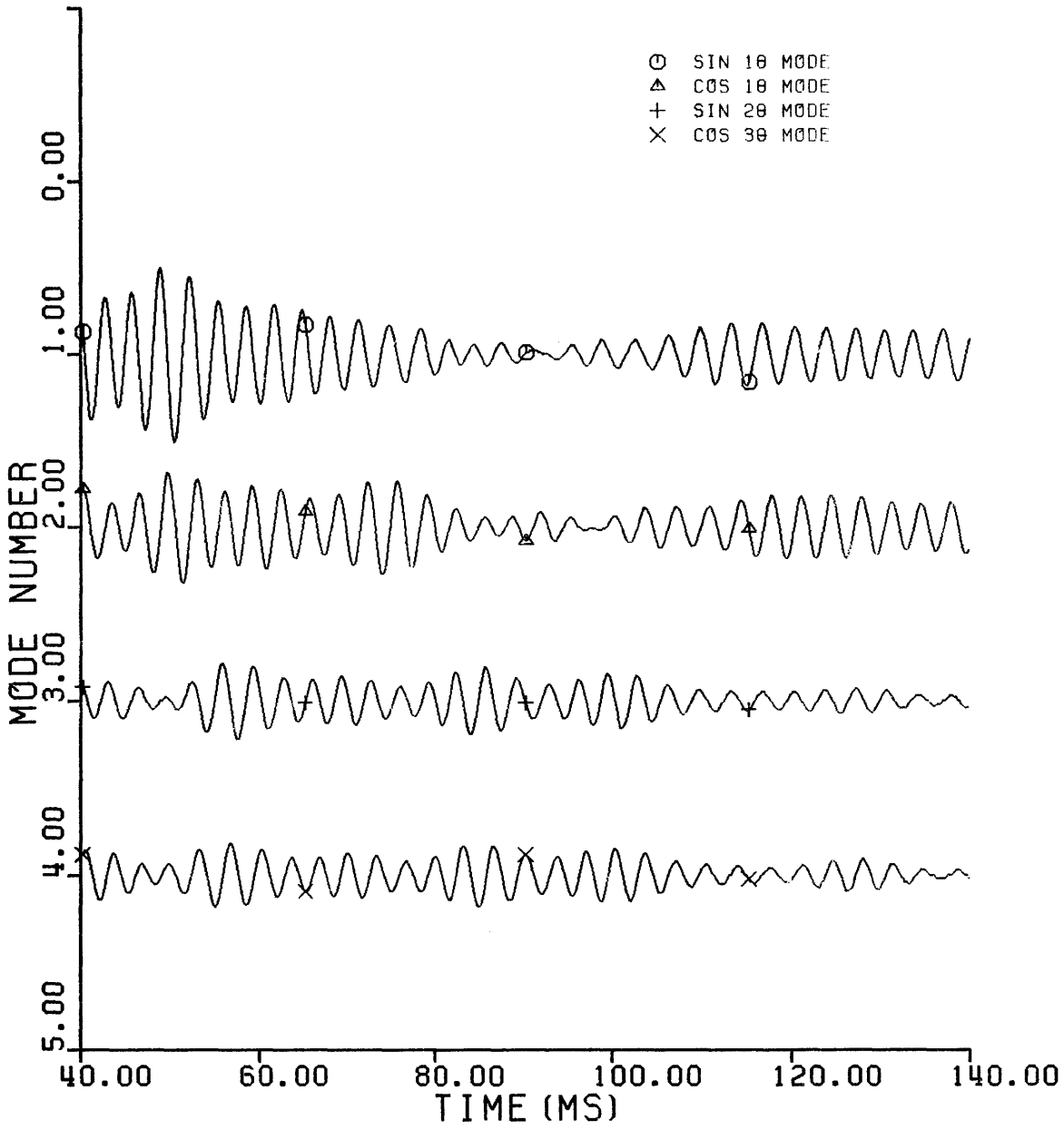

Figure 5-9b Amplitudes of several of the multiblade modes of the response in the range 220-350 Hz.

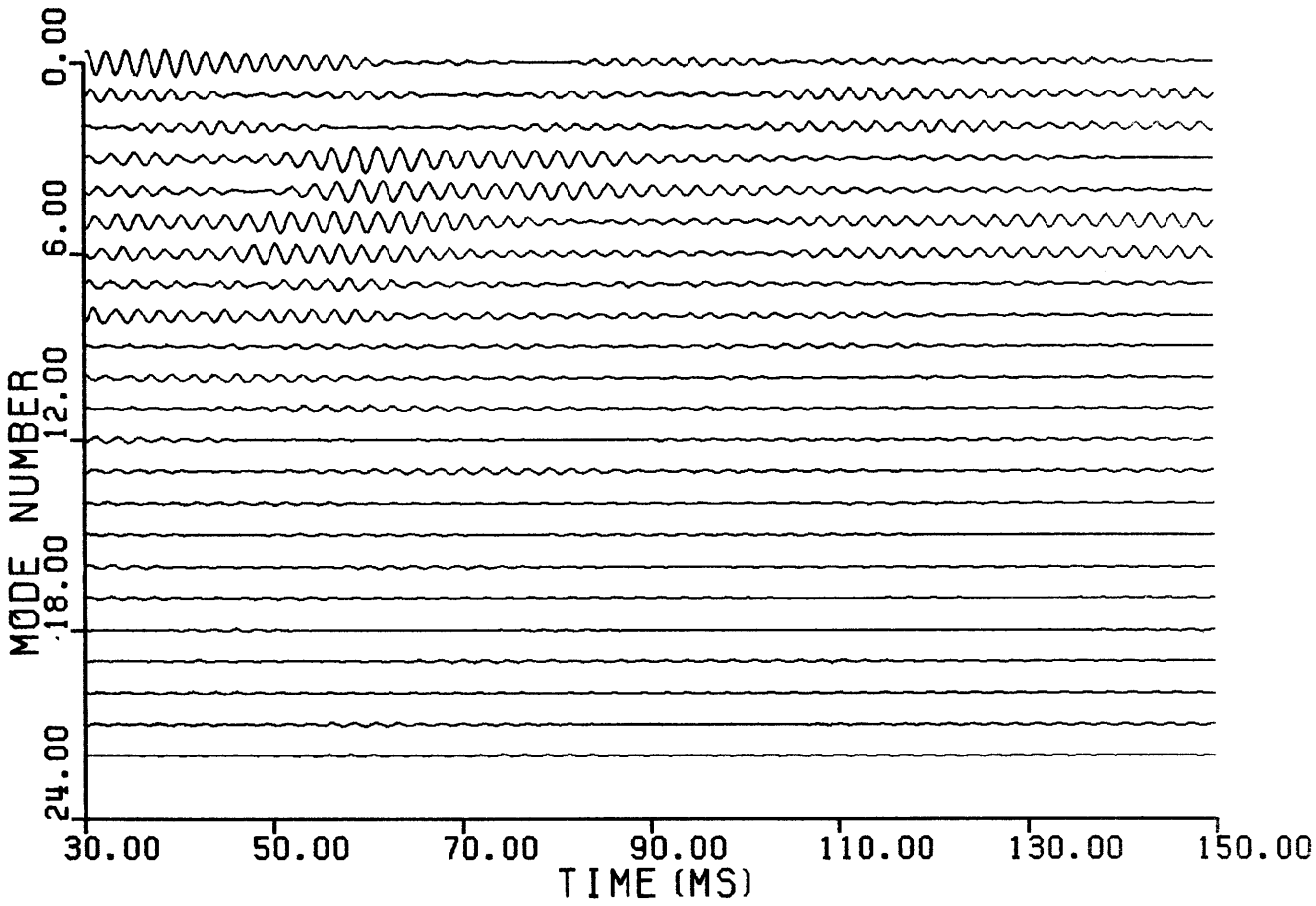

Figure 5-10a Amplitudes of the multiblade modes of the response in the range 350-750 Hz.

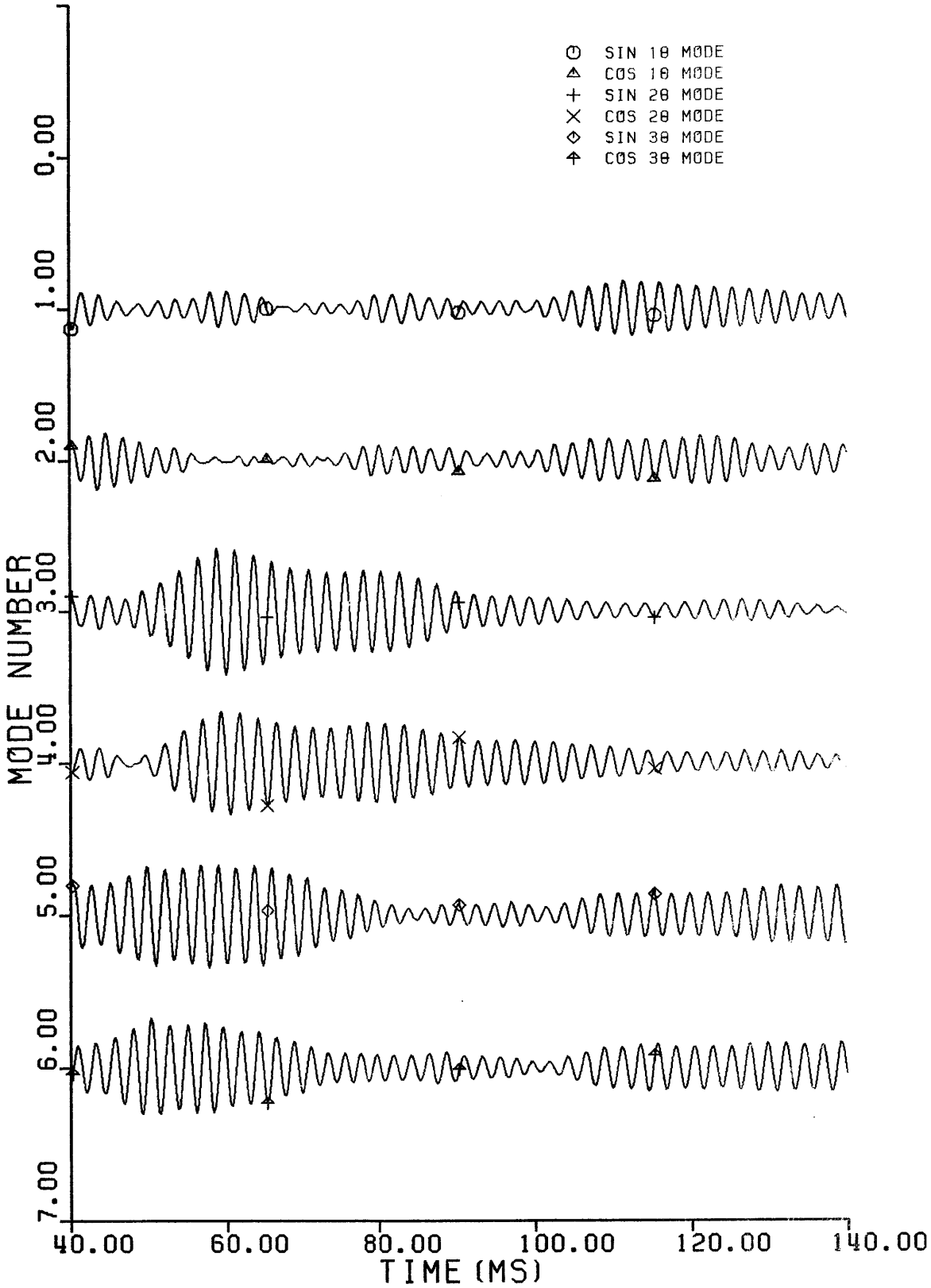

Figure 5-10b Amplitudes of several of the multiblade modes of the response in the range 350-750 Hz.

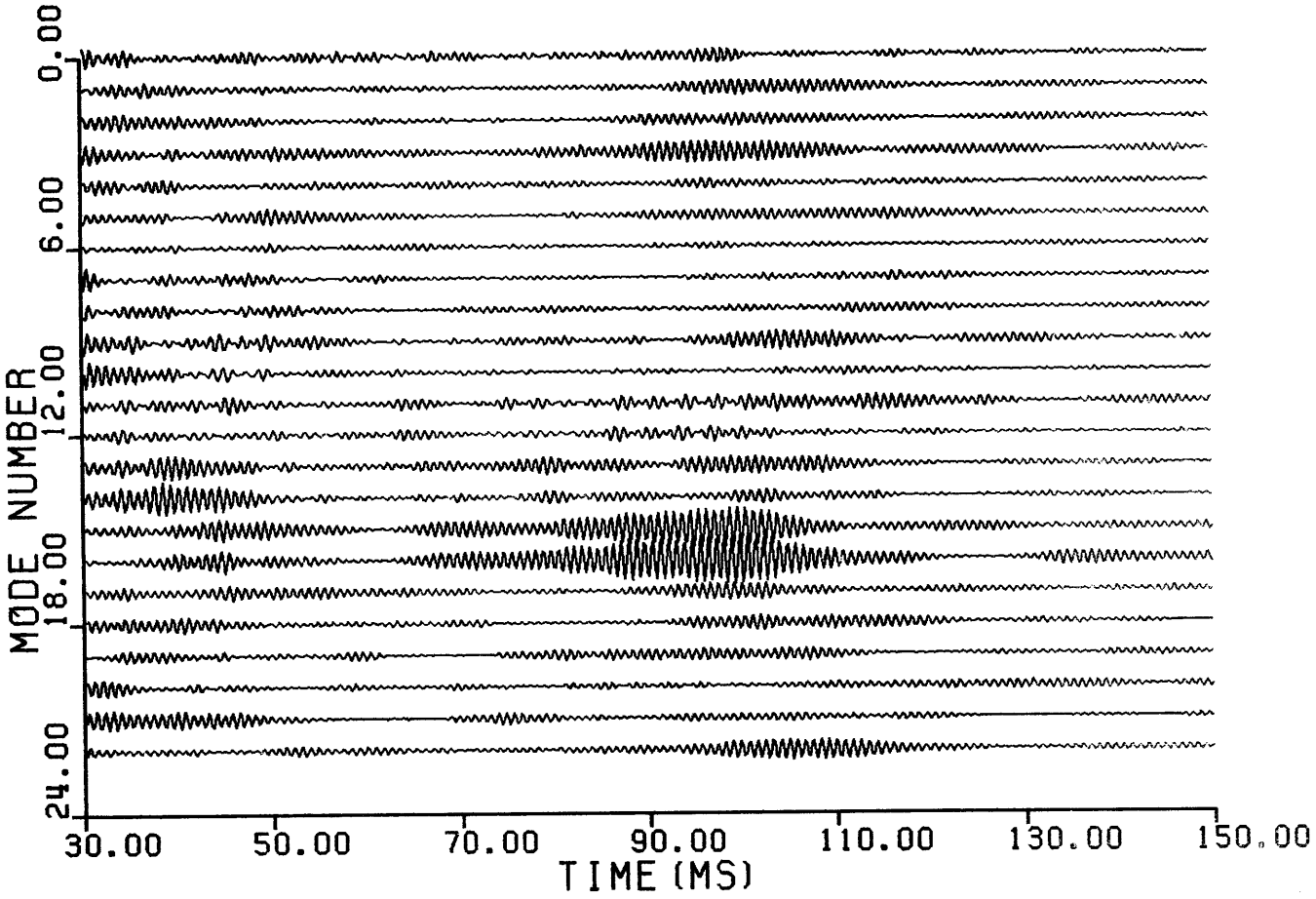

Figure 5-11a Amplitudes of the multiblade modes of the response in the range 750-1500 Hz.

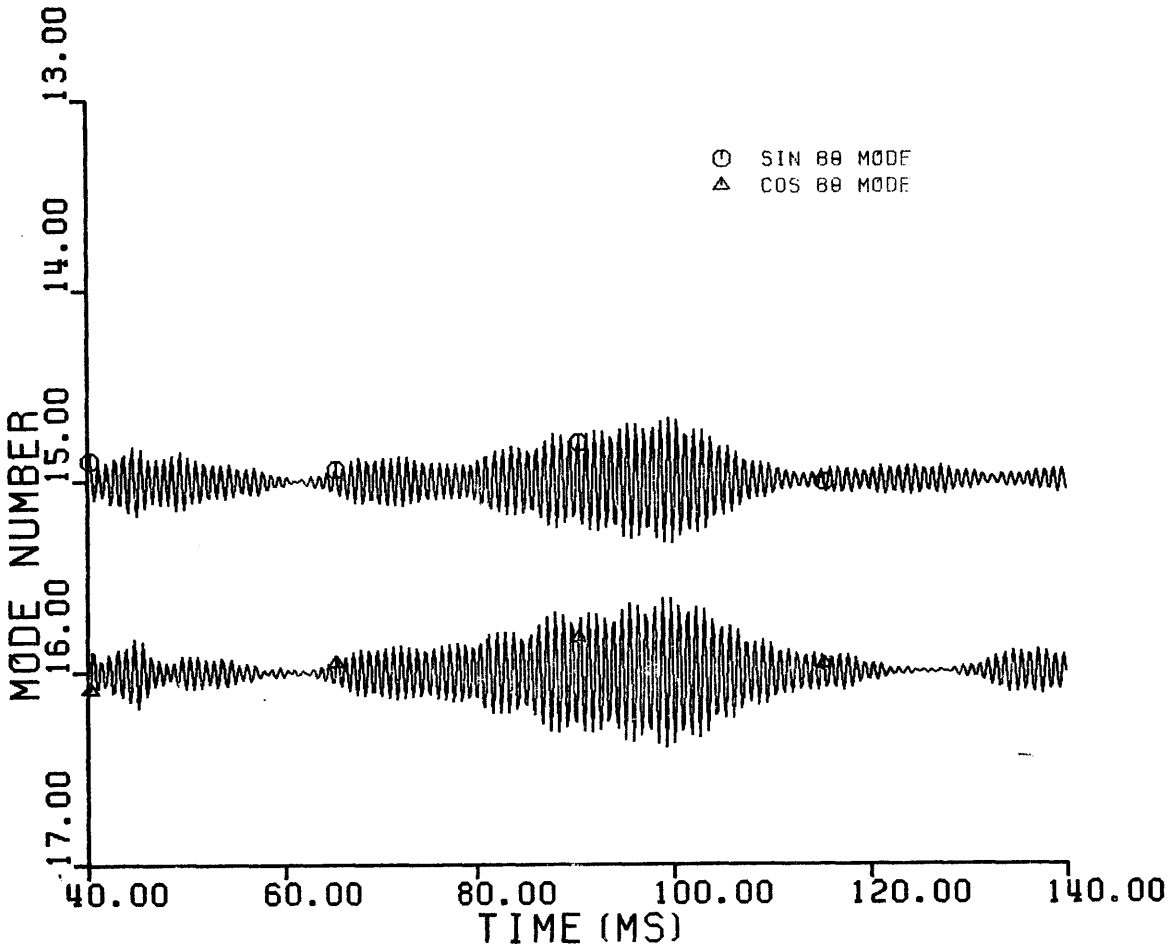

Figure 5-11b Amplitude of several of the multiblade modes of the response in the range 750-1500 Hz.

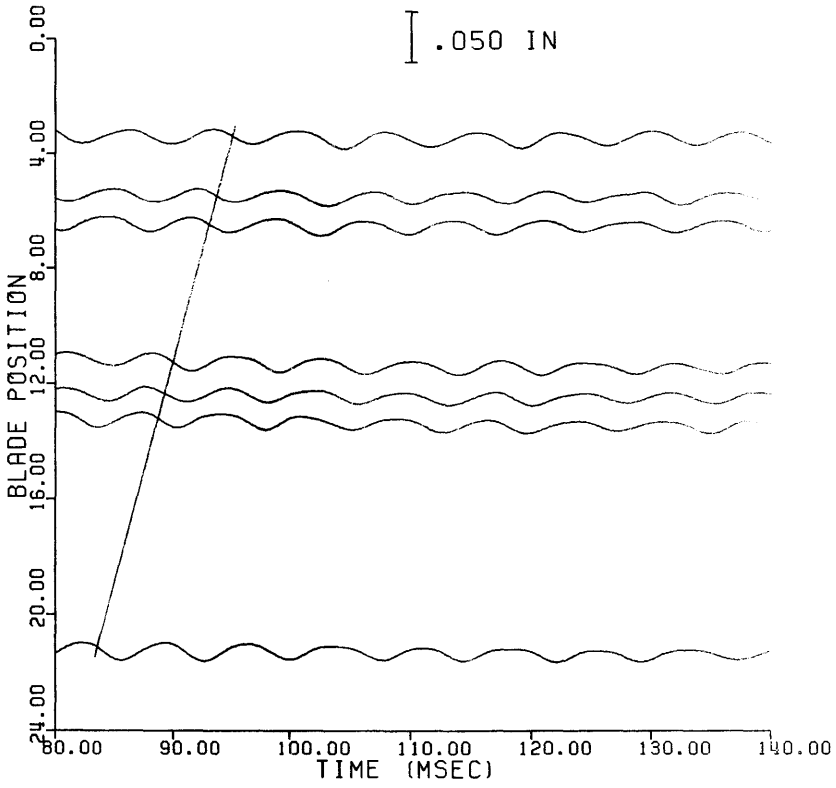

Figure 6-1 The blade response at the fundamental frequency of the 2-cell rotating stall.

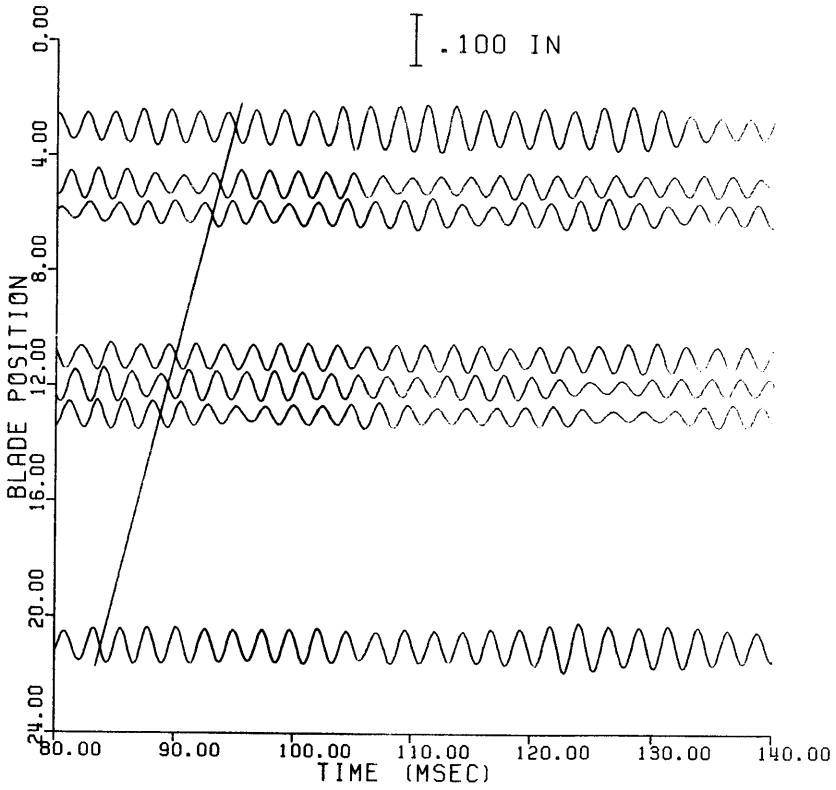

Figure 6-2 Blade response at the first bending frequency to a 2-cell rotating stall showing the strong phase lock of the blades.

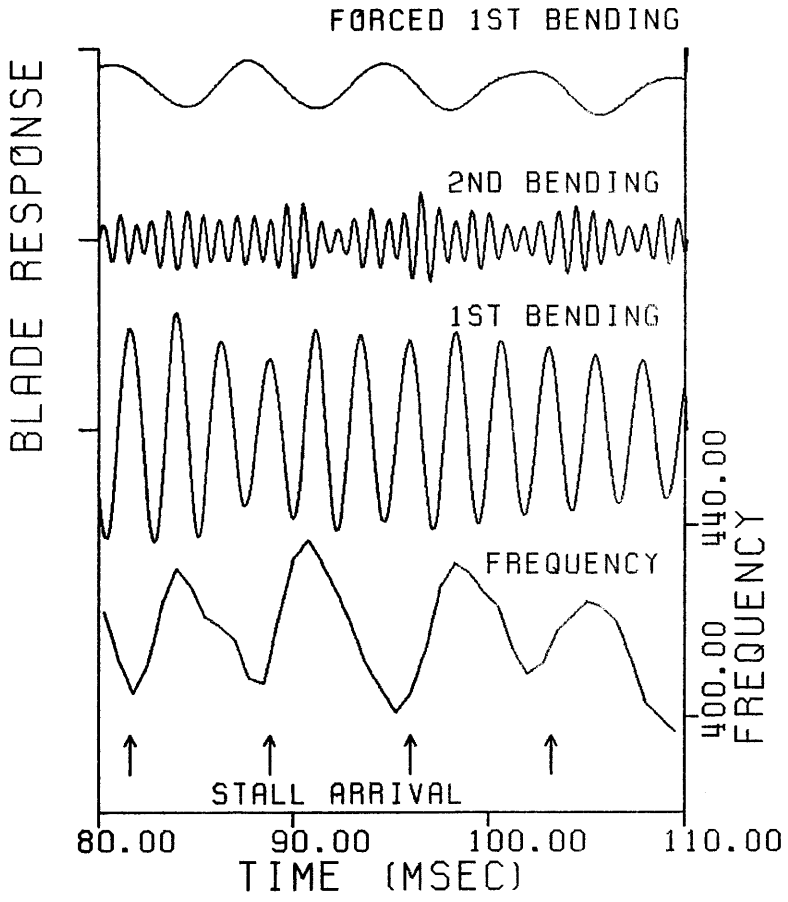

Figure 6-3 The passage of four individual stall cells is shown by the response at the forcing frequency of rotating stall, in the second bending mode (shown four times relative scale), and in the first bending mode. The frequency in Hertz of the first bending response is shown at the bottom. Arrows mark approximate time of arrival of the stall cell.

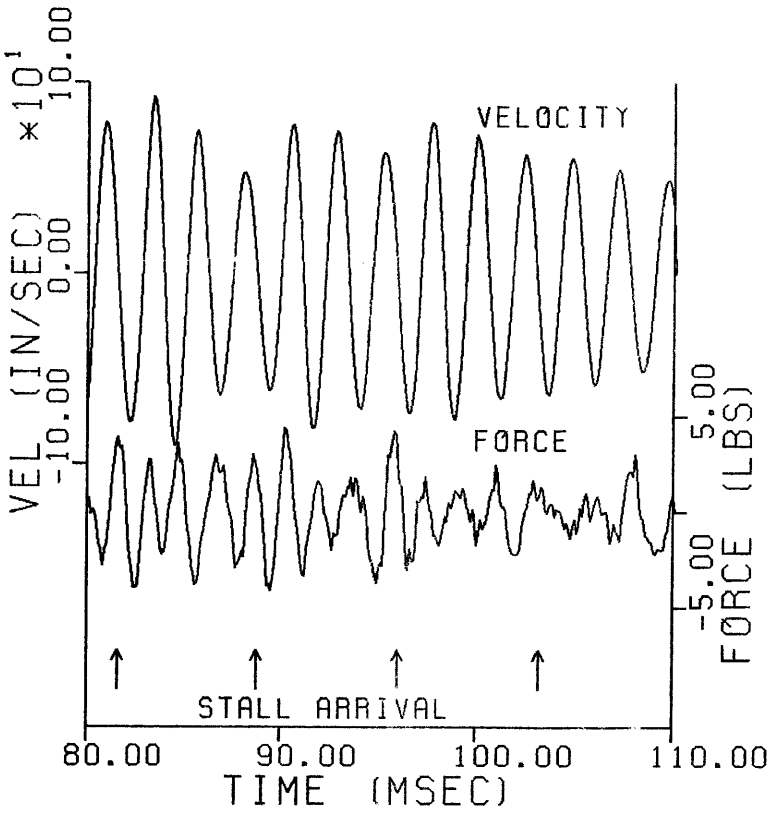

Figure 6-4 The modal (tip) velocity and force. Note that for about 24 msec after the arrival of the stall cell the force is in phase with the velocity. Outside that time they are 180° out of phase.

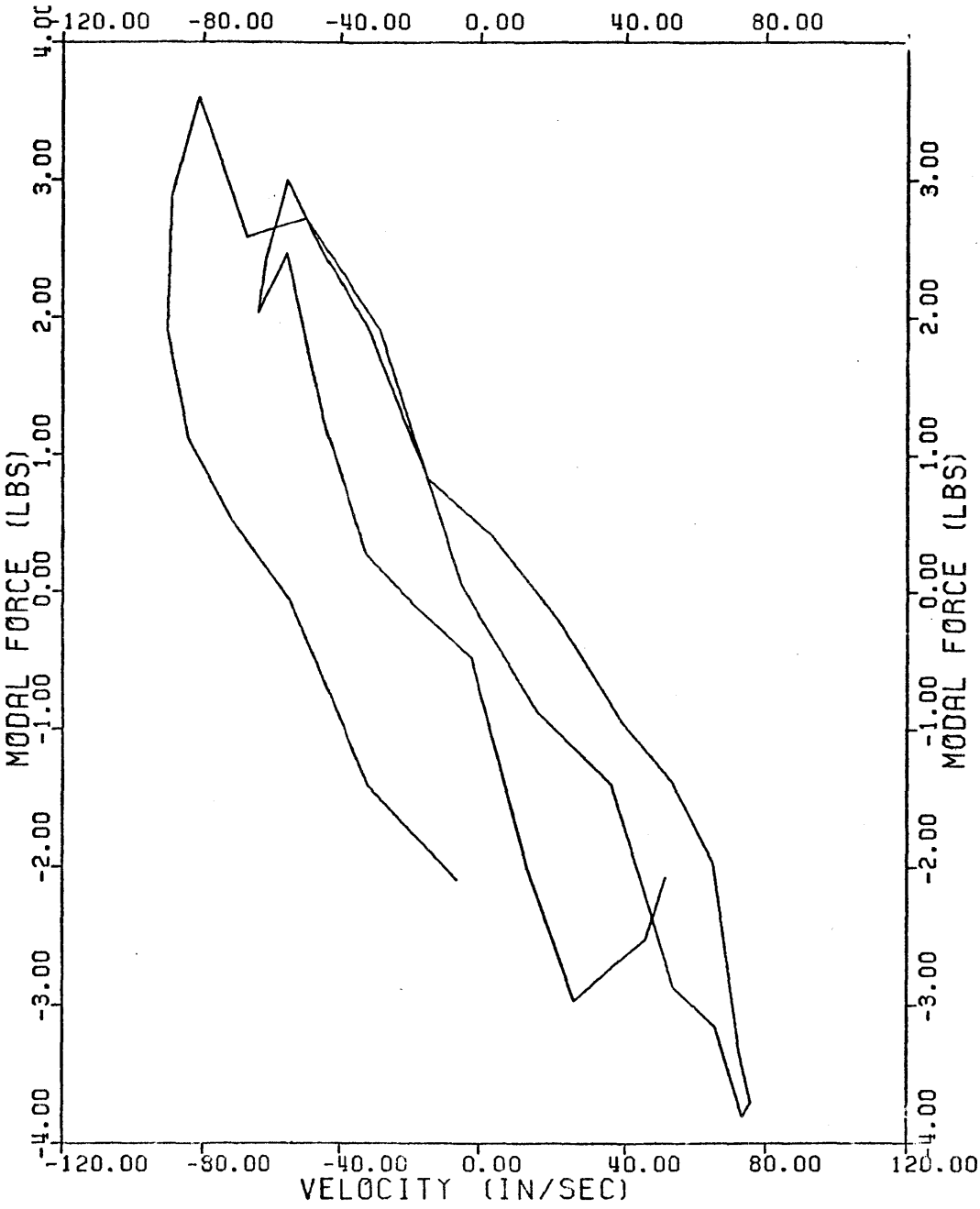

Figure 6-5 - A cross plot of the 1st bending modal force and velocity during the ring down from 84 to 88 msec. Note the very close phase relation of the two signals.